Linear, Parameter-Varying Control of Aeroservoelastic Systems

A DISSERTATION

SUBMITTED TO THE FACULTY OF THE GRADUATE SCHOOL

OF THE UNIVERSITY OF MINNESOTA

BY

Claudia Patricia Moreno Chicunque

IN PARTIAL FULFILLMENT OF THE REQUIREMENTS

FOR THE DEGREE OF

DOCTOR OF PHILOSOPHY

William Garrard

June 2015

Acknowledgements

I want to express my immense gratitude to my advisor Gary J. Balas. Prof. Balas' example of professionalism and positive attitude towards life made him the best mentor a student could want. He continually promoted and required excellence in all aspects of my career, including research, communication skills, and outreach. Prof. Balas was very approachable and made me feel welcome since day one as a graduate student. He raised my spirit in difficult times and turned feelings of frustration into confidence. It was truly and honor to work under Prof. Balas' direction and I will always feel proud to be called his student.

I would also like to thank Prof. William Garrard for all his help in this last stretch of my research. His support was key to culminate my studies and his valuable feedback helped me to improve my dissertation greatly. Thanks also to Prof. Peter Seiler, for his guidance through my whole graduate career. I will be forever in debt for all the support and countless robust control lessons he has provided to me. I want to thank the others in my committee, Prof. Demoz Gebre-Egziabher, Prof. Mihailo Jovanovic, and Prof. Tryphon Georgiou. Their excellent classes provided me with great knowledge and helped to advance in my research significantly.

Thanks to all my coworkers in the Aeroservoelastic group: Harald, Bela, Aditya and Abhineet. The great support I received from all of them in these years helped to achieve this goal. Special thanks to Harald for the immense contributions to my research and great friendship that kept me headed in the right direction. I also want to acknowledge the former Lab 15 members: Abhijit, Andrei, Arnar, Arda, Paul, David, Shu and Bin. Our fun conversations made of grad school a better place when frustration seemed to win. No less important are my Colombian friends David, Juanjo and Carlos. They really made grad school fun. I enjoyed every break and late night dinners we had these 5 years. I am also very grateful that grad school brought my future husband to my life. Paul, your incredible love, great patience and sweet support kept me motivated through the end of this journey. I am sure many more adventures are waiting for us in this new chapter.

To my mother: Raquel Chicunque

&

The memory of my father: Orlando Moreno

Abstract

Modern aircraft designers are adopting light-weight, high-aspect ratio flexible wings to improve performance and reduce operation costs. A technical challenge associated with these designs is that the large deformations in flight of the wings lead to adverse interactions between the aircraft aerodynamic forces and structural forces. These adverse interactions produce excessive vibrations that can degrade flying qualities and may result in severe structural damages or catastrophic failure. This dissertation is focused on the application of multivariable robust control techniques for suppression of these adverse interactions in flexible aircraft. Here, the aircraft coupled nonlinear equations of motion are represented in the linear, parameter-varying framework. These equations account for the coupled aerodynamics, rigid body dynamics, and deformable body dynamics of the aircraft. Unfortunately, the inclusion of this coupled dynamics results in high-order models that increase the computational complexity of linear, parameter-varying control techniques. This dissertation addresses three key technologies for linear, parameter-varying control of flexible aircraft: (i) linear, parameter-varying model reduction; (ii) selection of actuators and sensors for vibration suppression; and (iii) design of linear, parameter-varying controllers for vibration suppression. All of these three technologies are applied to an experimental research platform located at the University of Minnesota. The objective of this dissertation is to provide to the flight control community with a set of design methodologies to safely exploit the benefits of light-weight flexible aircraft.

Contents

List of Tables

List of Figures

ix

xiii

Chapter 1

Introduction

The need for improved performance and reduced operating costs has led modern aircraft designers to adopt light-weight, high aspect ratio flexible wings. Reducing weight decreases aerodynamic drag, leading to less fuel consumption. High aspect ratio wings minimize drag over lift, improving the aircraft performance on aspects such as long range and endurance. These modifications are being applied to modern commercial airplanes, mainly by using composite materials for both fuselage and wings. As result, the new generation of long range airliners developed by Boeing (787) and Airbus (A350) show higher fuel efficiency and lower costs than previous similar sized aircraft.

The aerodynamic advantages of high aspect ratio flexible wings are also being exploited to develop autonomous aircraft for intelligence, surveillance and reconnaissance missions. These light-weight, high-altitude, long-endurance vehicles with large wing span exhibit high flexibility and significant deformation in flight leading to increased interaction between the rigid body and structural dynamics modes. This phenomenon, called *Body Freedom Flutter*, occurs as the aircraft rigid body frequency response increases with airspeed and interacts with a wing vibration mode, typically the wing bending mode. The interaction can lead to poor handling qualities and may result in dynamic instability. Hence, an integrated active approach to flight control, flutter suppression and structural mode attenuation is required to meet the desired handling quality performance and gust load alleviation for modern flexible aircraft.

Numerous flutter suppression control strategies have been proposed to address the coupled rigid body and aeroelastic dynamics. These include optimal control [6, 7], dynamic inversion control [8], robust multivariable control [9], model predictive control [10] and gain scheduled control [11–14]. A majority of these strategies are model based, hence require an

accurate description of the aeroelastic behavior of the aircraft. Flutter analysis of aircraft has been widely studied [15–18] and numerous researchers have addressed aeroelastic modeling for highly flexible aircraft [6,8,14,19]. Currently, modeling of a flexible aircraft requires a geometric structural model coupled with a consistent aerodynamic model. The nonlinear aeroelastic models are derived based on structural finite elements and lifting-surface theory, both of which are available in general purpose commercial codes [20–22]. It is standard practice to represent the fully coupled nonlinear aircraft model as a linear model which varies as a function of parameters across the flight envelope, i.e. linear parameter varying (LPV) systems, hence the traditional description of aeroservoelastic models for control fits naturally in the LPV framework.

The LPV system framework provides a rich, theoretical control analysis and design framework for nonlinear systems [11,23–30]. This framework allows gain-scheduled, multivariable controllers to be treated as a single entity, with the gain-scheduling achieved via the parameter-dependent controller. The main advantages of these controllers are the guarantees in adaptability, global stability, robust performance, and real-time implementation while using linear system theory for their design. Unfortunately, LPV control synthesis techniques scale badly with the number of scheduling variables and dynamic order of the system. This rapid increase in the synthesis problem size has limited the applications of LPV controllers in industry. Hence, complementary research is required to make the LPV framework suitable for aeroservoelastic systems.

The main contribution of this dissertation is to expand the applications of the LPV framework to aeroservoelastic systems. It is largely based on the application of LPV techniques to an aeroservoelastic research platform at the University of Minnesota. This experimental vehicle is described by a set of linear, continuous-time, state-space models that includes rigid-body dynamics and aeroelastic effects. However, the inclusion of such effects increases the order of the models significantly. Hence, a LPV model reduction procedure is proposed in this dissertation to make the aeroservoelastic model of the aircraft suitable for control. Once the vehicle is described with an appropriate number of states, the following task is to design controllers to suppress the unstable aeroelastic interactions and provide additional damping to flexible modes. A previous step for control design is the selection of actuators and sensors that will achieve the desired performance. This dissertation also proposes an actuator and sensor selection method for control design. Finally, the reduced order aeroservoelastic model together with the the subset of actuators and sensors selected are used to design robust multivariable controllers that effectively suppress aeroservoelastic interactions and provides additional damping to structural modes.

This dissertation is organized as follows. Chapter 2 presents a brief overview of aeroservoelastic modeling approaches available in the literature. Details about the modeling approach that describes the aeroservoelastic experimental research vehicle are presented. Here, the parameter-varying nature of the system is exploited to represent the models in the LPV framework. The chapter concludes with an introduction to LPV systems and an overview of the relevant theoretical background for this dissertation. Chapter 3 introduces the University of Minnesota aeroservoelastic research platform used to develop active flutter suppression technologies. A thorough description of the vehicle is presented with a characterization of its structural and aeroelastic properties. Chapter 4 presents a model order reduction approach for aeroservoelastic systems and its application to the experimental vehicle. This reduced order model is then used in the following chapters for control purposes. Chapter 5 describes the actuator and sensor selection method for aeroservoelastic systems previous to the control design task. The results of applying this method to the experimental vehicle available are also presented in this chapter. Chapter 6 presents the multivariable robust controller designs and results for the experimental flexible aircraft. Finally, concluding remarks are provided in Chapter 7.

Chapter 2

Aeroservoelastic Modeling

Aeroservoelastic modeling includes the interaction of the aircraft flexible structure, steady and unsteady aerodynamic forces resulting from the aircraft motion, and the flight control system. The integration of these three disciplines has been approached by the literature in several manners [31–35]. This chapter describes the modeling approach based on the rigid-body dynamics augmented with linear structural modeling. Here, the coupled nonlinear equations are simplified by the mean axes assumptions, resulting in independent equations for the rigid body dynamics and elastic deformations [31]. These decoupled equations can be then linearized to obtain a linear, parameter-varying (LPV) system where the scheduling parameters are typically airspeed and altitude. The following sections present the mean axes modeling approach and introduce the fundamentals of LPV systems.

2.1 Aeroservoelastic Model (Mean Axes Assumptions)

The equations governing the aeroservoelastic dynamics of an unrestrained aircraft are [36]:

$$\begin{bmatrix} m_b(\dot{V}_b + \Omega_b \times V_b - T_{bE}g_E) \\ I_b\dot{\Omega}_b + \Omega_b \times (I_b\Omega_b) \end{bmatrix} = \Phi_b^T P^c$$

$$\hat{M}_f\ddot{\eta}_f + \hat{\Xi}_f\dot{\eta}_f + \hat{K}_f\eta_f = \Phi_f^T P^c \qquad (2.1)$$

where m_b is the total body mass, I_b is the mass inertia, g_E is the gravitational vector, and Φ_b is the rigid body modal matrix about the center of gravity with directions customary in flight mechanics. V_b and Ω_b are the velocity and angular velocity in the mean axis body frame of reference, T_{bE} transforms the gravitational vector from an earth fixed coordinate frame E to the body fixed coordinate frame b. Here, η_f is the vector of elastic modal displacements,

$\hat{M}_f$ is the generalized modal mass matrix, $\hat{K}_f$ is the generalized modal stiffness matrix, $\hat{\Xi}_f$ is the generalized damping matrix, Φ_f is the flexible modal matrix, and P^c is the vector of aerodynamic forces and moments applied to the airframe.

Currently, the available commercial software (e.g. NASTRAN and ZAERO) creates ASE models using the mean axes formulation in (2.1) [20, 22]. Here, the generalized mass and stiffness matrices are usually obtained from structural finite element methods. This structural modeling is detailed in Chapter 3. In addition, the aerodynamic forces and moments in the airframe are derived from unsteady aerodynamic panel methods. These methods are often formulated in the frequency domain by assuming simple harmonic motion. The objective is to compute a frequency domain aerodynamic influence coefficient (AIC) matrix that relates the resultant aerodynamic forces to the panels deformations such that

$$P_a = q_\infty \left[AIC(jk)\right] a \tag{2.2}$$

where P_a is the vector of resultant aerodynamic forces, a is the vector of aerodynamic deformations, q_∞ is the dynamic pressure, and k is the reduced frequency parameter defined as

$$k = \frac{\omega_a c}{2V} \tag{2.3}$$

with ω_a representing the assumed harmonic oscillatory frequency, c representing the reference chord, and V representing the velocity of undisturbed flow. Details about the generation of this AIC matrix can be found in [5].

A common problem encountered in this software is that displacements in the structural finite element model do not match with the aerodynamic panel displacements. Hence, the standard practice is to transfer the data from the aerodynamic panel model to the structural finite element model using an interpolation method called splining [20]. This splining method relates the aerodynamic panel forces to the structural forces such that

$$P_a = T_{as} P^c \tag{2.4}$$

where T_{as} is the interpolation matrix converting structural deflections to aerodynamic panel deflections. Similarly, the aerodynamic panel deflections can be related to the modal deflections η as

$$a = T_{as} \Phi \eta \tag{2.5}$$

where $\Phi = [\Phi_b,\ \Phi_f]$ and $\eta^T = \left[\eta_b^T,\ \eta_f^T\right]$. Here, η_b represents the rigid modal displacements.

Combining (2.2), (2.4), and (2.5) results in the vector of aerodynamic forces and moments P^c described as

$$P^c = q_\infty T_{as}^T \left[AIC(jk)\right] T_{as} \Phi \eta \tag{2.6}$$

Here, the vector $\Phi^T P^c$ is called the generalized aerodynamic forces and moments where

$$F(jk) = \Phi^T T_{as}^T \left[AIC(jk)\right] T_{as} \Phi \tag{2.7}$$

represents the generalized aerodynamic matrices in the frequency domain. Now, in order to make the frequency domain unsteady aerodynamics usable for time domain calculations, the generalized matrix $F(jk)$ needs to be approximated as a rational function. Typically, this approximation is in the form [37, 38]

$$F(jk) = F_0 + F_1 jk + F_2 j^2 k^2 + \sum_{l=1}^{n_L} F_{l+2} \frac{jk}{jk + b_l} \tag{2.8}$$

where $jk = \frac{c}{2V} s$ and s is the Laplace variable. Here, b_l represents the aerodynamic lags necessary to obtain a linear fit.

The approximation in (2.8) can be re-written in terms of s as

$$F(s) = F_0 + \frac{c}{2V} F_1 s + \left(\frac{c}{2V}\right)^2 F_2 s^2 + \sum_{l=1}^{n_L} F_{l+2} \frac{s}{s + \bar{b}_l} \tag{2.9}$$

with $\bar{b}_l = \frac{2V}{c} b_l$. Then, the vector of generalized forces and moments expressed in the time domain is

$$\Phi^T P^c = q_\infty \left[F_0 \eta + \frac{c}{2V} F_1 \dot{\eta} + \left(\frac{c}{2V}\right)^2 F_2 \ddot{\eta} + x_a\right] \tag{2.10}$$

where x_a represents the aerodynamic lag states defined by

$$\dot{x}_a = -\bar{b}_l x_a + F_{l+2} \dot{\eta} \tag{2.11}$$

Notice that (2.10) is a function of dynamic pressure and airspeed. Hence, the ASE equations of motion in (2.1) can be represented as a linear, parameter-varying (LPV) system where altitude and airspeed are the scheduling parameters. Next, the fundamental theory of LPV system is presented.

2.2 Linear, Parameter-Varying Systems [1]

Consider the following nonlinear system:

$$\dot{x}(t) = f(x(t), d(t), \rho(t))$$
$$e(t) = h(x(t), d(t), \rho(t)) \tag{2.12}$$

where f and h are differentiable, input $d(t) \in \mathbb{R}^m$, output $e(t) \in \mathbb{R}^p$, state variable $x(t) \in \mathbb{R}^n$ and $\rho(t) \in \mathbb{R}^{n_\rho}$ is a measurable exogenous parameter vector, called the scheduling

parameter. The parameter vector ρ is assumed to be a continuously differentiable function of time and the admissible trajectories are restricted based on physical considerations to a known compact subset $\mathcal{P} \subset \mathbb{R}^{n_\rho}$. The rates of the parameter variation $\dot{\rho}$ are assumed to be bounded in some applications, i.e. $\dot{\rho} \in \dot{\mathcal{P}}$, where $\dot{\mathcal{P}} \subset \mathbb{R}^{n_\rho}$ is a compact subset. In addition, the set of admissible trajectories is defined as

$$\mathcal{A} := \left\{ \rho : \mathbb{R}^+ \to \mathbb{R}^{n_\rho} : \rho(t) \in \mathcal{P}, \dot{\rho}(t) \in \dot{\mathcal{P}} \ \forall t \geq 0 \right\} \tag{2.13}$$

where $\dot{\mathcal{P}}$ is defined by

$$\dot{\mathcal{P}} := \{\dot{\rho} \in \mathbb{R}^{n_\rho} \,|\, |\dot{\rho}_i| \leq \nu_i, \ i = 1, \ldots, n_\rho\} \tag{2.14}$$

From now on, the explicit dependence on time t is suppressed throughout the remainder of this dissertation to shorten the notation.

Assumption 2.2.1 *There is a family of equilibrium points $(\bar{x}(\rho), \bar{d}(\rho))$ such that*

$$\begin{aligned} f(\bar{x}(\rho), \bar{d}(\rho), \rho) &= 0 \\ \bar{e}(\rho) &= h(\bar{x}(\rho), \bar{d}(\rho), \rho) \end{aligned} \qquad \forall \rho \in \mathcal{A} \tag{2.15}$$

Then, the nonlinear system given by (2.12) can be linearized about the equilibrium points via Jacobian linearization based on Taylor series expansion. Define the deviation variables as

$$\delta_x := x - \bar{x}(\rho), \quad \delta_d := d - \bar{d}(\rho), \quad \delta_e := e - \bar{e}(\rho) \tag{2.16}$$

Differentiating the δ_x term of (2.16) results in

$$\dot{\delta}_x = \dot{x} - \dot{\bar{x}}(\rho) = f(x, d, \rho) - \dot{\bar{x}}(\rho) \tag{2.17}$$

The Taylor series expansion of f and h about the equilibrium point yields

$$\begin{aligned} \dot{\delta}_x &= \nabla_x f|_o \, \delta_x + \nabla_v f|_o \, \delta_d + \epsilon_f(\delta_x, \delta_d, \rho) - \dot{\bar{x}}(\rho) \\ \delta_e &= \nabla_x h|_o \, \delta_x + \nabla_d h|_o \, \delta_d + \epsilon_h(\delta_x, \delta_d, \rho) \end{aligned} \tag{2.18}$$

where the $|_o$ denotes the evaluation at the equilibrium point $(\bar{x}(\rho), \bar{d}(\rho), \rho)$, and ϵ_f, ϵ_h represent the higher order terms of the Taylor series expansion. The term $\dot{\bar{x}}(\rho)$ arises due to the time variation in ρ. The linearization is performed with respect to (x, d) but the nonlinear dependence on ρ is retained. Define $L(\rho) := -\nabla \bar{x}(\rho)$. Then the linearization about the family of trim points (2.15) takes the form

$$\begin{aligned} \dot{\delta}_x &= A(\rho)\delta_x + B(\rho)\delta_d + L(\rho)\dot{\rho} + \epsilon_f(\delta_x, \delta_d, \rho) \\ \delta_e &= C(\rho)\delta_x + D(\rho)\delta_d + \epsilon_h(\delta_x, \delta_d, \rho) \end{aligned} \tag{2.19}$$

7

The LPV system is commonly obtained by assuming that the higher order terms of the Taylor series are negligible, i.e. $\epsilon_f, \epsilon_h \approx 0$. In addition, it is typically assumed that the parameter variation is sufficiently slow so that $L(\rho)\dot{\rho} \approx 0$. Under these assumptions, an LPV system G_ρ is defined using x, d, e instead of the deviation variables as

$$
\begin{aligned}
\dot{x} &= A(\rho)x + B(\rho)d \\
e &= C(\rho)x + D(\rho)d
\end{aligned}
\tag{2.20}
$$

Note that other approaches exist in literature to obtain LPV models from a nonlinear system, e.g., function substitution [39]. However, the most prevalent approach is based on the Jacobian linearization presented in this section. The LPV models of ASE systems in this dissertation were obtained by this approach. Following, the experimental research platform at the University of Minnesota and its LPV ASE model is introduced in the next chapter.

Chapter 3

Body Freedom Flutter Test Vehicle

The Air Force Research Laboratory (AFRL) contracted with Lockheed Martin Aeronautics Company to develop a flight test vehicle for demonstration of active aeroservoelastic (ASE) control technologies [4, 6]. This research program successfully predicted the rigid/flexible coupling of the aircraft with refined models validated through flight tests. Five BFF aircraft were built during the execution of the program. After the conclusion of the program, the University of Minnesota received one of the BFF vehicles in order to demonstrate ASE stability and performance with robust control design techniques. Fig. 3.1 shows a picture of the test vehicle at its time of arrival to the University of Minnesota. Much of the research presented in this dissertation is based on this experimental vehicle. The first sections of this chapter present a general description of the BFF aircraft. Here, the particular geometry and structural design are key to understand the ASE phenomena in the aircraft. Finally, the chapter concludes with a discussion of these ASE characteristics for the BFF aircraft.

3.1   Body Freedom Flutter Aircraft

The BFF aircraft is a light-weight, high-aspect ratio flying wing with an anti-symmetric airfoil section. Fig. 3.2 shows the detailed drawings of the vehicle's important components and sections with corresponding dimensions in the international system of units. These drawings show that the aircraft has a 22° swept-back wing planform, spanning 3.05 m, and chord length of 29.7 cm. In addition, winglet panels of 27.9 cm height, are located at the tip of each wing to provide directional stability.
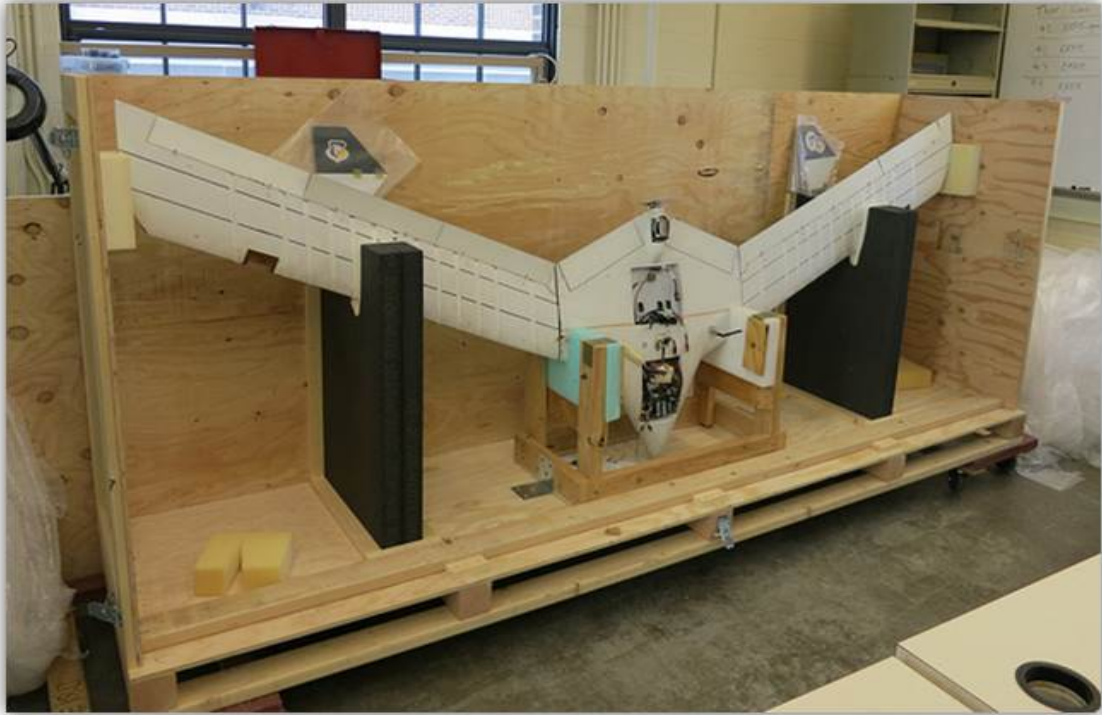
Figure 3.1: Body freedom flutter (BFF) aircraft at uninhabited aerial vehicle research laboratory in the University of Minnesota

The structure of the aircraft consists of two flexible wings fixed to a rigid center body. These flexible wings are built with light-weight foam and covered with a fiberglass skin. Each wing is supported by a single layer carbon fiber over foam core spar with rectangular cross-section of 7.7 cm width and 6 mm height. Notice that Fig. 3.2 shows cross-sectional cuts in the the wings. These cuts are made in order to guarantee that the spars are the only structural elements contributing to the strength of the wings. On the other hand, the center section is fabricated of carbon fiber and contains the majority of the vehicle's flight systems. These include the flight controls, air data, propulsion and batteries. The center body is a rugged construction that protects the most expensive components of the aircraft in case of flutter [40]. Some of these details can be observed in the transparent view showed in Fig. 3.3. In addition, the details about the dynamic behavior of the vehicle's structure are presented in the following section.

Furthermore, the flight control instrumentation of the BFF aircraft is depicted in Fig. 3.4. Here, it is observed that the entire trailing edge of the flying wing consists of eight control surfaces. The sensor suite of the aircraft consist of gyros to measure the vehicle's rates,
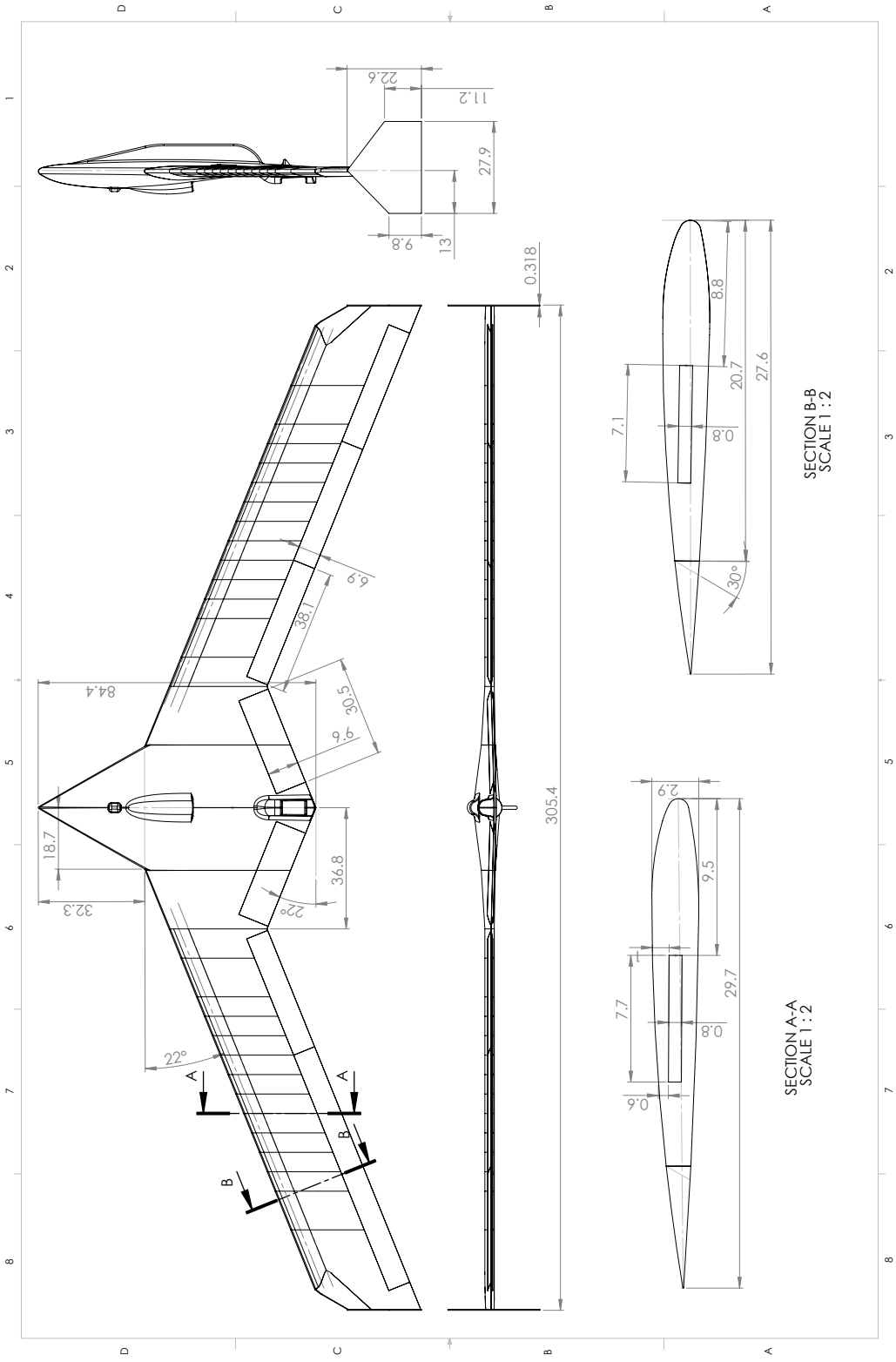
Figure 3.2: Body freedom flutter (BFF) aircraft drawing: planform view, airfoil and winglet sections. Measures are in cm. Source: Uninhabited aerial vehicle research laboratory at the University of Minnesota
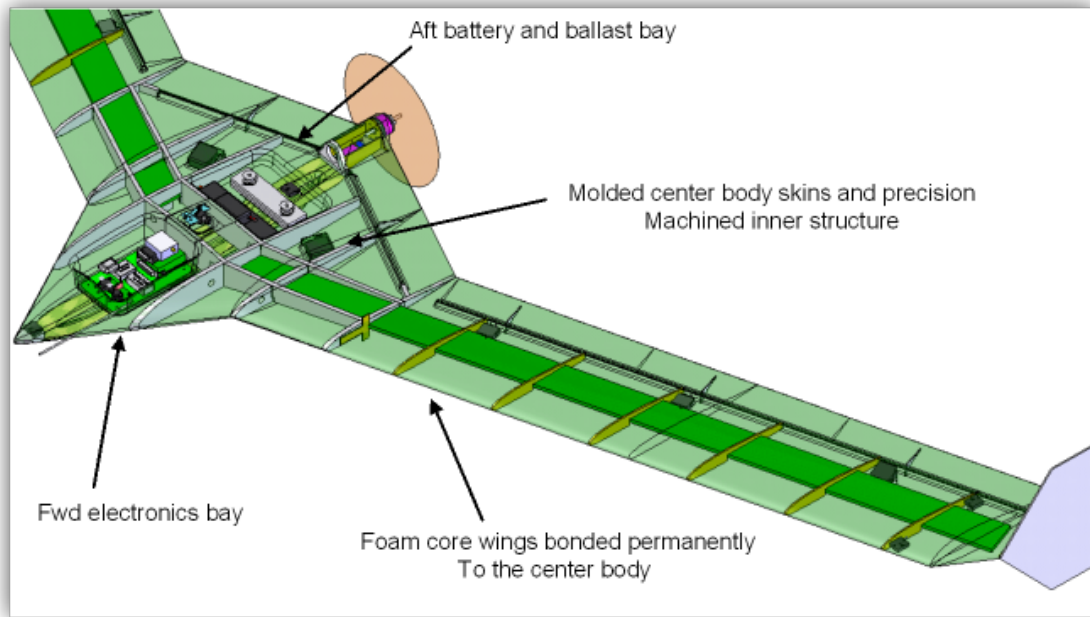
Figure 3.3: Body freedom flutter (BFF) aircraft structure: transparent view [4]

accelerometers located at the wing tips and center body of the vehicle, and hot-film sensors located at the leading-edge stagnation point (LESP) to estimate the lift distribution. The dynamics of these sensors and control surface actuators are incorporated in the ASE models of the vehicle. These models are described in the last section of the chapter.

3.2 Structural Dynamics

As described in the last chapter, modeling of ASE behavior requires the development of a structural model coupled with a consistent aerodynamic model. The BFF nonlinear ASE models are derived based on structural finite elements and lifting-surface theory, both of which are available in general purpose commercial codes [20–22]. This section describes a finite element model developed at the University of Minnesota to predict the structural dynamic response of the BFF aircraft. Following, the identification of modal parameters is presented. Here, a ground vibration test is performed in order to obtain experimental modal data that allows to identify the natural frequencies, damping factors and mode shapes of the structure. These data are then used to validate and improve the accuracy of the structural finite element model.
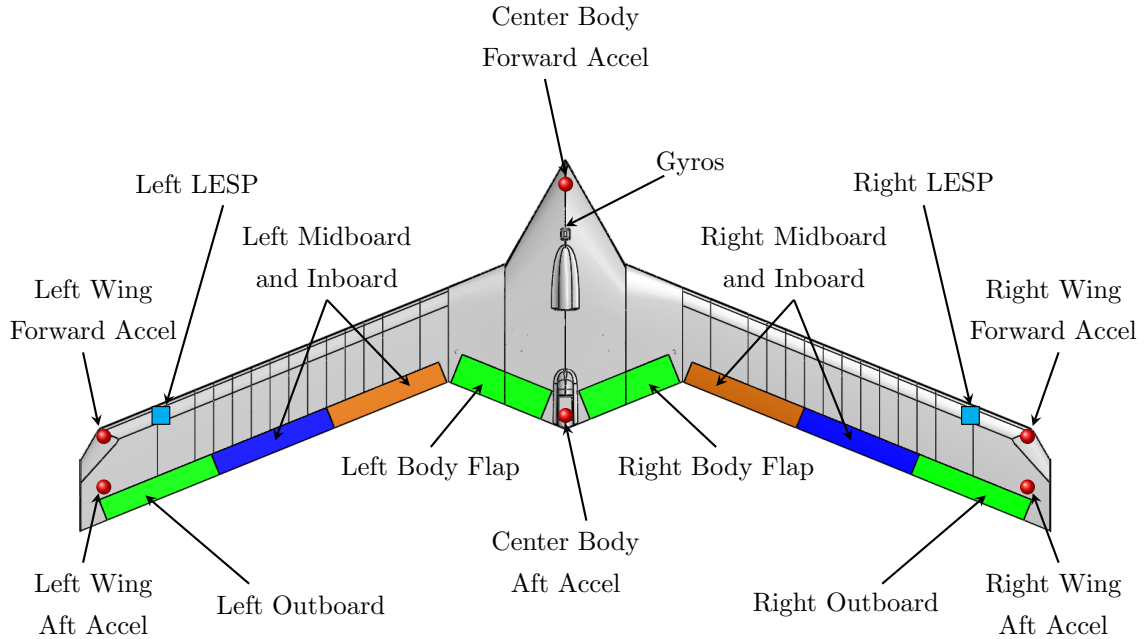
Figure 3.4: Body freedom flutter (BFF) aircraft configuration: control surfaces and sensors suite [5]

3.2.1 Finite Element Model [2]

The finite element method has become in a powerful tool to numerically solve a wide variety of engineering problems. Its popularity among the structural engineering community is the ability to physically model complex geometries and incorporate different materials obtaining accurate solutions in a computational efficient manner. For these reasons, the structural dynamics of the BFF aircraft is modeled using finite elements.

The structure of the BFF vehicle is modeled using one-dimensional elements with axial, bending and torsional properties. These properties correspond to the main load case of the aircraft in flight. A very common element used in these applications is the Euler-Bernoulli beam with added torsional effects. This typical element is shown in Fig. 3.5 where each end i and j, represents a structural node. Observe that the element has three degrees-of-freedom (DOF) at each node. These DOF represent the nodal displacements caused by the bending and torsional load conditions in the aircraft.

The BFF structure, consisting of the wing spars and center body, is discretized based on the vehicle's physical characteristics. These characteristics include the location of control surface actuators, winglets and major electronic components. The discretization results
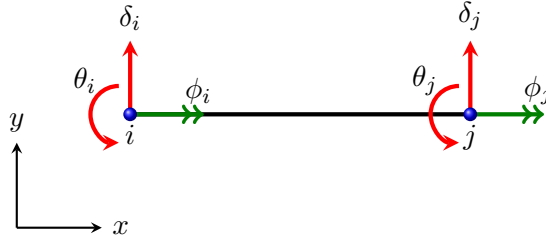
Figure 3.5: Euler-Bernoulli beam element with torsional effects

in a set of 14 nodes connected by 15 beam elements shown in Fig. 3.6. Here, the center body is modeled with equivalent beams between nodes 10-5 and 3-4. Node 2 represents the center of gravity of the aircraft, node 3 the propulsion motor, and node 4 the flight computer location. On the other hand, the wing spar is divided in four elements. These nodes correspond to equivalent locations of actuators for the inboard flaps (6,11), midboard flaps (7,12), and outboard flaps (8,13). Here, point masses are added in order to represent these electronic components. Actuators for the body and outboard flaps weigh approximately 65 g, actuators for the inboard and middle flaps weigh 50 g, winglets are 50 g, batteries 2.25 kg, propulsion motor 200 g and flight computer 150 g. Finally, nodes 9 and 14 represent the winglets of the aircraft. With this, the total length of each swept wing (5-9 or 10-14) is measured as 1.27 m.
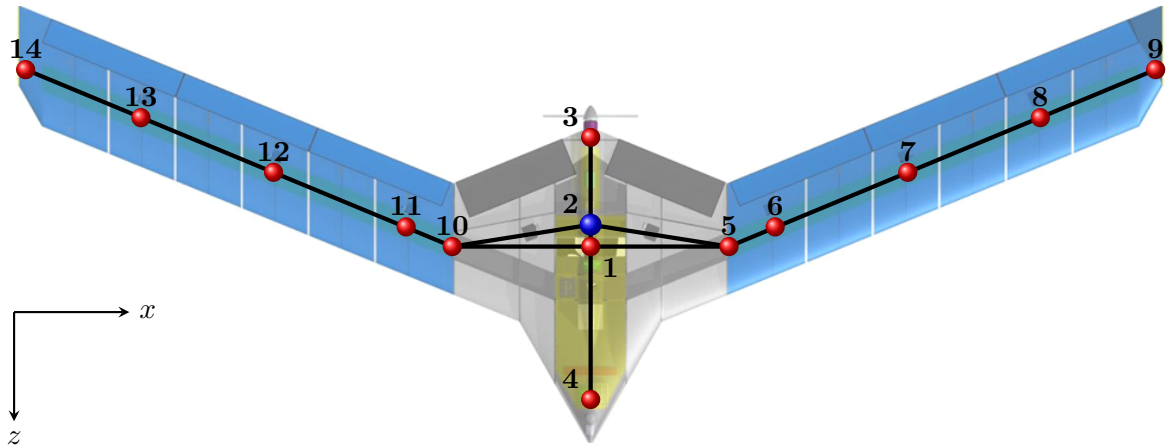
Figure 3.6: Finite element discretization of body freedom flutter (BFF) structure

As mentioned before, the great advantage of the finite element method is the ability to create accurate models of complex structures by assembling the corresponding equations of motion of each element. In this case, the equations of motion of the Euler-Bernoulli beam

14

element are derived for linear elastic materials and small deflection assumptions. These equations correspond to

$$m_e \ddot{q} + k_e q = p_e^c + p_e^{nc} \tag{3.1}$$

where $q = [\delta_i, \theta_i, \phi_i, \delta_j, \theta_j, \phi_j]^T$ is the vector of the nodal displacements, m_e is the mass matrix of the element, k_e is the stiffness matrix of the element, p_e^e is a vector of nodal forces and moments, and p_e^{nc} is the vector of non-conservative forces in the element. Here, the mass and stiffness matrices are given by [41]

$$m_e = \begin{pmatrix} \frac{156\mu L}{420} & \frac{22\mu L^2}{420} & 0 & \frac{54\mu L}{420} & \frac{-13\mu L^2}{420} & 0 \\ \frac{22\mu L^2}{420} & \frac{4\mu L^3}{420} & 0 & \frac{13\mu L^2}{420} & \frac{3\mu L^3}{420} & 0 \\ 0 & 0 & \frac{\chi L}{3} & 0 & 0 & \frac{\chi L}{6} \\ \frac{54\mu L}{420} & \frac{13\mu L^2}{420} & 0 & \frac{156\mu L}{420} & \frac{-22\mu L^2}{420} & 0 \\ \frac{-13\mu L^2}{420} & \frac{-3\mu L^3}{420} & 0 & \frac{-22\mu L^2}{420} & \frac{4\mu L^3}{420} & 0 \\ 0 & 0 & \frac{\chi L}{6} & 0 & 0 & \frac{\chi L}{3} \end{pmatrix} \tag{3.2}$$

$$k_e = \begin{pmatrix} \frac{12EI_z}{L^3} & \frac{6EI_z}{L^2} & 0 & \frac{-12EI_z}{L^3} & \frac{6EI_z}{L^2} & 0 \\ \frac{6EI_z}{L^2} & \frac{4EI_z}{L} & 0 & \frac{-6EI_z}{L^2} & \frac{2EI_z}{L} & 0 \\ 0 & 0 & \frac{GJ_x}{L} & 0 & 0 & \frac{-GJ_x}{L} \\ \frac{-12EI_z}{L^3} & \frac{-6EI_z}{L^2} & 0 & \frac{12EI_z}{L^3} & \frac{-6EI_z}{L^2} & 0 \\ \frac{6EI_z}{L^2} & \frac{2EI_z}{L} & 0 & \frac{-6EI_z}{L^2} & \frac{4EI_z}{L} & 0 \\ 0 & 0 & \frac{-GJ_x}{L} & 0 & 0 & \frac{GJ_x}{L} \end{pmatrix} \tag{3.3}$$

where EI_z represents the bending stiffness around the z-axis, GJ_x the torsional stiffness, and L the length of the element. The elastic and material properties of the elements are represented by the Young modulus E, shear modulus G, section mass per unit length μ, and inertia per unit length χ. The cross section properties of the element correspond to the second area moment around the z-axis, I_z, and the polar moment of inertia around the x-axis, J_x. Notice that each entry of these matrices is associated to a DOF in the vector q. In other words, the entries of the mass matrix can be interpreted as the inertial force resulting from applying an unitary acceleration in a particular DOF direction. Similarly, the entries of the stiffness matrix are interpreted as the static force resulting from an unitary deformation in a particular DOF direction.

Equations (3.2) and (3.3) indicate that the structural dynamics of these beam elements are completely dependent on their geometric and material properties. However, these properties were not provided by the developers of the BFF aircraft. Hence, additional experiments are required to obtain the equivalent static and dynamic properties of the center body and wings. These experimental results, used to build the BFF structural model, are presented in the following subsections.

Wing Static Tests

Static tests are conducted on the aircraft wings to obtain initial estimates of their stiffness properties. This experimental setup is shown in Fig. 3.7. The BFF aircraft wing is fixed with clamps at $1.15\,\mathrm{m}$ from the tip of the wing. An inclinometer that measures the angular deflection in two directions is located at $1\,\mathrm{m}$ from the fixed end. Three weights were applied at two different locations along the wing, $l_1 = 0.9\,\mathrm{m}$ and $l_2 = 0.6\,\mathrm{m}$ from the fixed end. Measurements for bending and torsion deflections are taken by applying eccentric loads at $10\,\mathrm{cm}$ forward the spar axis of the wing. The data analysis resulted in a bending stiffness $EI_z = 70\,\mathrm{N\text{-}m}^2$ and torsion stiffness $GJ_x = 40\,\mathrm{N\text{-}m}^2$.
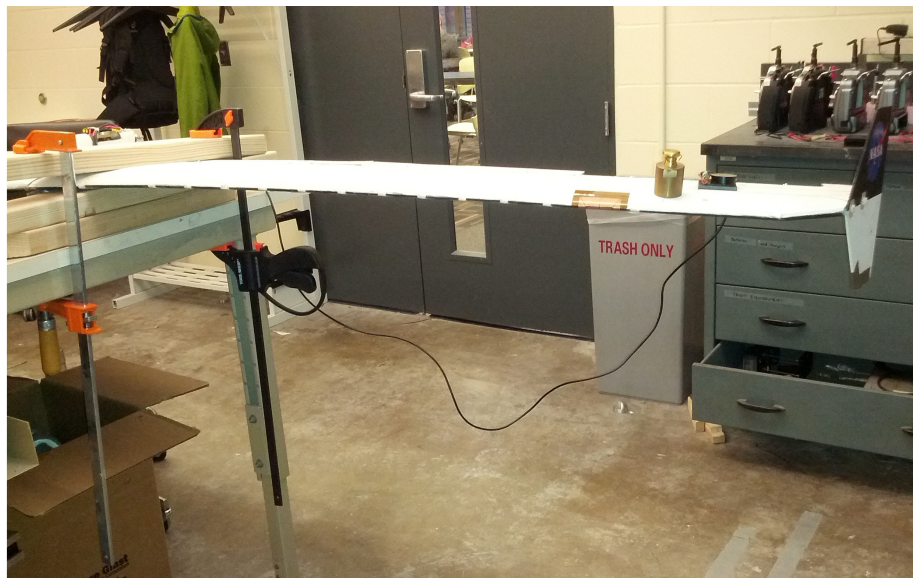
Figure 3.7: Static test setup

Wing Dynamic Tests

An estimation of the mass properties of the wings is obtained from dynamic tests. As in the static test, the aircraft wing is fixed with clamps at $1.15\,\mathrm{m}$ from the tip of the wing. Accelerometers are located at the free end of the wing. One accelerometer is located on the spar axis and another accelerometer is located at $10\,\mathrm{cm}$ forward the spar axis. The experiment consists of applying an initial displacement to the tip of the wing, and recording the time histories of the free vibration measured by the accelerometers. The recorded data is analyzed in the frequency domain in order to identify the fundamental vibration frequencies of the wing. These frequencies are identified from the power spectra of the recorded wing accelerations in free vibration shown in Fig. 3.8. From here, two bending frequencies are identified at $\omega_1 = 21.2\,\mathrm{rad/s}$, $\omega_3 = 150.8\,\mathrm{rad/s}$ and one torsion frequency is identified at $\omega_2 = 116.9\,\mathrm{rad/s}$. Next, the corresponding mass properties of the wing are computed.
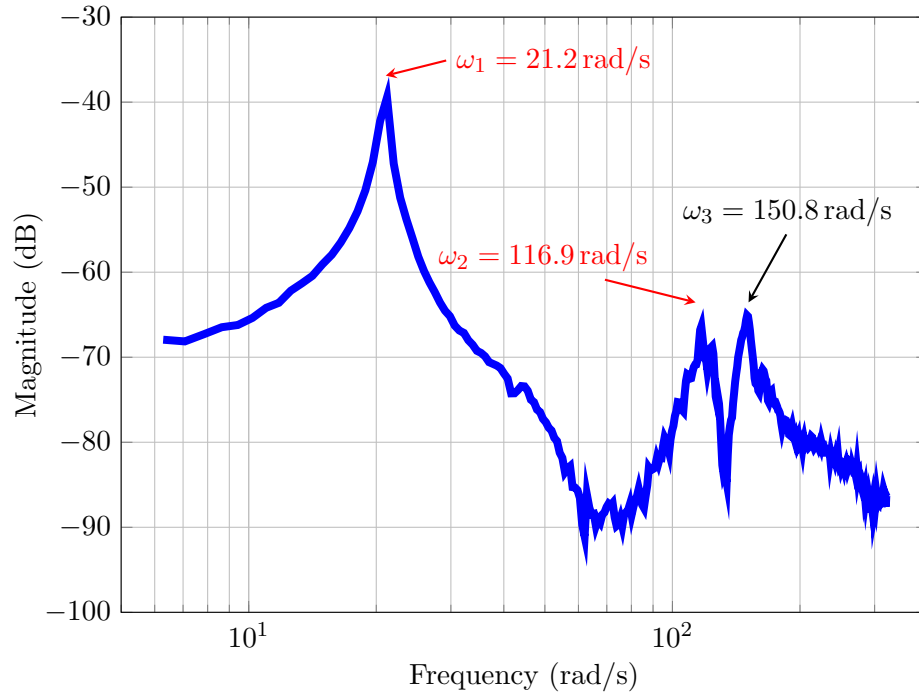
Figure 3.8: Power spectrum of the BFF wing free vibration for eccentric accelerometer

The mass and inertial distribution of the wing can be obtained from the cantilever beam vibration solutions. Here, the fundamental bending frequency is equivalent to $\omega_b = (0.597\pi/L)^2\sqrt{EI_z/\mu}$ where EI_z is the bending stiffness, μ is the mass distribution per unit length, and L is the total length of the cantilever wing. Similarly, the fundamental torsional

17

frequency is $\omega_t = (\pi/2L)\sqrt{GJ_x/\chi}$ where GJ_x is the torsional stiffness and χ is the inertial distribution per unit length. Using the stiffness values previously obtained from the static tests, the mass and inertia properties of the wing are found to be $\mu = 1.0797\,\text{kg/m}$ and $\chi = 0.0054\,\text{kg-m}^2/\text{m}$.

Center of Gravity

An estimation of the center of gravity location for the BFF aircraft was obtained using three scales. Fig. 3.9 shows the experimental setup with one scale located under each winglet and the other scale located under the center body axis. The aft scales were placed $60\,\text{cm}$ from the center body scale. Each scale measurement was recorded to find that the total mass of the aircraft is $m_b = 5.42\,\text{kg}$. The center of gravity location was obtained using the three readings and distances between scales such that $\bar{z} = (m_1 z_1 + m_2 z_2)/m_b$, where m_1 is the sum of the scale measurements under the winglets, m_2 is the scale measurement under the center body axis, z_1 is the distance of the aft scales with respect to the nose, z_2 is the distance of the center body scale with respect to the nose, and m_b is the total mass of the aircraft. From this, the location of the center of gravity is estimated at $\bar{z} = 59\,\text{cm}$ measured with respect to the nose of the vehicle [42].

Aircraft Inertia [42]

The principal moments of inertia of the aircraft were determined via swing tests. The pitch moment of inertia was determined using a compound pendulum approximation while the roll moment of inertia was determined using a bifilar pendulum approach shown in Fig. 3.10. Assuming small deflections during these swing tests, the pitch inertia is equivalent to $I_q = m_b g d/\omega_q^2$ where m_b is the total mass of the aircraft, g is the acceleration due to gravity, d is the distance between the pivot point and the center of gravity, and ω_q is the frequency of the pitching oscillations. On the other hand, the roll inertia is equivalent to $I_p = m_b g d^2/4L^2\omega_p^2$, where d represents the horizontal distance between the two bifilar, L is the length of the bifilar, and ω_p is the frequency of the rolling oscillations. From these tests, the estimated values for the pitching and rolling moments of inertia are $I_q = 0.36\,\text{kg-m}^2$ and $I_p = 2.50\,\text{kg/m}^2$, respectively.

Figure 3.9: Center of gravity test setup. Source: Uninhabited aerial vehicle research laboratory at the University of Minnesota

Figure 3.10: Inertia swings test setup. Source: Uninhabited aerial vehicle research laboratory at the University of Minnesota

Aircraft Vibration Analysis

The vibration analysis of the entire aircraft structure is performed by assembling the dynamic equations of all the elements in Fig. 3.6. These equations have the form

$$M\ddot{Q} + KQ = P^c + P^{nc} \tag{3.4}$$

where $M = \sum m_e$ is the global mass matrix, $K = \sum k_e$ is the global stiffness matrix, Q is the vector of all DOF in the structure, and P^c and P^{nc} are the total nodal conservative and non-conservative forces and moments in the structure. Eq. (3.4) represents N coupled differential equations where N is the number of degrees-of-freedom [43]. Here, the dynamic properties of the structure are represented by its natural frequencies and natural modes of vibration. These concepts are introduced next.

The concepts of natural frequency and vibration mode are derived from the free vibration condition in structures. A structure is said to be undergoing free vibration when it is disturbed from its static equilibrium position and then allowed to vibrate without any external dynamic excitation. This condition is governed by the differential equations [44]

$$M\ddot{Q} + KQ = 0 \tag{3.5}$$

Here, the solution $Q(t)$ satisfies the initial conditions $Q(0) = Q_0$ and $\dot{Q}(0) = \dot{Q}_0$. This solution can also be described mathematically by

$$Q(t) = \sum_{n=1}^{N} \phi_n \eta_n(t) \tag{3.6}$$

where ϕ_n is the deflected shape, called also the vibration mode, and $\eta_n(t)$ is the harmonic function

$$\eta_n(t) = A_n \cos \omega_n t + B_n \sin \omega_n t \tag{3.7}$$

with natural frequency vibration ω_n.

By substituting (3.6) in (3.5), the following eigenvalue problem is generated

$$\left[-\Omega^2 M\Phi + K\Phi \right] \eta(t) = 0 \tag{3.8}$$

where Ω^2 is a diagonal matrix with N natural frequencies ω_n^2 as

$$\Omega^2 = \begin{bmatrix} \omega_1^2 & & & \\ & \omega_2^2 & & \\ & & \ddots & \\ & & & \omega_N^2 \end{bmatrix} \tag{3.9}$$

20

and Φ is the modal matrix of the system assembled with the eigenvectors associated to each natural frequency ω_n. That is

$$\Phi = \begin{bmatrix} \phi_1 & \phi_2 & \cdots & \phi_N \end{bmatrix} \tag{3.10}$$

This solution also implies that the following matrices are diagonal

$$\hat{K} = \Phi^T K \Phi$$
$$\hat{M} = \Phi^T M \Phi \tag{3.11}$$

with diagonal elements corresponding to

$$K_n = \phi_n^T K \phi_n$$
$$M_n = \phi_n^T M \phi_n \tag{3.12}$$

Here, K_n is called the modal stiffness and M_n is called the modal mass associated to the natural frequency ω_n. Next, the modal properties of the BFF aircraft are presented.

The natural frequencies and modal shapes of the BFF aircraft are summarized in Table 3.1. These results are computed by solving the eigenvalue problem in (3.8) with the finite element global mass and stiffness matrices of the structure. Here, the first six fundamental structural modes are presented.

Table 3.1: Natural frequencies and modal masses from finite element model of BFF aircraft

Mode Shape	Frequency [rad/s]	Modal Mass [kg-m^2]
1st Symmetric Bending	34.89	0.297
1st Anti-Symmetric Bending	53.26	0.348
1st Symmetric Torsion	108.84	0.008
1st Anti-Symmetric Torsion	106.57	0.008
2nd Symmetric Bending	163.19	0.052
2nd Anti-Symmetric Bending	183.62	0.057

The mode shapes corresponding to the natural frequencies listed in Table 3.1 are depicted in Fig. 3.11, Fig. 3.12, and Fig. 3.13. Here, the blue lines denote vertical displacements in the y-axis and the green lines denote torsional angles around the x-axis. Notice that the bending vibration modes exhibit both vertical and torsional deflections. This behavior is observed because the swept wings cause eccentric loading in the xz-plane. On the other hand, it is observed that the torsional vibration modes exhibit pure torsional deflections. In this case, the sweep angle does not cause any vertical displacement.
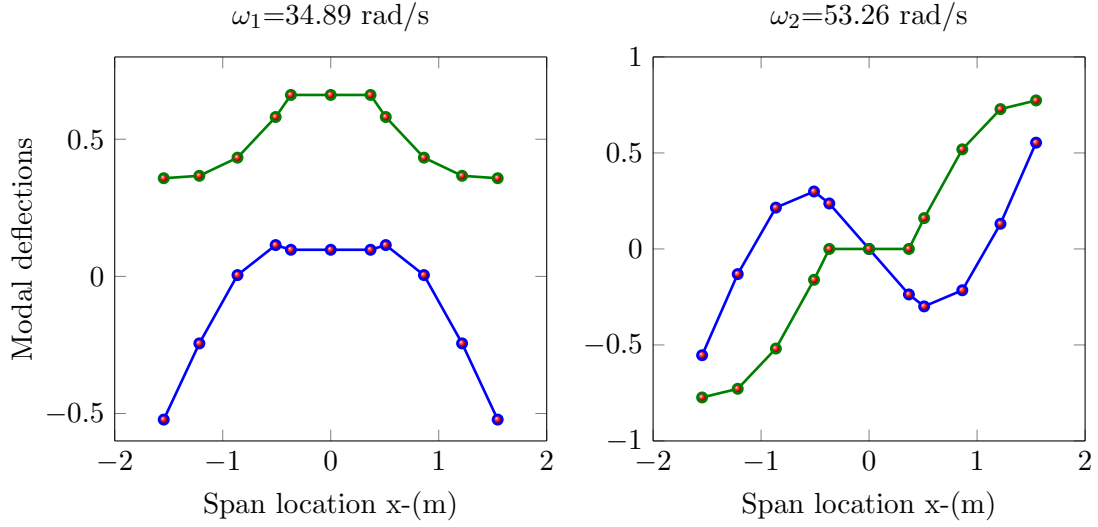
Figure 3.11: First symmetrical (ω_1) and anti-symmetrical (ω_2) bending modes. Vertical displacements y-(m) are represented by (——•——) and torsional angle deflections ϕ-(rad) are represented by (——•——).
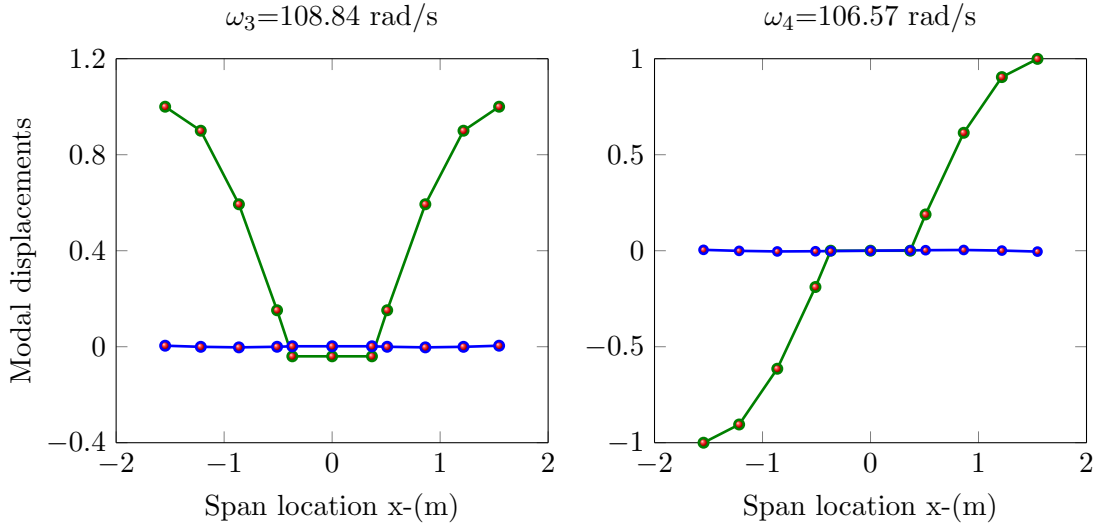
Figure 3.12: First symmetrical (ω_3) and anti-symmetrical (ω_4) torsion modes. Vertical displacements y-(m) are represented by (——•——) and torsional angle deflections ϕ-(rad) are represented by (——•——).

In general, the natural frequencies and modal shapes presented in Table 3.1 are known as the structure's undamped modal properties. This means that the structure oscillates
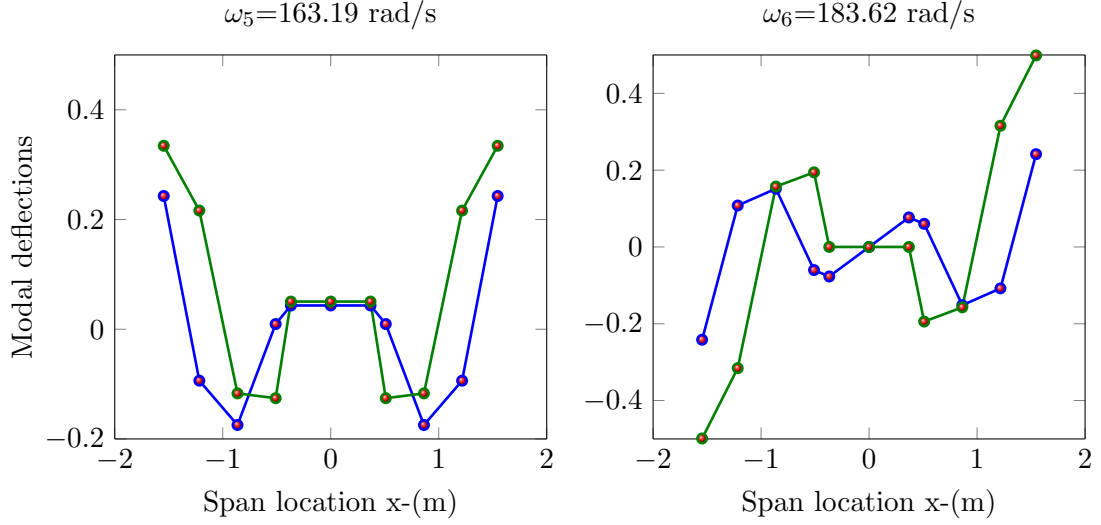
Figure 3.13: Second symmetrical (ω_5) and anti-symmetrical (ω_6) bending modes. Vertical displacements y-(m) are represented by (——) and torsional angle deflections ϕ-(rad) are represented by (——).

indefinitely at the frequency ω_n if no external force is applied. However, real structures dissipate this oscillation energy through several mechanisms. Then, these non-conservative forces P^{nc} can be included in the system as damping forces by re-writing the equations of motion in (3.4) as

$$M\ddot{Q} + \Xi\dot{Q} + KQ = P^c \tag{3.13}$$

where C is the damping matrix of the structure. This damping matrix can also be diagonalized using the eigenvectors of the system as

$$\hat{\Xi} = \Phi^T \Xi \Phi \tag{3.14}$$

where the diagonal elements correspond to

$$\Xi_n = \phi_n^T \Xi \phi_n = 2M_n \zeta_n \omega_n \tag{3.15}$$

where ζ_n is defined as the damping ratio associated to ω_n. Damping ratios are a measure of how modal oscillations decay in time and are usually estimated from ground vibration tests. This test is explained in the following subsection.

3.2.2 Ground Vibration Test [3]

A ground vibration test is performed in order to determine the aircraft structural response to a sweep sine force excitation. The goal is to use this input-output data to identify the

23

modal parameters of the flexible structure. Identifying these parameters is key for updating and validating the finite element structural model. The following subsections present the experimental procedure and data analysis for the modal identification of the BFF aircraft.

Boundary Conditions

A vibration test would ideally occur with the vehicle freely suspended in space. In practice, however, a truly free support is not feasible because the structure needs to be held in some way. This condition can be approximated by supporting the test structure on very flexible springs such that the rigid body modes do not interfere with the flexible modes [45].

The BFF free condition is reproduced using a very flexible spring such that the highest rigid body mode frequency is less than 20% of the fundamental frequency of the aircraft. Because the fundamental frequency of the structure ω_n is approximately 30 rad/s, the frequency of the mass-spring system ω_r must not exceed 6 rad/s. Recall that the mass of the aircraft is $m_b =5.42$ kg. Hence, the maximum stiffness of the spring required to achieve an almost free condition is $k = m_b\omega_r^2 = 195$ N/m. Here, a commercial spring that can support the structure with the specified or less stiffness will achieve the desired boundary condition. Then, a stainless steel spring with a maximum load resistance of 11.2 kg and stiffness of 130 N/m is selected to suspend the aircraft from a rigid frame as shown in Fig. 3.14.

Data Acquisition Equipment

All the equipment used for this experiment is available at the Aeromechanics Laboratory of the University of Minnesota. An Unholtz-Dickie Model 20 electrodynamic shaker is used to provide a known excitation to the structure. This shaker can apply forces up to 1103 N at frequencies between 1-5000 Hz. The shaker is connected to the aircraft through an excitation stinger. This stinger transmits the excitation force axially and reduces lateral forces applied to the structure. In addition, a PCB 208C01 force sensor is mounted between the stinger and the structure to measure the excitation force. This sensor can measure forces of ± 44.5 N between a frequency range of 0.01-36000 Hz with a sensitivity of 112.41 mV/N.

The structural response of the aircraft is measured using two PCB 353B16 miniature accelerometers located at several points along the aircraft. The measurement range of these accelerometers is ± 500 g between the frequencies 1-10000 Hz. These sensors have a sensitivity of 10 mV/g. The acceleration signals are then amplified using two PCB 480E09 signal conditioners. The voltage amplification gains of these conditioners correspond to factors of 1 and 10. Finally, the excitation signals and experimental transfer functions between the
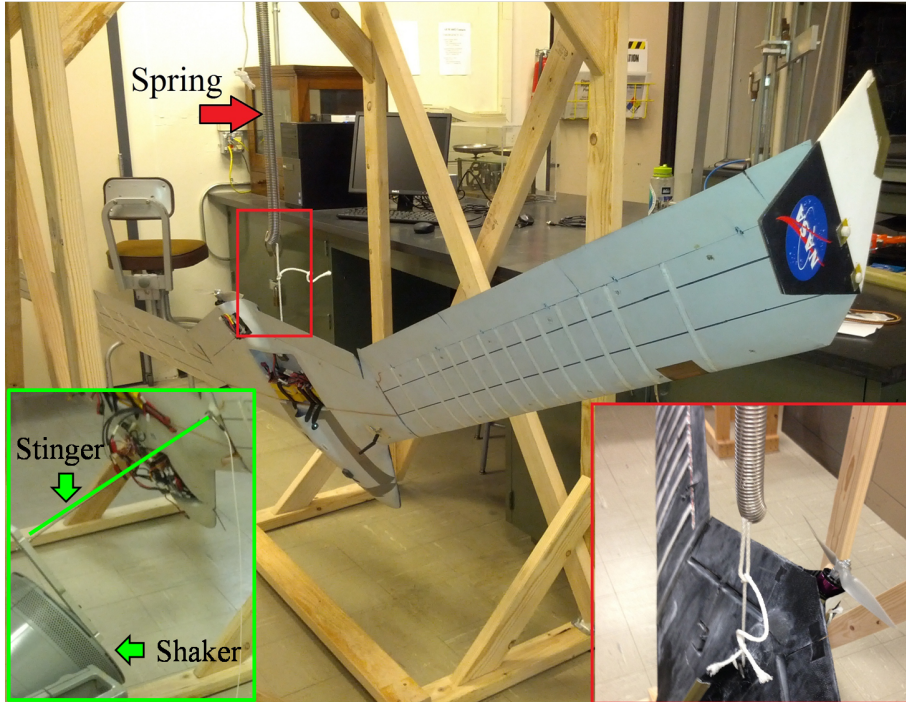
Figure 3.14: Test setup: suspended aircraft with vibration exciter shaker

force applied by the shaker and the acceleration at the different points are calculated using a HP35670A Dynamic Signal Analyzer with 400-data point frequency resolution [46, 47].

Experimental Procedure

Fig. 3.15 shows the experimental procedure to obtain the structural dynamic response of the BFF aircraft. Here, the aircraft is excited with a sine sweep wave from 3 to 35 Hz (20-220 rad/s). A sampling rate of 74 Hz (465 rad/s) is chosen by the analyzer to perform the test. This sampling rate allows to determine the structure natural frequencies below 220 rad/s. Acceleration responses are measured at 34 points distributed along the wing and center body of the vehicle (3.16). Point 12 was selected as the excitation location. It is expected that vibrations applied in this asymmetric point will excite the symmetric and anti-symmetric modes of the structure.

Single input, single output (SISO) frequency responses from applied force to acceleration response are obtained at each location using the dynamic analyzer. The frequency responses contain 400 data points and are computed in the swept-sine analyzer mode. Force and acceleration signals are measured at a constant frequency to calculate each point of the frequency response.
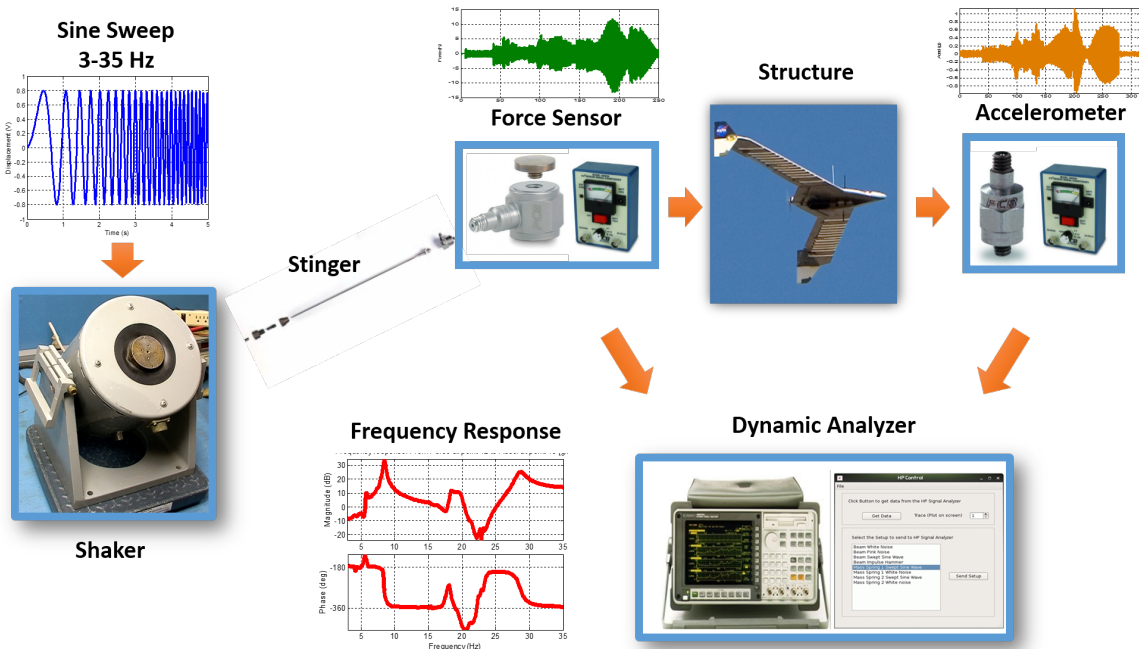
Figure 3.15: Experimental procedure to obtain vibration data
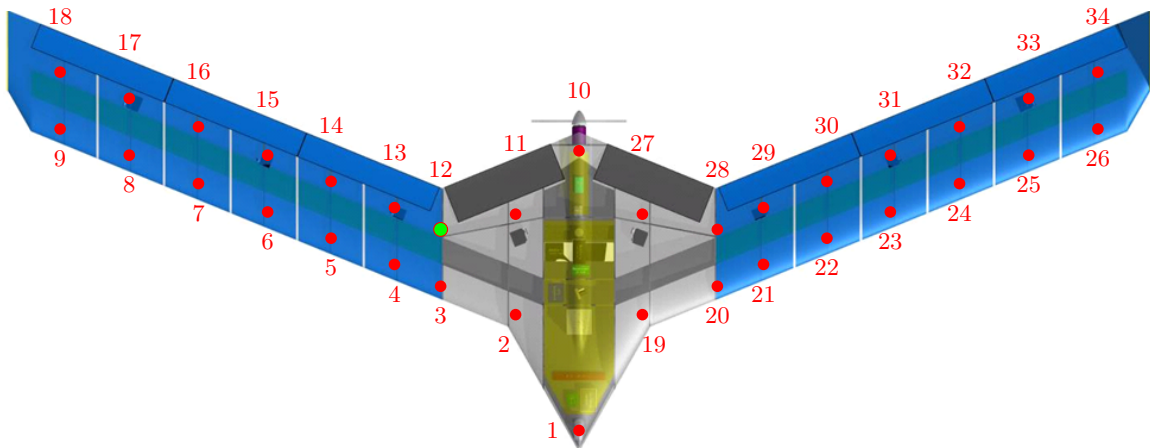
Figure 3.16: Accelerometers location (●) and input excitation location (●) [4]

An experimental frequency response obtained from the anti-symmetric input to the acceleration response at the tip of the wing is shown in Fig. 3.17. Peaks in the magnitude response and 180° phase changes denote the identification of several modes. In particular the structure has two closely spaced modes between 110 and 130 rad/s. These experimental data are used to obtain the modal parameters of the aircraft structure as described in the following section.

26
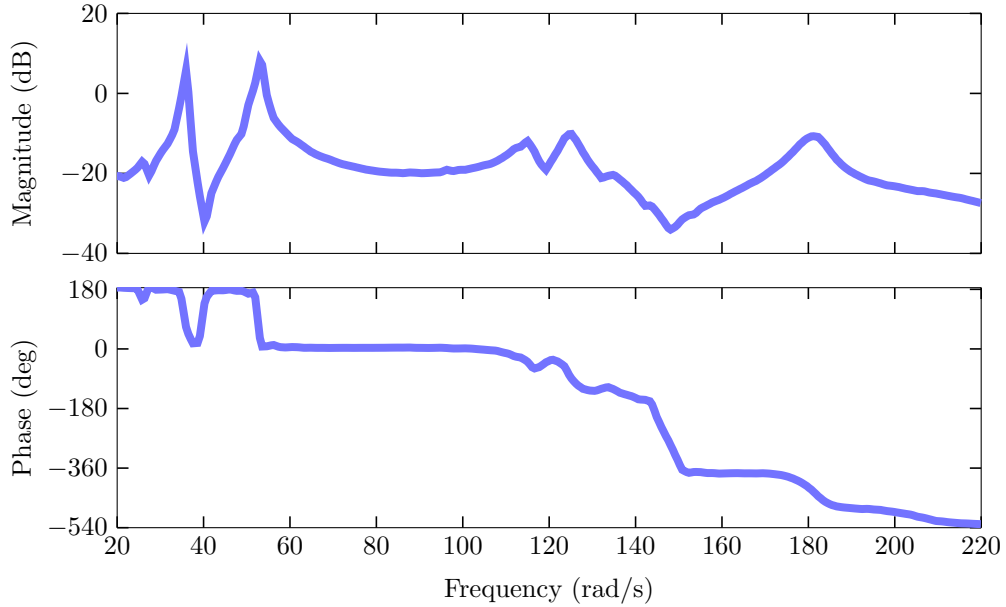
Figure 3.17: Experimental frequency response: From force [N] at point 12 to acceleration [g] at point 18

3.2.3 Modal Identification

The modal identification of the BFF aircraft is formulated as a system identification problem where the objective is to build mathematical models of dynamic systems based on data observations. The construction of these models involves three entities: (i) recorded experimental input-output data, (ii) selection of a mathematical modeling framework, and (iii) choice of system identification algorithms that will yield the best model fitting of the observed data [48].

In this work, state-space models are selected to describe the structural dynamic system. These mathematical models can accurately describe the linear dynamics and can provide physical insight regarding the system. Because the measurement data is usually sampled for computational applications, discrete-time state-space models are better suited for system identification purposes. Moreover, state-space models form the basis for many modern control design methods. The versatility of state-space models is the reason to select them to describe the structural dynamics of the aircraft.

A discrete-time, state-space models for identification and control is generally described

by

$$x(k+1) = \check{A}x(k) + \check{B}u(k) + w(k),$$
$$y(k) = \check{C}x(k) + \check{D}u(k) + v(k) \tag{3.16}$$

where $u(k)$ and $y(k)$ are the input and output vector measurements at time instant k, $x(k)$ is the state vector and $w(k)$, $v(k)$ unmeasurable signals representing the noise in the system. $\check{A}$ is the dynamic system matrix, $\check{B}$ the input matrix, $\check{C}$ the output matrix and $\check{D}$ the direct feed-through term.

The state-space representation described by (3.16) has been the subject for the development of several system identification methods [48, 49]. In this case, the state-space identification method selected for modal parameter estimation of the BFF aircraft is based on subspace identification algorithms. These algorithms use system theory and linear algebra concepts to reveal important characteristics of the system. Because these concepts also provide an understanding of the aircraft as a control system, they fit better for state-space model identification.

One particular subspace algorithm proposed in the literature is the eigensystem realization algorithm (ERA) [49]. The ERA was originally developed for identification of lightly damped systems. Hence, this algorithm is very adequate for the identification of the structural modal parameters of the BFF aircraft. The following subsection presents the modal identification results for the BFF aircraft using the ERA subspace algorithm. The mathematical aspects of the algorithm are discussed below.

The ERA assumes deterministic models to directly compute a state-space model from the measured input-output data. A deterministic system is a system in which process noise w_k and measurement noise v_k are zero. Hence, the state-state model in (3.16) is simply

$$x(k+1) = \check{A}x(k) + \check{B}u(k),$$
$$y(k) = \check{C}x(k) + \check{D}u(k) \tag{3.17}$$

Here, the identification problem consists on determining the system matrices $\check{A} \in \mathbb{R}^{n \times n}$, $\check{B} \in \mathbb{R}^{n \times m}$, $\check{C} \in \mathbb{R}^{l \times n}$, and $\check{D} \in \mathbb{R}^{l \times m}$ with a given set of input measurements $u(k)$ and output measurements $y(k)$. The solution to this problem is obtained by exploiting the relationship between the impulse response of the structure and its system dynamics. This relationship is revealed by constructing the Hankel matrix of the experimental impulse response. In linear algebra, a Hankel matrix is a matrix with constant skew-diagonals such

that

$$H(k-1) = \begin{bmatrix} y(k) & y(k+1) & \cdots & y(k+p) \\ y(k+1) & \ddots & & \vdots \\ \vdots & & \ddots & \vdots \\ y(k+r) & \cdots & \cdots & y(k+p+r) \end{bmatrix} \tag{3.18}$$

where p and r are the number of columns and rows of the Hankel matrix, respectively. Next, the impulse response $y(k)$ is analyzed.

The output $y(k)$ of the deterministic system in (3.17), with initial condition $x(0) = 0$, to an impulse input $u(0) = 1$ is given by

$$\begin{aligned} y(0) &= \breve{D}, \\ y(k) &= \breve{C}\breve{A}^{k-1}\breve{B} \end{aligned} \tag{3.19}$$

Consequently, the Hankel matrix of this impulse response evaluated at $H(0)$ has the form

$$H(0) = \begin{bmatrix} \breve{C} \\ \breve{C}\breve{A} \\ \vdots \\ \breve{C}\breve{A}^{k+r} \end{bmatrix} \begin{bmatrix} \breve{B} & \breve{A}\breve{B} & \cdots & \breve{A}^{k+p}\breve{B} \end{bmatrix} \tag{3.20}$$

where

$$\mathcal{C}_r = \begin{bmatrix} \breve{C} \\ \breve{C}\breve{A} \\ \vdots \\ \breve{C}\breve{A}^{k+r} \end{bmatrix} \tag{3.21}$$

is the controllability matrix of the system and

$$\mathcal{O}_p = \begin{bmatrix} \breve{B} & \breve{A}\breve{B} & \cdots & \breve{A}^{k+p}\breve{B} \end{bmatrix} \tag{3.22}$$

is the observability matrix of the system.

Now, the system matrices can be obtained by performing a singular value decomposition of the Hankel matrix such that $H(0) = U\Sigma V^T$. Here, U and V are the left and right singular vectors and Σ is a diagonal matrix containing the singular values. The order n of the system to identify is obtained by eliminating relatively small singular values from Σ. Hence, the condensed matrices Σ_n, U_n, V_n are used to find a discrete-time, state-space realization

$$\begin{aligned} \breve{A} &= \Sigma_n^{-1/2}U_n H(1) V_n \Sigma_n^{-1/2} \\ \breve{B} &= \Sigma_n^{-1/2}V_n^T [I\ 0] \\ \breve{C} &= [I\ 0]^T U_n \Sigma_n^{-1/2} \\ \breve{D} &= y(0) \end{aligned} \tag{3.23}$$

where the natural frequencies and modal damping factors are the solution for the eigenvalues of the state matrix $\breve{A}$ in its continuous time representation. That is, $\lambda_{c_i} = ln(\lambda_i)/dt$ where λ_i are the discrete-time system eigenvalues, λ_{c_i} are the continuous time system eigenvalues, and dt is the time step. Then, the modal frequencies ω_i and damping ratios ζ_i correspond to

$$\omega_i = |\lambda_{c_i}|$$
$$\zeta_i = \frac{\Re(\lambda_{c_i})}{|\lambda_{c_i}|} \tag{3.24}$$

For good results, the columns of the Hankel matrix p should be selected to be at least ten times the number of modes to be identified, and the rows r should be selected to be 3-5 times p [49, 50].

On the other hand, the realization of the system obtained in (3.23) is not unique because the system matrices depend on the size of the Hankel matrix $H(0)$. Therefore, the system identification can be refined by minimizing the model prediction error. This optimization problem is formulated as

$$I_N(G) = \sum_{k=1}^{N} [y(k) - G(z)u(k)]^2 \tag{3.25}$$

where N is the number of samples and $G(z)$ is the complex frequency response of the discrete system

$$G(z) = \breve{C}\left(zI - \breve{A}\right)^{-1}\breve{B} + \breve{D} \tag{3.26}$$

with z as the discrete Laplace variable. Hence, the optimized discrete system $G^*(z)$ is used to compute the corresponding modal frequencies and damping ratios in (3.24). Following, the results for the BFF aircraft structural identification are presented.

Results

The natural frequencies of the vehicle are determined using the described eigensystem realization algorithm (ERA). Here, the impulse response functions $y(k)$ are computed as the inverse Fourier transform of each collected experimental frequency response. The Hankel matrix is assembled using 601 samples of the impulse response, corresponding to 500 rows and 150 columns of the matrix.

Individual SISO state-space models with 12 states are estimated for each sensor measurement, leading to 34 models. The order of the systems is selected based on the number of modes to identify. The natural frequencies are determined, and are presented in the scatter

plot in Fig. 3.18. Six flexible modes, visualized by the vertical patterns, are identified with these set of measurements. Note that not all of the six modes are identified in each SISO system. These results probably correspond to measurements located at or very close to the nodes of some modes, where their contribution is very small and as consequence, they are not seen in the response.
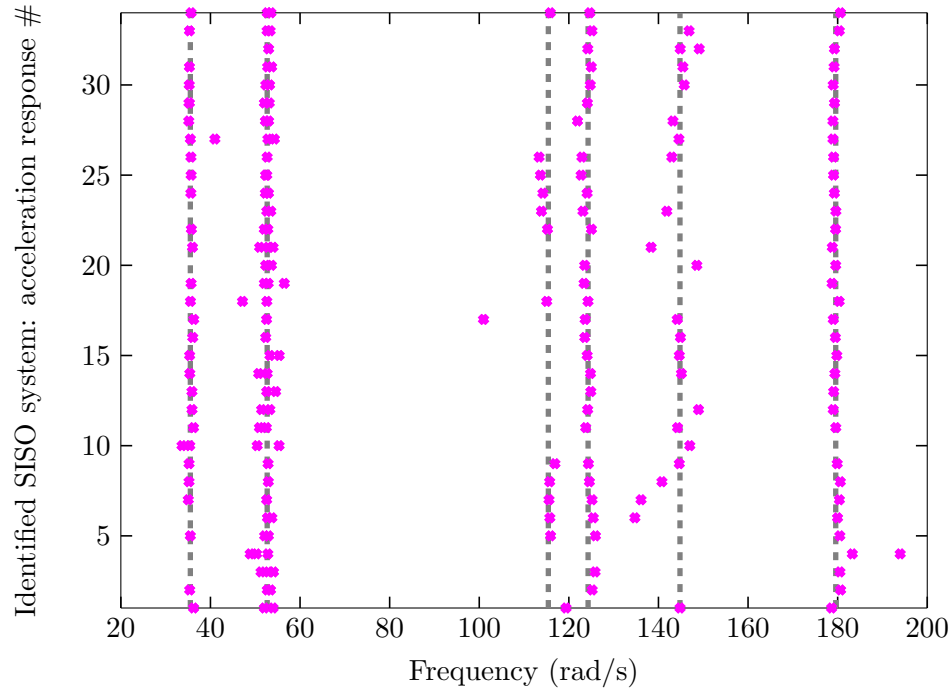
Figure 3.18: Identified natural frequencies (vertical patterns - - - /*) for identified transfer functions from the force sensor at point 12 to acceleration response at 34 points in the aircraft

An initial estimate of the natural frequencies of the structure is obtained by averaging the values corresponding to each identified vertical pattern. The natural frequencies obtained are 35.51, 52.66, 115.42, 124.30, 144.81 and 179.57 rad/s as depicted by the dashed line in Fig. 3.18. Having estimated the modal frequencies, the next step is to find a structural model that reproduces the dynamic behavior of the aircraft at all 34 locations upon excitation at the location 12. This model will be used for tuning and updating the finite element model described in the previous subsection.

A single input, multiple output structural model is estimated using the MATLAB System Identification Toolbox [51]. A non-iterative subspace approach, combined with numerical optimization of the prediction error, is performed to estimate the model. A state-space

model with 20 states was found suitable to capture the six flexible modes initially estimated by ERA. The order of the multiple output model is higher than the order required for the SISO state-space models. This result shows that modeling of multiple output systems is more challenging because input-output couplings involve more complex models and require additional parameters to obtain a good fit [52].

Fig. 3.19 and Fig. 3.20 compare the frequency response of the measured experimental data and the estimated state-space system from the force inputs to two acceleration outputs. It is observed that the estimated model successfully captures the major modal contributions to the system response.

From: Force at point 12 To: Accel at point 16
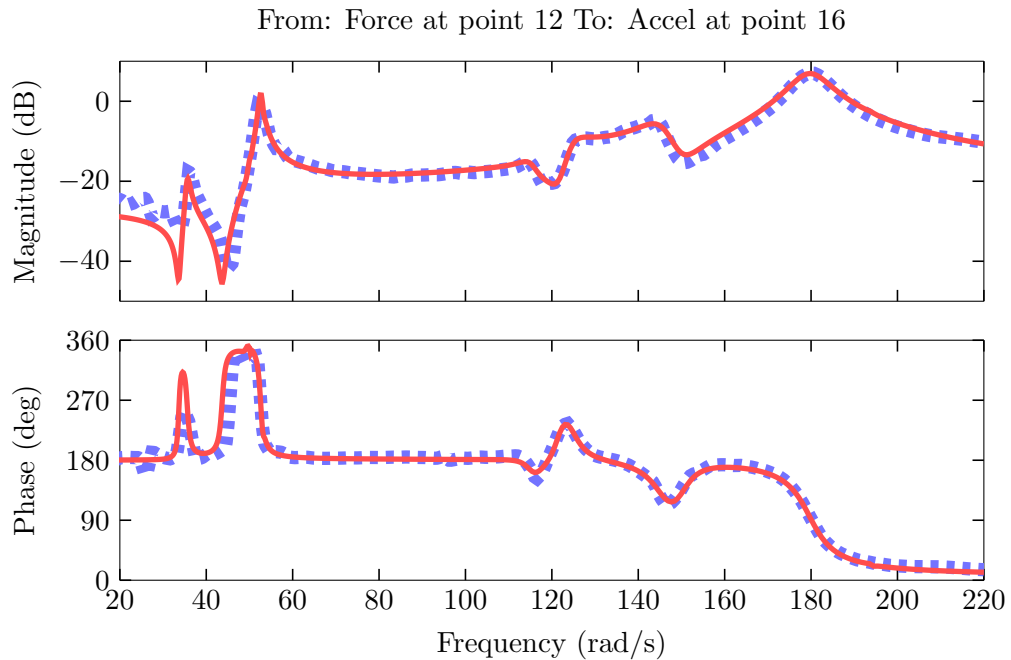
Figure 3.19: Frequency response of experimental data (▪▪▪) and identified system (▬) from force [N] at point 12 to acceleration response [g] measured at point 16

Mode shapes of the structure are determined using the quadrature picking technique [53, 54]. In lightly damped structures, the response at a particular natural frequency is completely dominated by the corresponding mode. This implies that the response of the structure is governed by its imaginary part. The relative modal displacement at each point is obtained by evaluating the frequency response function at a particular natural frequency and examining the magnitude and direction of its imaginary part.

Fig. 3.21 sketches the identified mode shapes and associated natural frequencies of the aircraft. In addition, Table 3.2 lists the frequency values and damping factors corresponding
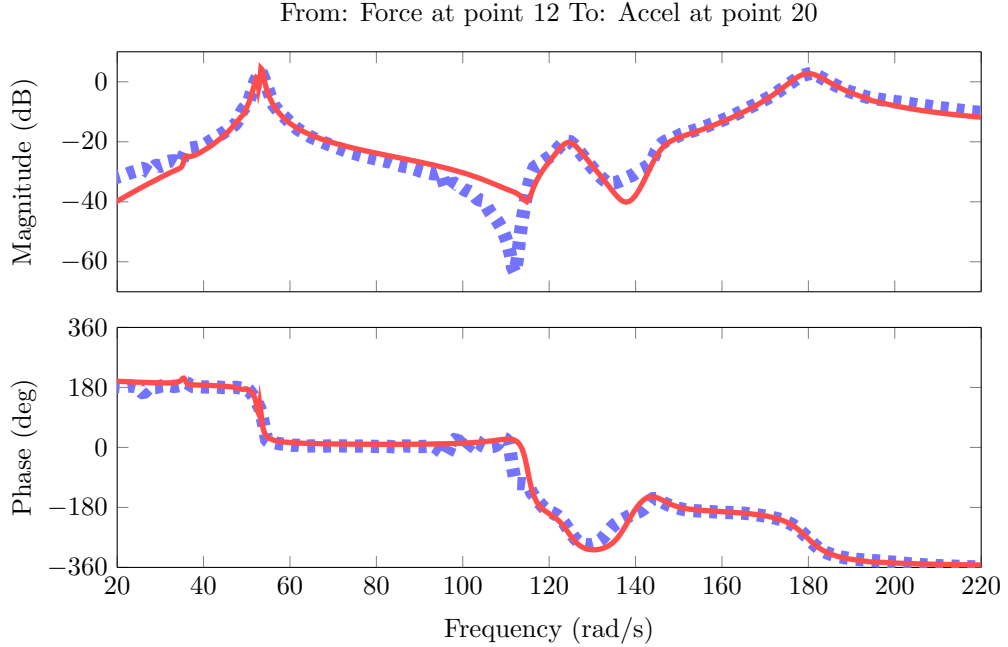
Figure 3.20: Frequency response of experimental data (▪▪▪) and identified system (—) from force [N] at point 12 to acceleration response [g] measured at point 20

to each mode shape identified by the state-space model.

Table 3.2: Natural frequencies, damping factors and modal shapes

Modal Shape	Frequency [rad/s]	Damping [%]
1st Symmetric Bending	35.60	1.55
1st Anti-Symmetric Bending	52.61	1.06
1st Symmetric Torsion	115.27	2.06
1st Anti-Symmetric Torsion	124.56	2.33
2nd Symmetric Bending	145.59	2.85
2nd Anti-Symmetric Bending	179.70	2.55

Validation

Model validation is performed using two techniques, the normalized root mean square error (NRMSE) and the ν-gap metric. The evaluation criteria to determine if the estimated model is a good representation of the real system is based on comparing the frequency response predicted by the model and the measured data.
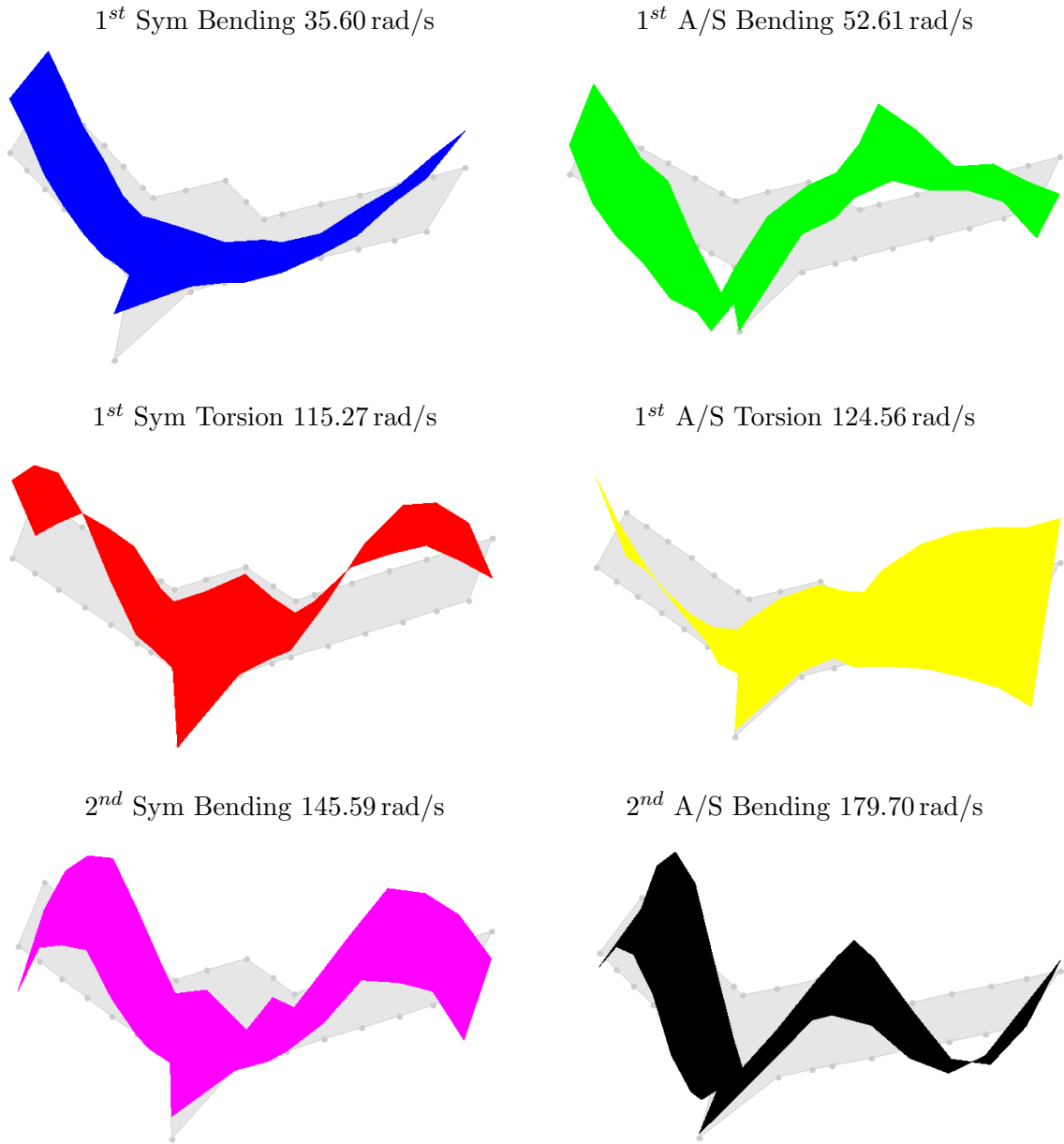
Figure 3.21: Identified mode shapes

The accuracy of the estimated model using the NRMSE is calculated as

$$\%\text{fit} = 100 \left(1 - \frac{\|y - \hat{y}\|_2}{\|y - \text{mean}(y)\|_2} \right) \tag{3.27}$$

where y is the measured frequency response data and $\hat{y}$ is the predicted frequency response of the model. Here, a value of 100% indicates a perfect fit [52].

Fig. 3.22 shows the percentage of the input-output frequency response that the estimated

model represents. Literature reports five evaluation criteria to categorize the goodness of an estimated model. Fit values > 70% are excellent models, > 40% good models and > 20% poor models [55]. A 70% fit value is chosen to accept the model as a good representation of the aircraft structural dynamics.
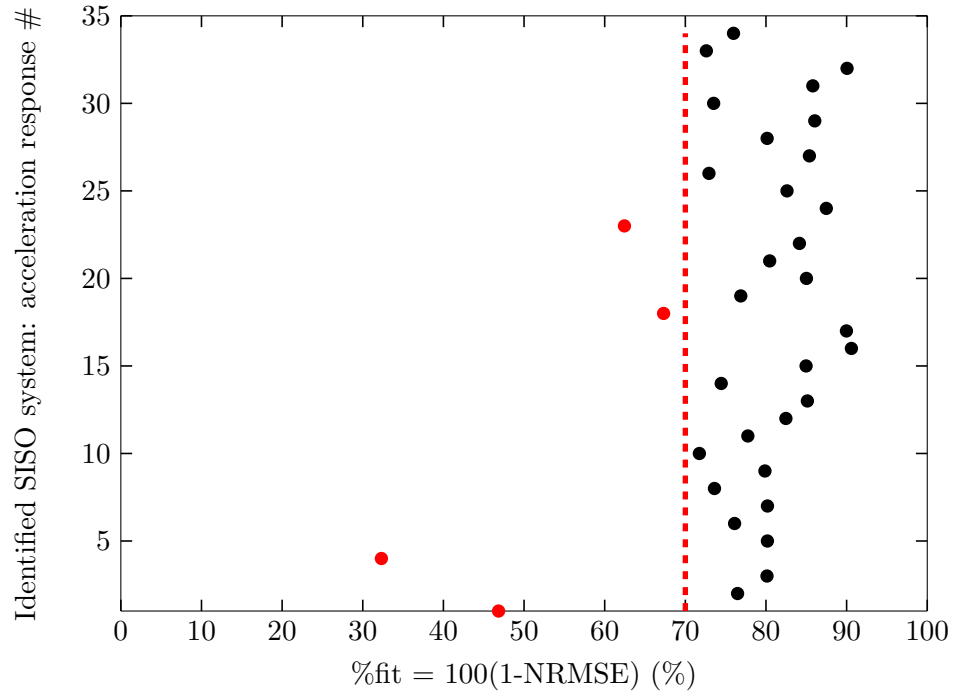
Figure 3.22: Percentage of the input-output frequency response represented by the estimated model. A fit of 70% (---) means that the input-output behavior is reproduced with good accuracy.

It is observed that the estimated model has four input-output frequency responses below the 70% threshold value. This means that the dynamic behavior for those input-output responses is hard to reproduce by the model. This situation can be a consequence of input-output couplings and poor measured data.

Because the model validation using NRMSE is based on the accuracy of each input-output pair, i.e. SISO system, a different metric that evaluates the accuracy of the estimated model in a multiple input, multiple output (MIMO) framework is proposed.

The ν-gap metric is proposed to validate the model in a MIMO framework. This metric provides a measure of the distance between two linear systems in a feedback context. Two systems are considered to be close in the gap metric if, given any stable input-output pair of the first system, there is a corresponding stable input-output pair of the second system that

is close to it. The ν-gap metric between two linear systems $G_1(j\omega)$, $G_2(j\omega)$ is calculated in the frequency domain as

$$\delta(G_1, G_2)(j\omega) = (1 + G_2 G_2^*)^{-\frac{1}{2}} (G_2 - G_1) (1 + G_1 G_1^*)^{-\frac{1}{2}} \tag{3.28}$$

where $\delta(G_1, G_2)(j\omega)$ lies within the interval $[0, 1]$. Values close to zero indicate the two systems are identical and values close to 1 that the systems are far apart [56]. More details about this metric will be given in following chapters.

Fig. 3.23 shows the distance between the estimated model and the experimental data over the frequency range of interest, i.e. 35-185 rad/s. A ν-gap metric of 0.3 is selected as threshold to determine the goodness of the estimated model. It is observed that the ν-gap metric is below the 0.3 threshold across the frequency range identified. This means that the multiple output estimated model with 20 states is a good representation of the aircraft structural dynamics in the bandwidth of interest.
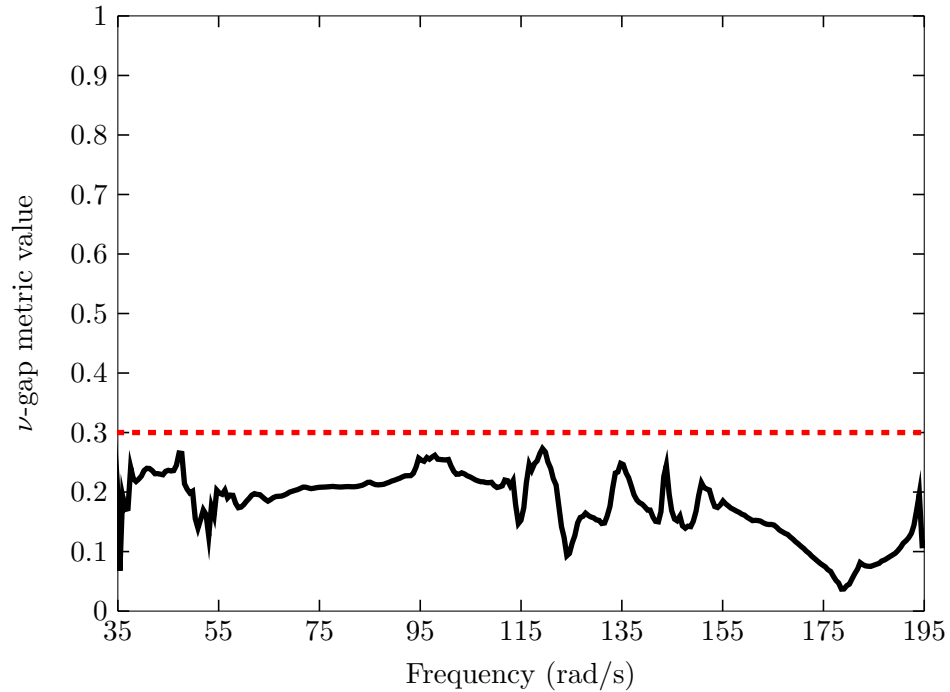
Figure 3.23: ν-gap metric distance between estimated model and experimental data across frequency. A ν-gap metric of 0.3 (━ ━ ━) means that the closed-loop input-output behavior is reproduced with good accuracy.

Updating

The modal vibration parameters obtained with the finite element model are compared to the experimental modal parameters identified from the ground vibration test. Here, it is observed that the two torsion modes, symmetric and anti-symmetric, do not match with the experimental results. Hence, parameter updating is required to obtain a more accurate finite element model that represents the BFF structure.

The model updating problem of the BFF finite element model is formulated as [2]

$$\min_{\alpha} \sum_{i=1}^{m} \left[1 - \mathrm{MAC}(\phi_{id,i}, \phi_{fe,i}(\alpha)) \right] + \|e_\omega(\alpha)\| \tag{3.29}$$

with

$$\mathrm{MAC}(\phi_{id,i}, \phi_{fe,i}) = \frac{|\phi_{id,i}^T \phi_{fe,i}|^2}{\phi_{id,i}^T \phi_{id,i} \phi_{fe,i}^T \phi_{fe,i}} - \tag{3.30}$$

$$e_\omega = \begin{bmatrix} \frac{\omega_{id,1} - \omega_{fe,1}}{\omega_{id,1}} & \cdots & \frac{\omega_{id,m} - \omega_{fe,m}}{\omega_{id,m}} \end{bmatrix}^T, \tag{3.31}$$

where $\omega_{id,i}$ and $\phi_{id,i}$ are the natural frequencies and mode shapes identified from the ground vibration test, $\omega_{fe,i}$ and $\phi_{fe,i}$ are the natural frequencies and modal shapes computed by the finite element model, m is the number of modes to match and α is the set of parameters to optimize in the finite element model. Here, the modal assurance criteria (MAC) can take values between 0 and 1, where 1 means the modal vectors are consistent and 0 means that the modal vectors are orthogonal.

The stiffness parameters EI_z, GJ_x and the mass parameters m, χ of the different BFF aircraft elements are optimized to minimize the error between the identified and modeled natural frequencies and mode shapes. These optimal parameters are obtained by running an evolutionary algorithm called differential evolution. Finally, the finite element model is updated with this set of optimal parameters and the comparison between the updated model and the experimental data is presented in Table 3.3.

As mentioned earlier, the updated finite element structural model can be used to create an aeroservoelastic (ASE) model of the BFF aircraft. However, the integration of this structural model with an aerodynamic model is still an ongoing research topic in the UAV laboratories. Hence, the ASE model developed by Lockheed Martin is presented in the next section.

Table 3.3: Natural frequencies and mode shapes comparison between updated finite element model and experimental data

| Modal Shape | Frequency (rad/s) | | MAC |
	Updated Model	Experiments	
1st Symmetric Bending	34.75	35.60	0.83
1st Anti-Symmetric Bending	53.91	52.61	0.92
1st Symmetric Torsion	120.70	115.27	0.84
1st Anti-Symmetric Torsion	124.91	124.56	0.93
2nd Symmetric Bending	144.70	145.59	0.93
2nd Anti-Symmetric Bending	173.04	179.70	0.92

3.3 Aeroservoelastic Model

This section presents the ASE model of the BFF aircraft developed by Lockheed Martin. The model was created using a structural model with 376 DOF and an unsteady aerodynamic model with 2252 DOF. Both of these models were generated in MSC/NASTRAN using finite elements and double lattice panels for the structural model and unsteady aerodynamic model, respectively [20]. From here, it is possible to obtain a set of generalized matrices that describe the structural and aerodynamic properties as described in Chapter 2. Next, linear, continuous-time, state-space ASE models in the form (2.20) are created [4].

The set of linear, continuous-time, state-space ASE models is created using the generalized mass matrix and generalized stiffness matrix provided by the structural model together with the generalized aerodynamic force matrix provided by the unsteady aerodynamic model. Because at a given Mach number the aerodynamic force matrix is a complex value matrix depending on the oscillation frequency, the matrix is approximated by the second order rational function in 2.9. With this, linear models are constructed by holding altitude constant and varying the airspeed of the aircraft. In total, 26 state-space models are obtained at constant altitude of 1000 ft from 40 to 90 KEAS (knots equivalent airspeed) with increments of 2 knots. In the remaining of the document, this set of models is referred as the LPV ASE model.

The LPV model has 148 states where the state vector consists of 37 generalized displacements with corresponding time derivatives and 74 unsteady aerodynamic states. The generalized displacements represent 5 rigid body modes corresponding to the lateral, plunge, roll, pitch and yaw modes of the aircraft, 8 flexible modes corresponding to symmetric and

anti-symmetric bending and torsion modes, and 24 secondary discrete DOF associated with local vibration modes in the structure. In addition, the 74 unsteady aerodynamic states produced by the rational function approximation correspond to two aerodynamic lags for each generalized displacement. With this approximation, the ASE model of the BFF aircraft is in the LPV state-space form given by (2.20).

Once the ASE model is in the LPV state-space form, a flutter analysis can be performed by evaluating the eigenvalues of the state matrix at each airspeed. Fig. 3.24 shows the evolution of six aeroelastic modal shapes across the flight envelope. Here, the frequency values and damping ratios at a particular airspeed are shown for this six vibration modes. In the ASE community, this plot is often called the V-f-g diagram of the aircraft. Notice that positive damping denotes system instabilities in this plot.
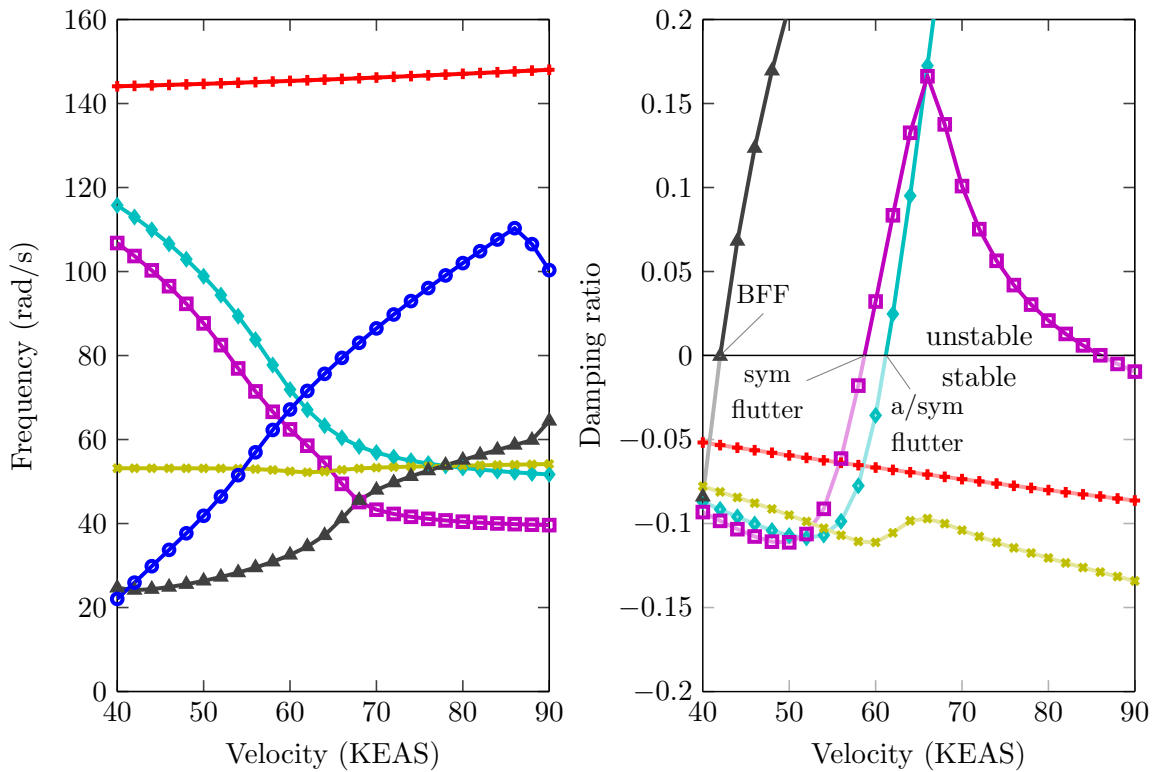
Figure 3.24: Velocity-frequency-damping (V-f-g) diagram of the BFF aircraft. Short period (—●—), 1st symmetric bending (—▲—), 1st anti-symmetric bending (—✕—), 1st symmetric torsion (—□—), 1st anti-symmetric torsion (—◆—), and 2nd symmetric bending (—+—).

Fig. 3.24 shows coupling of the short period mode with the first symmetric wing bending. This coupling produces the body flutter freedom phenomena at 42 KEAS with a frequency of

24.3 rad/s. Traditional flutter is also observed when the symmetric wing bending and symmetric wing torsion modes are coupled at a frequency of 65 rad/s. This phenomena occurs at an airspeed of 58 KEAS. Similarly, the anti-symmetric wing bending and anti-symmetric wing torsion modes come close in proximity at 61 KEAS with frequency of 69 rad/s. This leads to a third instability in the system. Hence, the flutter analysis performed concludes that the flight envelope of the vehicle is limited to 42 KEAS, airspeed at which the vehicle is marginally stable.

In addition, a frequency response of the vehicle for all flight conditions is plotted in Fig. 3.25. This plot shows the dependency on airspeed of the frequency response from the right outboard wing flap to the pitch rate sensor. Here, the lowest airspeed of 40 KEAS correspond to the dark blue curve, transitioning to green around 60 KEAS, and dark red at the highest velocities. Notice that the model dynamics change dramatically as a function of the airspeed. Looking at the phase plot, it is observed that the vehicle is marginally stable at 42 KEAS (dark blue) as inferred from the V-f-g diagram. Furthermore, a phase change is also observed around 60 KEAS (bright green) and 90 KEAS (dark red). The phase change corresponding to the bright green curves correspond to a change in stability of the system due to the traditional wing flutter phenomena. On the other hand, the dark red curve at 90 KEAS indicates that one of these wing modes is no longer unstable. This is also observed in the V-f-g diagram where the first symmetric torsion mode has a negative damping ratio. Recall that the ASE convention for stable systems is denoted by negative damping ratios.

3.4 Summary

This chapter described the aeroservoelastic experimental platform used in this dissertation to investigate the design of robust controllers. This research platform was developed by Lockheed Martin and is referred as the body freedom flutter (BFF) aircraft in the remaining chapters. The first part of the chapter presented a general description of the aircraft. Here, it was highlighted that the University of Minnesota was not provided with detailed information of the building process neither modeling process. Hence, a great effort has been put in understanding the modeling process of the BFF aircraft. These particular circumstances motivated the development of in-house structural and aerodynamic models.

The second part of the chapter focused on the development of a finite element model for the BFF aircraft. This model is intended to be integrated with an aerodynamic model in order to create an ASE model of the aircraft. However, this is still an ongoing research topic at the University of Minnesota and hence, the remaining chapters utilize an ASE
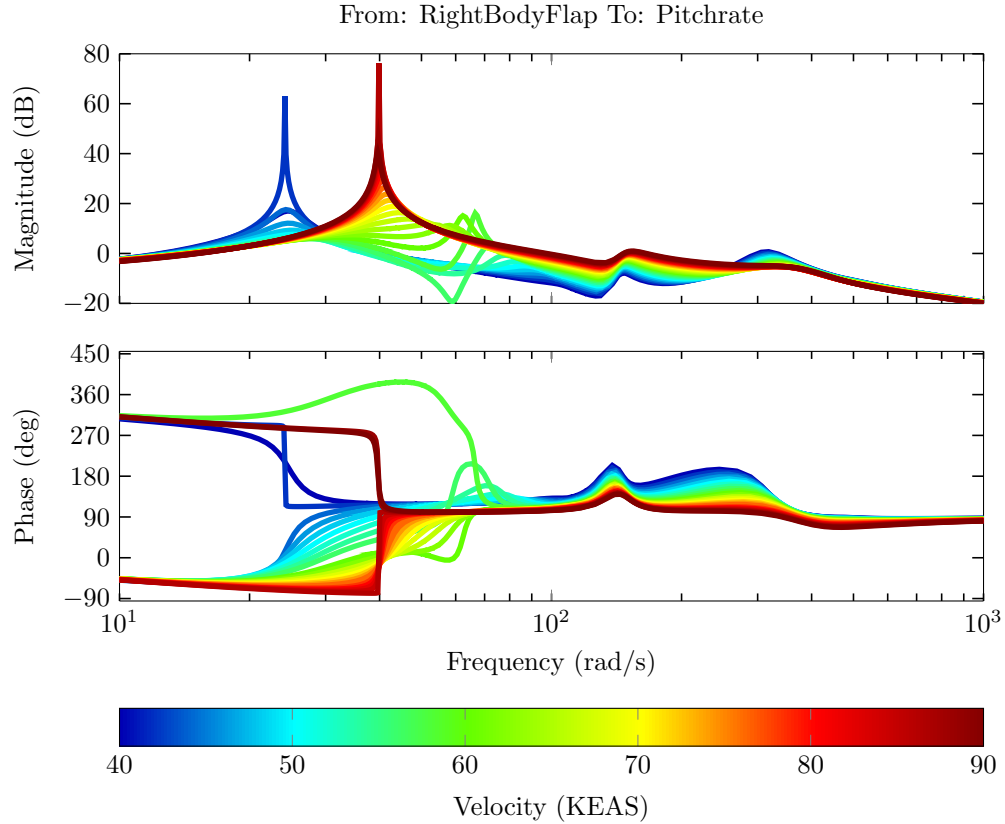
Figure 3.25: Frequency response of the BFF aircraft from the right outboard flap to the pitch rate sensor for all velocities (40-90 KEAS) in the flight envelope.

model created by Lockheed Martin. This ASE model is the focus of the last section of the chapter.

The ASE model of the BFF aircraft developed by Lockheed Martin consists on a set of linear, continuous-time, state-space models with varying airspeed. This model is represented by 148 states that are common across the flight envelope. This means that the ASE model is represented by an LPV system. Following, a description of the ASE dynamics together with a flutter analysis are presented. The results identified three flutter modes across the flight envelope, including the coupling of the short period mode and symmetric bending vibration (BFF) occurring at 42 KEAS. The objective of this research is to extend the flight envelope of the BFF aircraft by using the existing control surfaces for flutter suppression. However, the use of an LPV model with 148 states for control design is not practical; and hence a low-order LPV ASE model is required for control design. The next chapter will discuss this LPV model reduction topic in detail.

Chapter 4

Model Reduction for Aeroservoelastic Systems

This chapter presents a model reduction approach for LPV models of aeroservoelastic (ASE) systems. ASE models, as described in Chapter 2, usually result in LPV models with a large number of states. Using these high-order models for control design is unrealistic due to computational limitations associated with modern control synthesis techniques. Moreover, the controllers synthesized using these modern techniques result in equal or greater number of states as the plant. High-order controllers are hard to implement in practical applications and may even run into software or hardware problems. Hence, model order reduction of ASE systems is a necessary task previous to control design. The general model reduction problem is described in Section 4.1. Section 4.2 presents an overview of model reduction techniques for LPV systems. Finally, Section 4.3 describes the model reduction procedure for the body freedom flutter (BFF) vehicle.

4.1 Model Order Reduction

The model order reduction problem is in general stated as [57]: Given a full n-th order model $G_1(s)$ with m inputs and p outputs, find a lower r-th order model $G_2(s)$ with the same number of inputs, m, and outputs, p, such that the distance between G_1 and G_2 is small. Typically, the distance between G_1 and G_2 is measured by the $\mathcal{L}_\infty$-norm. $\mathcal{L}_\infty$ defines the set of all rational transfer matrices with no poles on the imaginary axis, and its norm is given by

$$\|G\|_\infty = \sup_{\omega \in \Re} \bar{\sigma} \left[G(j\omega) \right] \tag{4.1}$$

Using this $\mathcal{L}_\infty$-norm as a measure of approximation between G_1 and G_2, the model reduction problem is formulated as

$$\min_{deg(G_2) \le r} \|(G_1 - G_2)\|_\infty \tag{4.2}$$

For stable systems, i.e. the set of all rational functions with all poles in the left-half plane and no poles on the imaginary axis, the $\mathcal{L}_\infty$-norm is interpreted as the maximum achievable gain for sinusoidal inputs over all frequencies. As $t \to \infty$, let $e(\omega)$ denote the linear response of the system to a sinusoidal input $d(\omega)$, then $e(\omega) = G(j\omega)d(j\omega)$. At a given frequency ω, the gain $\|e(\omega)\|_2 / \|d(\omega)\|_2$ depends on the direction of $d(j\omega)$, and the gain in the worst-case direction is given by the maximum singular value

$$\bar{\sigma}\,[G(j\omega)] = \max_{d(\omega) \neq 0} \frac{\|e(\omega)\|_2}{\|d(\omega)\|_2} \tag{4.3}$$

Note that the model reduction problem in (4.2) can be interpreted as the induced gain from the input $v(t)$ to the matching error $e(t)$, shown in Fig. 4.1. Here, the full n-th order model G_1 is represented as the sum of the r-th lower order model G_2 and an uncertain system $\Delta_a = G_1 - G_2$. This type of uncertainty is often called additive uncertainty and the distance metric between models is defined by

$$\delta_n(G_1, G_2) := \|(G_1 - G_2)\|_\infty = \|\Delta_a\|_\infty \tag{4.4}$$
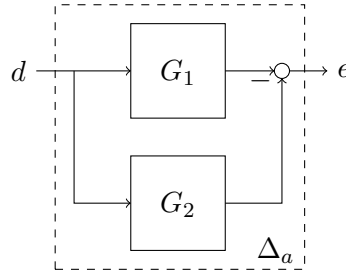
Figure 4.1: Model reduction problem: additive uncertainty

Alternatively, the distance between G_1 and G_2 can also be measured in the closed-loop feedback structure. In this context, the closed-loop behavior of the two systems is analyzed under the same feedback controller as shown in Fig. 4.2. A useful metric to compare G_1 and G_2 in this closed-loop structure is the ν-gap metric [56]. This metric is defined as

$$\delta_\nu(G_1, G_2) = \begin{cases} \|\Psi(G_1, G_1)\|_\infty & \text{if } \det(1 + G_2^* G_1)(j\omega) \neq 0 \;\; \forall \omega \in (-\infty, \infty) \text{ and} \\ & \text{wno } \det(1 + G_2^* G_1) - \eta(G_1) - \eta(G_2) = 0 \\ 1 & \text{otherwise} \end{cases} \tag{4.5}$$
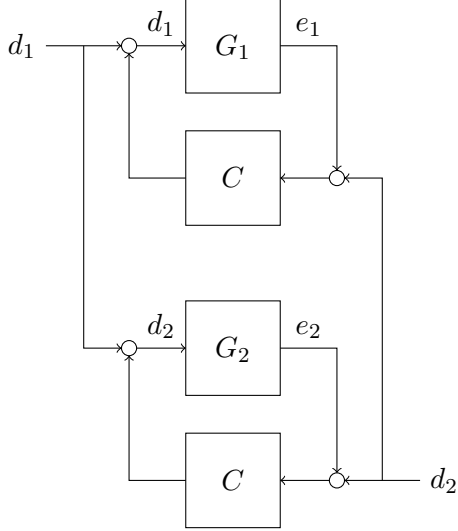
Figure 4.2: Closed-loop comparison

where $\eta(G)$ denotes the number of right-half plane poles of $G(s)$, $\mathrm{wno}(G) = \eta(G^{-1}) - \eta(G)$ and

$$\Psi(G_1, G_2) = (I + G_2 G_2^*)^{-1/2}(G_2 - G_1)(I + G_1^* G_1)^{-1/2} \qquad (4.6)$$

As indicated in (4.5), the ν-gap metric lies within the interval $[0, 1]$, where 0 is attained for two identical systems. Moreover, this metric exhibits important duality properties with stability margins. Any system G_1 at a distance less than β from the system G_2, i.e. $\delta_\nu(G_1, G_2) < \beta$, will be stabilized by any feedback controller stabilizing G_2 with a stability margin of at least β. Furthermore, any system G_1 at a distance greater than β from G_2 will be destabilized by the same feedback controller with a stability margin of at least β. These duality properties and the ability to compute the metric frequency by frequency will be of great benefit to analyze the distance between two systems in a robust manner [58].

Although the ν-gap metric is a great tool for measuring the difference between two systems in terms of closed-loop behavior, the model reduction problem using this approximation error is highly computational complex [59, 60]. On the other hand, the model reduction problem using the $\mathcal{L}_\infty$ approximation error, see (4.2), has been widely studied and successfully implemented for LTI systems. Moreover, several of these model reduction methods have been extended to deal with LPV systems [61–66]. In addition, this problem can be reformulated as a frequency weighted problem

$$\min_{deg(G_r) \leq r} \|W_o(s)(G - G_r)W_i(s)\|_\infty \qquad (4.7)$$

with appropriate choice of the input weighting matrix $W_i(s)$ and output weighting matrix $W_o(s)$ to weight the frequency range of interest. Frequency weighting is of particular interest for model reduction of ASE systems because control requirements at one frequency range can be drastically different from requirements at another frequency range.

In conclusion, model reduction techniques based on additive errors are easier to implement in ASE systems. However, a better measure to evaluate the approximation of full and reduced order models is provided by the $\nu-$gap metric. Hence, the model reduction approach proposed in this chapter focuses on techniques that minimize the distance $\delta_n(G_1, G_2)$ while evaluating the closeness between models with the ν-gap metric. The next section presents an overview of LPV model reduction techniques, following by their application to an ASE test vehicle.

4.2 Linear, Parameter-Varying Model Reduction

The objective of the LPV model reduction problem is to reduce the complexity of the models while preserving the state characteristics and input-output behavior for all parameters $\rho \in \mathcal{A}$. The main idea is to eliminate states with small energy contribution transferred from inputs to outputs.

This section describes four LPV methods used to address the model reduction problem of ASE systems. These methods are: (1) truncation, (2) residualization, (3) modal truncation, and (4) balanced residualization. The methods are described using a partitioned n-th state-space realization of (2.20) such that

$$
\begin{aligned}
\dot{x}_1 &= A_{11}(\rho)x_1 + A_{12}(\rho)x_2 + B_1(\rho)d \\
\dot{x}_2 &= A_{21}(\rho)x_1 + A_{22}(\rho)x_2 + B_2(\rho)d \\
e &= C_1(\rho)x_1 + C_2(\rho)x_2 + D(\rho)d
\end{aligned}
\tag{4.8}
$$

where x_1 is a vector of r states to preserve and x_2 contains the $n - r$ states to remove. This notation is used to describe the different model reduction techniques presented in the following subsections.

4.2.1 Truncation

Model reduction by truncation consists of eliminating the states and dynamics associated with the vector x_2. The truncated model $\bar{G}_\rho$ is then [67]

$$
\begin{aligned}
\dot{x}_1 &= A_{11}(\rho)x_1 + B_1(\rho)d \\
e &= C_1(\rho)x_1 + D(\rho)d
\end{aligned}
\tag{4.9}
$$

In general, very little can be said about the relationship between the transfer function matrices G_ρ and $\bar{G}_\rho$. Particularly, the truncated system may be unstable even if the full-order system is stable; or the truncated system realization may be non-minimal even if the full-order realization is minimal [68]. However, the truncation error can be analyzed for special cases.

Let $G_\kappa(s)$ be the transfer function of a linear time-invariant system for a fixed parameter $\rho = \kappa$

$$G_\kappa(s) = D(\kappa) + C(\kappa) \left[sI - A(\kappa)\right]^{-1} B(\kappa) \tag{4.10}$$

with $A(\kappa)$ nonsingular, then

$$G_\kappa(\infty) = \bar{G}_\kappa(\infty) = D(\kappa) \tag{4.11}$$

This means that all reduced models obtained by truncation have perfect matching at infinite frequency. Hence, truncation is preferred when accuracy of the reduced order model at high frequencies is required.

On the other hand, the truncation error at low frequencies is given by

$$G_\kappa(0) - \bar{G}_\kappa(0) = C_1(\kappa)A_{11}^{-1}(\kappa)B_1(\kappa) - C(\kappa)A^{-1}(\kappa)B(\kappa) \tag{4.12}$$

This difference can be unacceptably large for applications requiring good low-frequency models. In these cases, truncation is not the appropriate model reduction method. In contrast, the following subsection describes a model reduction method that greatly improves the model reduction errors at low frequencies.

4.2.2 Residualization

Model reduction by residualization approximates the low-frequency behavior by setting $\dot{x}_2 = 0$, where the vector x_2 represents the fast dynamics of the system [67]. This gives the quasi-steady solution for x_2

$$\begin{aligned} 0 &= A_{21}(\rho)x_1 + A_{22}(\rho)x_2 + B_2(\rho)d \\ x_2 &= -A_{22}^{-1}(\rho)\left[A_{21}(\rho)x_1 + B_2(\rho)d\right] \end{aligned} \tag{4.13}$$

where $A_{22}(\rho)$ is nonsingular. Eliminating x_2 from the remaining equations in (4.8) using (4.13) yields the residualized model G_r

$$\begin{aligned} \dot{x}_1 &= \bar{A}_{11}(\rho)x_1 + \bar{B}_1(\rho)d \\ e &= \bar{C}_1(\rho)x_1 + \bar{D}(\rho)d \end{aligned} \tag{4.14}$$

46

where

$$\bar{A}_{11}(\rho) = A_{11}(\rho) - A_{12}(\rho)A_{22}(\rho)^{-1}A_{21}(\rho), \quad \bar{B}_1(\rho) = B_1(\rho) - A_{12}(\rho)A_{22}(\rho)^{-1}B_2(\rho)$$
$$\bar{C}_1(\rho) = C_1(\rho) - C_2(\rho)A_{22}(\rho)^{-1}A_{21}(\rho), \quad \bar{D}(\rho) = D(\rho) - C_2(\rho)A_{22}(\rho)^{-1}B_2(\rho)$$

Notice that $A(\rho)$ can be written as

$$A(\rho) = \begin{bmatrix} I & A_{12}(\rho)A_{22}^{-1}(\rho) \\ 0 & I \end{bmatrix} \begin{bmatrix} \bar{A}_{11}(\rho) & 0 \\ 0 & A_{22}(\rho) \end{bmatrix} \begin{bmatrix} I & 0 \\ A_{22}^{-1}(\rho)A_{21}(\rho) & I \end{bmatrix} \qquad (4.15)$$

which gives

$$A^{-1}(\rho) = \begin{bmatrix} I & 0 \\ -A_{22}^{-1}(\rho)A_{21}(\rho) & I \end{bmatrix} \begin{bmatrix} \bar{A}_{11}^{-1}(\rho) & 0 \\ 0 & A_{22}^{-1}(\rho) \end{bmatrix} \begin{bmatrix} I & -A_{12}(\rho)A_{22}^{-1}(\rho) \\ 0 & I \end{bmatrix} \qquad (4.16)$$

Equation (4.16) is used to obtain $G_\kappa(0)$ for a fixed parameter $\rho = \kappa$ as

$$G_\kappa(0) = D(\kappa) \begin{bmatrix} \bar{C}_1(\kappa) & C_2(\kappa) \end{bmatrix} \begin{bmatrix} \bar{A}_{11}^{-1}(\kappa) & 0 \\ 0 & A_{22}^{-1}(\kappa) \end{bmatrix} \begin{bmatrix} \bar{B}_1(\kappa) \\ B_2(\kappa) \end{bmatrix} \qquad (4.17)$$

which is equivalent to

$$G_\kappa(0) = \bar{G}_\kappa(0) = \bar{D}(\kappa) - \bar{C}_1(\kappa)\bar{A}_{11}^{-1}(\kappa)\bar{B}_1(\kappa) \qquad (4.18)$$

This means that residualization retains the accuracy of the reduced order model at low-frequency. Consequently, the residualization technique is related to the direct truncation technique by the bilinear transform $s \longrightarrow 1/s$ [69].

As seen, truncation and residualization methods require a state-space realization of the system. However, the dynamics of a system can be represented by many state-space models and, in principle, truncation and residualization techniques can be applied to all of them. Hence, an important task in model order reduction is to select the appropriate state-space realization for which truncation or residualization bounded errors are guaranteed. Examples of these realizations are the modal and balanced state-space realizations.

Modal and balanced state-space realizations are commonly used in engineering practice due to their particular structure and control properties. These realizations are usually obtained by choosing alternative state coordinates to describe the dynamics of the system. The relation between a new set of state coordinates and the original set of state coordinates is called a similarity transformation. The main advantage of using similarity transformations is that the dynamic characteristics of the system are not affected by this coordinate change in the state-space.

Particularly, LPV state-space systems in the form (2.20) are transformed into another set of equations if there exists a differentiable transformation, $T(\rho)$, such that $\hat{x} = T(\rho)x$ and

$$\dot{\hat{x}} = \left[T(\rho)A(\rho) + \frac{\partial T}{\partial \rho}\dot{\rho}\right]T^{-1}(\rho)\hat{x} + T(\rho)B(\rho)d$$
$$e = C(\rho)T^{-1}(\rho)\hat{x} + D(\rho)d$$

(4.19)

Using these parameter-dependent transformations introduces an explicit dependence on the parameter variation, $\dot{\rho}$, into the state-space realization (4.19). These variations increase the complexity of the LPV model, making the model reduction problem computational challenging. Hence, a time invariant transformation, T, that generates an LPV realization with consistent states for all the feasible parameters, ρ, is used for model reduction purposes. The desired LPV state-space transformation is then

$$\dot{\hat{x}} = TA(\rho)T^{-1}\hat{x} + TB(\rho)d$$
$$e = C(\rho)T^{-1}\hat{x} + D(\rho)d$$

(4.20)

The following subsections present the details of the modal and balanced state-space realizations and their model reduction techniques for LPV models. The objective is to obtain a time invariant similarity transformation, T, that transforms the LPV model in a modal and balanced state-space realization. Truncation is the technique chosen to reduce the LPV modal realization and residualization is chosen to reduce the LPV balanced realization.

4.2.3 Modal Truncation

For a fixed value of the parameter, $\rho = \kappa$, there exist a state transformation matrix T such that the transformed state matrix $\hat{A}(\kappa) = TA(\kappa)T^{-1}$ is in the diagonal form [63, 67]

$$\hat{A}(\kappa) = \begin{bmatrix} \lambda_1(\kappa) & & & \\ & \lambda_2(\kappa) & & \\ & & \ddots & \\ & & & \lambda_n(\kappa) \end{bmatrix}$$

(4.21)

and the transformed matrices $\hat{B}(\kappa) = TB(\kappa)$ and $\hat{C}(\kappa) = C(\kappa)T^{-1}$ are partioned as

$$\hat{B}(\kappa) = \begin{bmatrix} \hat{B}_1(\kappa) \\ \hat{B}_2(\kappa) \\ \vdots \\ \hat{B}_n(\kappa) \end{bmatrix}, \quad \hat{C}(\kappa) = \begin{bmatrix} \hat{C}_1(\kappa) & \bar{C}_2(\kappa) & \cdots & \hat{C}_n(\kappa) \end{bmatrix}$$

(4.22)

The similarity transformation that induces the diagonal structure in (4.21) is built around the eigenvectors of $A(\kappa)$. Let $\lambda_i(\kappa)$ be the i-th eigenvalue of $A(\kappa)$ and $v(\kappa)$ the associated eigenvector, then the transformation T is

$$T^{-1} = \begin{bmatrix} v_1(\kappa) & v_2(\kappa) & \cdots & v_n(\kappa) \end{bmatrix} \qquad (4.23)$$

Such transformation brings the system to what are known as modal coordinates, where $\lambda_i(\kappa)$ is the corresponding modal frequency and $v_i(\kappa)$ is the corresponding modal shape. Then, this modal realization will retain only the modes in the frequency range of interest.

Partitioning the state matrix, $\hat{A}(\kappa) = \mathrm{diag}\left(\hat{A}_r(\kappa), \hat{A}_{n-r}(\kappa)\right)$, where $\hat{A}_r(\kappa)$ contains the r modes to retain and $\hat{A}_{n-r}(\kappa)$ the modes to remove, gives the reduced model $\hat{G}_r$

$$\begin{aligned} \dot{\hat{x}}_r &= \hat{A}_r(\kappa)\hat{x}_r + \hat{B}_r(\kappa)d \\ e &= \hat{C}_r(\kappa)\hat{x}_r + D(\kappa)d \end{aligned} \qquad (4.24)$$

where $\hat{x}_r$ is the modal vector of r states to preserve. Here the truncation error between the original modal realization $\hat{G}$ and reduced model $\hat{G}_r$ is given by

$$\hat{G}(s) - \hat{G}_r(s) = \sum_{i=r+1}^{n} \frac{C(\kappa)_i B_i(\kappa)}{s - \lambda_i} \qquad (4.25)$$

and therefore

$$\left\| \hat{G}(s) - \hat{G}_r(s) \right\|_{\infty} = \sum_{i=r+1}^{n} \frac{\bar{\sigma}\left[C(\kappa)_i B_i(\kappa)\right]}{|\mathrm{Re}(\lambda_i)|} \qquad (4.26)$$

An advantage of modal truncation is that the poles of the truncated model are a subset of the poles of the original model and therefore retain any physical interpretation they might have, e.g. the phugoid mode in aircraft dynamics [67]. However, the physical insight gained from decoupling the LTI differential equations is lost when extended to LPV systems. Using a parameter-varying transformation $T(\rho)$, as in (4.19), introduces derivative terms that can generate large off-diagonal elements into the transformed state matrix. Hence, a constant transformation T that yields the modal form at a fixed point $\rho = \kappa$ is used to approximate a modal state-space basis of the LPV system. Here, modal couplings at the other parameters $\rho \neq \kappa$ are neglected while removing modes from the LPV system that are outside the frequency range of interest.

4.2.4 Balanced Residualization

Balanced realizations are based on the measure of the controllability and observability of the system. For an LPV system [65], these measures are given by the controllability and

observability Gramians defined as

$$P > \int_0^\infty e^{A(\rho)t} B(\rho) B^T(\rho) e^{A^T(\rho)t} dt \tag{4.27}$$

$$Q > \int_0^\infty e^{A^T(\rho)t} C^T(\rho) C(\rho) e^{A(\rho)t} dt \tag{4.28}$$

Solutions to these integrals are also the solutions to the Lyapunov inequalities [57]

$$A(\rho)P + PA^T(\rho) + B(\rho)B^T(\rho) < 0 \tag{4.29}$$

$$A^T Q(\rho) + QA(\rho) + C^T(\rho)C(\rho) < 0 \tag{4.30}$$

if and only if $P = P^T > 0$ and $Q = Q^T > 0$.

Note that the integrals given by Eq. (4.27) and Eq. (4.28) will be unbounded if the matrix $A(\rho)$ is not stable (i.e. there exist at least one eigenvalue on the imaginary axis or the right-half plane). Unfortunately, ASE systems are naturally mixed stability systems and this standard balanced reduction approach is not suitable. An alternative to computing controllability and observability Gramians for unstable systems is to use coprime factorizations [65,66]. The objective is to find the reduced balanced coprime factors of the unstable system and use these to construct the LPV reduced order model. A detailed description of this approach is provided next.

Coprime Factorization Approach

If G_ρ is an LPV realization of the form (2.20), there is a contractive right-coprime factorization $G_\rho = N_\rho M_\rho^{-1}$ such that the set of all stable input-output pairs is given by

$$\begin{bmatrix} e \\ d \end{bmatrix} = \begin{bmatrix} N_\rho \\ M_\rho \end{bmatrix} q \tag{4.31}$$

where q is square integrable over the infinite time axis [64, 65]. A realization for this contractive right-coprime factorization is defined as

$$\begin{bmatrix} \dot{x} \\ e \\ d \end{bmatrix} = \begin{bmatrix} A(\rho) + B(\rho)F(\rho) & B(\rho)S^{-1/2}(\rho) \\ C(\rho) + D(\rho)F(\rho) & D(\rho)S^{-1/2}(\rho) \\ F(\rho) & S^{-1/2}(\rho) \end{bmatrix} \begin{bmatrix} x \\ q \end{bmatrix} \tag{4.32}$$

where

$$S(\rho) = I + D^T(\rho)D(\rho),$$
$$F(\rho) = -S(\rho)^{-1} \left[B^T(\rho)X + D^T(\rho)C(\rho) \right]$$

and $X = X^T > 0$ is a constant solution of the Generalized Control Ricatti Inequality (GCRI)

$$\left[A(\rho) - B(\rho)S^{-1}(\rho)D^T(\rho)C(\rho)\right]^T X + X\left[A(\rho) - B(\rho)S^{-1}(\rho)D^T(\rho)C(\rho)\right] -$$
$$XB(\rho)S^{-1}(\rho)B^T(\rho)X + C^T(\rho)R^{-1}(\rho)C(\rho) < 0 \quad (4.33)$$

with $R(\rho) = I + D(\rho)D^T(\rho)$.

The controllability Gramian P and observability Gramian Q of the contractive right-coprime factorization are given by

$$\begin{aligned} Q &= X \\ P &= (I + YX)^{-1}Y \end{aligned} \quad (4.34)$$

where X solves the GCRI and $Y = Y^T > 0$ solves the Generalized Filtering Ricatti Inequality (GFRI)

$$\left[A(\rho) - B(\rho)D^T(\rho)R^{-1}(\rho)C(\rho)\right]Y + Y\left[A(\rho) - B(\rho)D^T(\rho)R^{-1}(\rho)C(\rho)\right]^T -$$
$$YC^T(\rho)R^{-1}(\rho)C(\rho)Y + B(\rho)S^{-1}(\rho)B^T(\rho) < 0 \quad (4.35)$$

Note that linear matrix inequalities (LMIs) can be obtained from the Schur complement of (4.33) and (4.35) with change of variables $\bar{X} = X^{-1}$, $\bar{Y} = Y^{-1}$. Then the solutions for these Riccati inequalities are given by [66]

$$\begin{bmatrix} \bar{X}A_C^T(\rho) + A_C(\rho)\bar{X} - B(\rho)S^{-1}(\rho)B^T(\rho) & \bar{X}C^T(\rho) \\ C(\rho)\bar{X} & -R(\rho) \end{bmatrix} < 0 \quad (4.36)$$

$$\begin{bmatrix} \bar{Y}A_F(\rho) + A_F^T(\rho)\bar{Y} - C^T(\rho)R^{-1}(\rho)C(\rho) & \bar{Y}B(\rho) \\ B^T(\rho)\bar{Y} & -S(\rho) \end{bmatrix} < 0 \quad (4.37)$$

with

$$\begin{aligned} A_C(\rho) &= A(\rho) - B(\rho)S^{-1}(\rho)D^T(\rho)C(\rho), \\ A_F(\rho) &= A(\rho) - B(\rho)D^T(\rho)R^{-1}(\rho)C(\rho) \end{aligned}$$

A balanced realization of the system is then a realization with equal, diagonal controllability and observability Gramians, $\hat{P} = \hat{Q} = \Sigma$. Here, Σ is denoted as the Hankel singular values matrix. The constant balancing state transformation, T, is chosen such that $\hat{P} = TPT^T$ and $\hat{Q} = (T^{-1})^T QT^{-1}$. These expressions can be rewritten as

$$PT^T = J\Sigma, \qquad\qquad QJ = T^T\Sigma, \qquad\qquad J = T^{-1} \qquad (4.38)$$

where J, T and Σ are unknown matrices.

One method to solve (4.38) is to use the singular value decomposition of the symmetric positive Gramians P and Q [70, 71]. Given $P = P^T > 0$ and $Q = Q^T > 0$, the following holds

$$P = U_p \Sigma_p U_p^T = L_p L_p^T$$
$$Q = U_q \Sigma_q U_q^T = L_q L_q^T$$

(4.39)

where $L_p = U_p \Sigma_p^{-1/2}$ and $L_q = U_q \Sigma_q^{-1/2}$. Substituting (4.39) in (4.38) yields

$$L_p L_p^T T^T = S\Sigma, \qquad\qquad L_q L_q^T J = T^T \Sigma, \qquad\qquad J = T^{-1} \qquad (4.40)$$

Then the solution for S and Σ follows from the eigenvalue problem

$$L_p(L_p^T L_q)L_q^T J = S\Sigma^2$$
$$L_p(U_e \Sigma_e V_e^T)L_q^T = J\Sigma^2 J^{-1}$$

(4.41)

where $L_p^T L_q = U_e \Sigma_e V_e^T$ and

$$S = L_p U_e \Sigma_e^{-1/2}$$
$$T = (L_q V_e \Sigma_e^{-1/2})^T$$
$$\Sigma = \Sigma_e$$

(4.42)

Note also that $\hat{P}\hat{Q} = TPQT^{-1} = \Sigma^2$, and therefore the eigenvalues of the product of the Gramians are invariant under transformation [57].

Using the balanced transformation T in (4.42), the balanced parameter varying right-coprime factorization of G_ρ is

$$\begin{bmatrix} \dot{\hat{x}} \\ e \\ d \end{bmatrix} = \begin{bmatrix} \hat{A}(\rho) + \hat{B}(\rho)\hat{F}(\rho) & \hat{B}(\rho)S^{-1/2}(\rho) \\ \hat{C}(\rho) + D(\rho)\hat{F}(\rho) & D(\rho)S^{-1/2}(\rho) \\ \hat{F}(\rho) & S^{-1/2}(\rho) \end{bmatrix} \begin{bmatrix} \hat{x} \\ q \end{bmatrix}$$

(4.43)

where q represents the set of all stable input signals and

$$\hat{A}(\rho) = T^{-1}A(\rho)T$$
$$\hat{B}(\rho) = T^{-1}B(\rho)$$
$$\hat{C}(\rho) = C(\rho)T$$
$$\hat{F}(\rho) = -S^{-1}(\rho)\left[\hat{B}^T(\rho)\Sigma + D^T(\rho)\hat{C}(\rho)\right]$$

This realization reflects the combined controllability and observability of the individual states. Partitioning the system in Eq. (4.43) such that $\Sigma = \mathrm{diag}(\Sigma_1, \Sigma_2)$, the balanced right-coprime factor is

$$
\begin{bmatrix} \dot{\hat{x}}_1 \\ \dot{\hat{x}}_2 \\ e \\ d \end{bmatrix} = \begin{bmatrix} \hat{A}_{11}(\rho) + \hat{B}_1(\rho)\hat{F}_1(\rho) & \hat{A}_{12}(\rho) + \hat{B}_1(\rho)\hat{F}_2(\rho) & \hat{B}_1(\rho)S^{-1/2}(\rho) \\ \hat{A}_{21}(\rho) + \hat{B}_2(\rho)\hat{F}_1(\rho) & \hat{A}_{22}(\rho) + \hat{B}_2(\rho)\hat{F}_2(\rho) & \hat{B}_2(\rho)S^{-1/2}(\rho) \\ \hat{C}_1(\rho) + D(\rho)\hat{F}_1(\rho) & \hat{C}_2(\rho) + D(\rho)\hat{F}_2(\rho) & D(\rho)S^{-1/2}(\rho) \\ \hat{F}_1(\rho) & \hat{F}_2(\rho) & S^{-1/2}(\rho) \end{bmatrix} \begin{bmatrix} \hat{x}_1 \\ \hat{x}_2 \\ q \end{bmatrix}
$$
(4.44)

with

$$
\begin{array}{llll}
\hat{A}_{11}(\rho) \in \mathbb{R}^{r \times r}, & \hat{A}_{12}(\rho) \in \mathbb{R}^{r \times (n-r)}, & \hat{B}_1(\rho) \in \mathbb{R}^{r \times m}, & \hat{C}_1(\rho) \in \mathbb{R}^{p \times r}, \\
\hat{A}_{21}(\rho) \in \mathbb{R}^{(n-r) \times r}, & \hat{A}_{22}(\rho) \in \mathbb{R}^{(n-r) \times (n-r)}, & \hat{B}_2(\rho) \in \mathbb{R}^{(n-r) \times m}, & \hat{C}_2(\rho) \in \mathbb{R}^{p \times (n-r)}, \\
\hat{F}_1(\rho) \in \mathbb{R}^{m \times r}, & \hat{F}_2(\rho) \in \mathbb{R}^{m \times (n-r)}, & D(\rho) \in \mathbb{R}^{p \times m}, & S(\rho) \in \mathbb{R}^{m \times m}.
\end{array}
$$

Here, Σ_1 is related to the most controllable and observable states and Σ_2 is related to the least controllable and observable directions. The small Hankel singular values in Σ_2 indicate that a finite amount of energy in a given input do not result in significant energy in the output. Eliminating these states will not affect the input/output characteristics of the system. Hence, the reduced right-coprime factor obtained by residualizing the states related to Σ_2 is [66]

$$
\begin{bmatrix} \dot{\hat{x}}_r \\ e \\ d \end{bmatrix} = \begin{bmatrix} A_s(\rho) & B_s(\rho) \\ C_{ns}(\rho) & D_{ns}(\rho) \\ C_{ms}(\rho) & D_{ms}(\rho) \end{bmatrix} \begin{bmatrix} \hat{x}_r \\ q \end{bmatrix}
$$
(4.45)

where

$$
\begin{aligned}
A_s(\rho) =& \hat{A}_{11}(\rho) + \hat{B}_1(\rho)\hat{F}_1(\rho) - \\
& \left[\hat{A}_{12}(\rho) + \hat{B}_1(\rho)\hat{F}_2(\rho) \right] \left[\hat{A}_{22}(\rho) + \hat{B}_2(\rho)\hat{F}_2(\rho) \right]^{-1} \left[\hat{A}_{21}(\rho) + \hat{B}_2(\rho)\hat{F}_1(\rho) \right], \\
B_s(\rho) =& \hat{B}_1(\rho)S^{-1/2}(\rho) - \\
& \left[\hat{A}_{12}(\rho) + \hat{B}_1(\rho)\hat{F}_2(\rho) \right] \left[\hat{A}_{22}(\rho) + \hat{B}_2(\rho)\hat{F}_2(\rho) \right]^{-1} \left[\hat{B}_2(\rho)S^{-1/2}(\rho) \right], \\
C_{ns}(\rho) =& \hat{C}_1(\rho) + D(\rho)\hat{F}_1(\rho) - \\
& \left[\hat{C}_2(\rho) + D(\rho)\hat{F}_2(\rho) \right] \left[\hat{A}_{22}(\rho) + \hat{B}_2(\rho)\hat{F}_2(\rho) \right]^{-1} \left[\hat{A}_{21}(\rho) + \hat{B}_2(\rho)\hat{F}_1(\rho) \right], \\
C_{ms}(\rho) =& \hat{F}_1(\rho) - \hat{F}_2 \left[\hat{A}_{22}(\rho) + \hat{B}_2(\rho)\hat{F}_2(\rho) \right]^{-1} \left[\hat{A}_{21}(\rho) + \hat{B}_2(\rho)\hat{F}_1(\rho) \right],
\end{aligned}
$$

$$D_{ns}(\rho) = D(\rho)S^{-1/2}(\rho) - \left[\hat{C}_2(\rho) + D(\rho)\hat{F}_2(\rho)\right]\left[\hat{A}_{22}(\rho) + \hat{B}_2(\rho)\hat{F}_2(\rho)\right]^{-1}\hat{B}_2(\rho)S^{-1/2}(\rho),$$

$$D_{ms}(\rho) = S^{-1/2}(\rho) - \hat{F}_2(\rho)\left[\hat{A}_{22}(\rho) + \hat{B}_2(\rho)\hat{F}_2(\rho)\right]^{-1}\hat{B}_2(\rho)S^{-1/2}(\rho)$$

assuming $\left[\hat{A}_{22}(\rho) + \hat{B}_2(\rho)\hat{F}_2(\rho)\right]$ invertible $\forall \rho \in \mathcal{A}$.

Finally, the reduced r-th model $\hat{G}_{\rho_r} = \hat{N}_{\rho_r}\hat{M}_{\rho_r}^{-1}$ is given by

$$\begin{bmatrix} \dot{\hat{x}}_r \\ e \end{bmatrix} = \begin{bmatrix} A_s(\rho) - B_s(\rho)D_{ms}^{-1}(\rho)C_{ms}(\rho) & B_s(\rho)D_{ms}^{-1}(\rho) \\ C_{ns}(\rho) - D_{ns}(\rho)D_{ms}^{-1}(\rho)C_{ms}(\rho) & D_{ns}(\rho)D_{ms}^{-1}(\rho) \end{bmatrix} \begin{bmatrix} \hat{x}_r \\ d \end{bmatrix} \tag{4.46}$$

This coprime factorization approach is used for balanced reduction of LPV ASE models. The following section presents a procedure to obtain a reduced LPV model for the BFF test vehicle.

4.3 Model Reduction of Body Freedom Flutter Vehicle

This section presents a procedure to obtain an LPV reduced order model of the BFF vehicle that preserves the state meaning at all flight conditions. As described in Chapter 3, the LPV model of the aircraft consists of 148 states, 8 inputs and 11 outputs. Fig. 3.24 and Fig. 3.25 show that the modes participating in the flutter phenomena vary between 10-160 rad/s across the flight envelope. Consequently, the frequency range of interest for the BFF model reduction is defined to be 10-160 rad/s.

The four LPV model reduction techniques described in Section 4.2 are applied sequentially to the BFF vehicle. Elimination of states is based on the ν-gap metric, preservation of unstable dynamics, and input/output frequency responses between the full order model and the reduced order model. The approach starts by truncating states directly related to very low-frequency modes of the aircraft. Next, the LPV system is transformed to a quasi-modal form in order to remove high-frequency modes outside the bandwidth of interest. Here, quasi-modal means that the time-invariant transformation does not decouple the LPV system at all flight conditions. A third step in the model reduction approach is to residualize the remaining states related to multiple modes. Finally, the LPV system is balanced based on its coprime factors and the states with the smallest Hankel singular values are residualized.

In addition, a LTI model reduction of the BFF is performed by treating the models at individual flight conditions as LTI systems. In this case, a similarity transformation is computed for each LTI model meaning that the state consistency of the system is lost across the flight envelope. The objective is to set a lower bound for the BFF model reduction

problem by comparing the results between the LTI and LPV procedures. The following subsections present the details of both procedures.

4.3.1 Truncation

The goal of the model reduction by truncation is to match the response of the system at infinite frequency. Low-frequency modes outside the bandwidth of interest can be truncated from the model giving preference to high-frequency accuracy. The BFF plunge displacement and roll angle modes, corresponding to the second and third states respectively, have a frequency approximately four orders of magnitude below the bandwidth of interest at all flight conditions. Hence, these extremely slow modes are truncated to obtain a LPV reduced order model with 146 states.

Figure 4.3 shows a comparison of the frequency responses between the full order model with 148 states and the truncated model with 146 states. The bode plots corresponding to the transfer functions from the left body flap deflection to the pitch rate measurement and the right outboard flap deflection to the left forward wing accelerometer are plotted for the flight conditions at 42 and 72 KEAS. Here, the highlighted area denotes the frequency bandwidth of interest for the model reduction problem. The plots show that the two states around 10^{-3} rad/s are successfully truncated without affecting the input/output relationship at higher frequencies.

Figure 4.4 plots the frequency dependency of the ν-gap metric between the full order model and the truncated model for all flight conditions. Notice that the errors across frequency and airspeed is of order 10^{-7}. Hence, the elimination of plunge displacement and roll angle does not affect the closed-loop response of the system in the ν-gap metric sense.

Figure 4.5 shows the full order model pole migration in the complex plane and compares it with the pole migration of the truncated model. The plot shows the trajectory of poles and their transition from stable to unstable with respect to airspeed. Blue color poles correspond to low velocities and red color poles to the highest speeds in the flight envelope. Notice that the aircraft is stable at 40 KEAS (i.e., all dark blue poles are in the left-hand plane) with three complex pairs close to the imaginary axis. These complex poles migrate to the right-half plane and it is observed that the aircraft becomes highly unstable at the fastest velocities. Comparing the pole migration for the full order model and truncated model, it is observed that truncation of the rigid body states preserves the unstable dynamics of the system perfectly. Hence, the truncated LPV model with 146 states is accepted as a good approximation of the LPV full order model. The next step is to eliminate the high-frequency
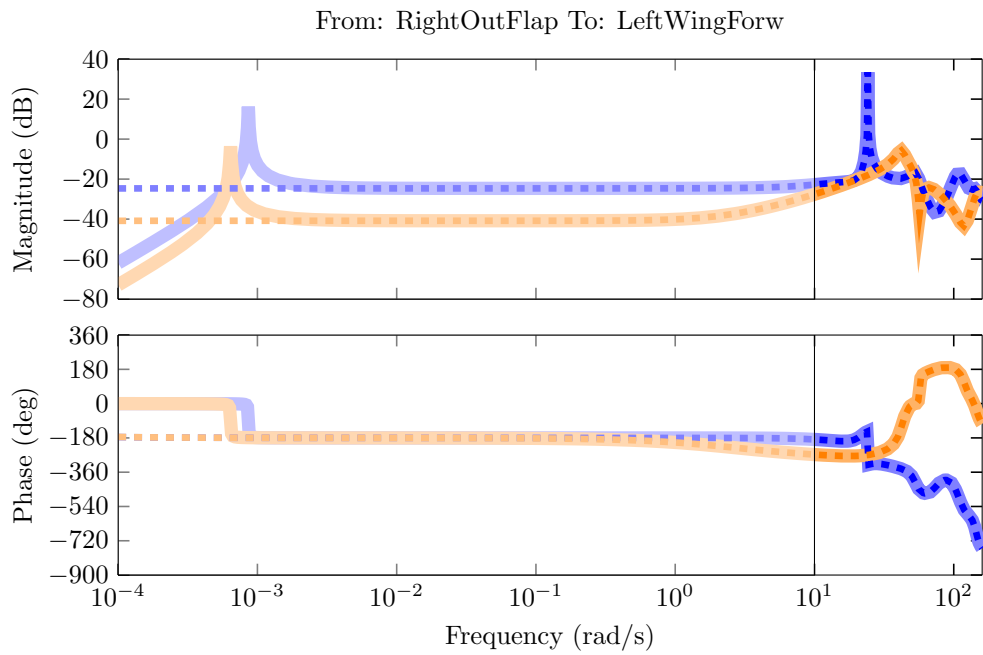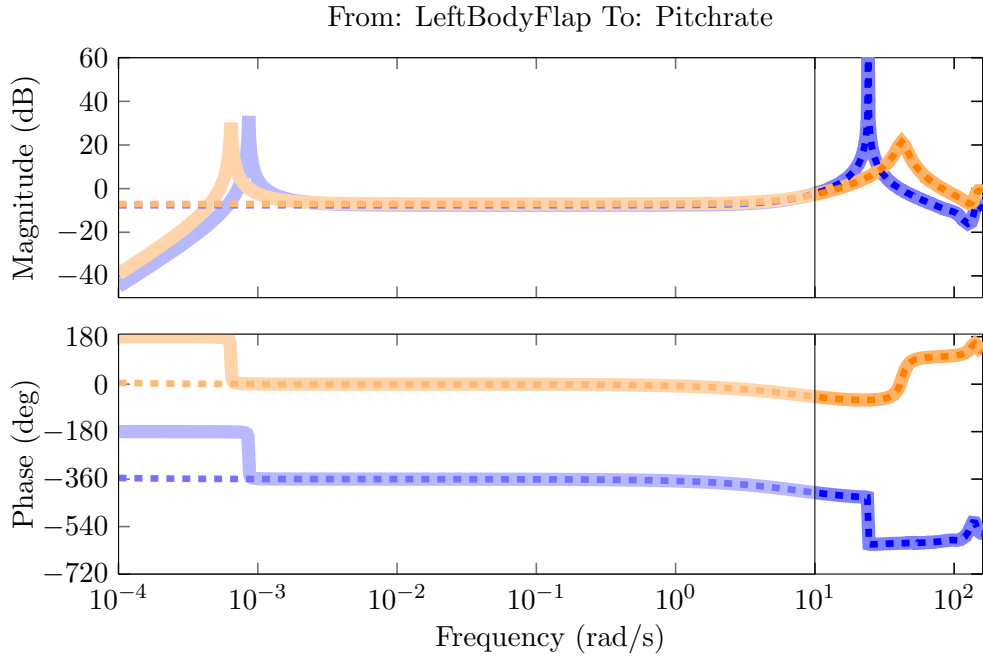
Figure 4.3: Bode plots of full order model (148 states) at 42 KEAS ( ) and 72 KEAS ( ) compared to truncated model with 146 states (/). Lighter areas denote frequency range of no interest.
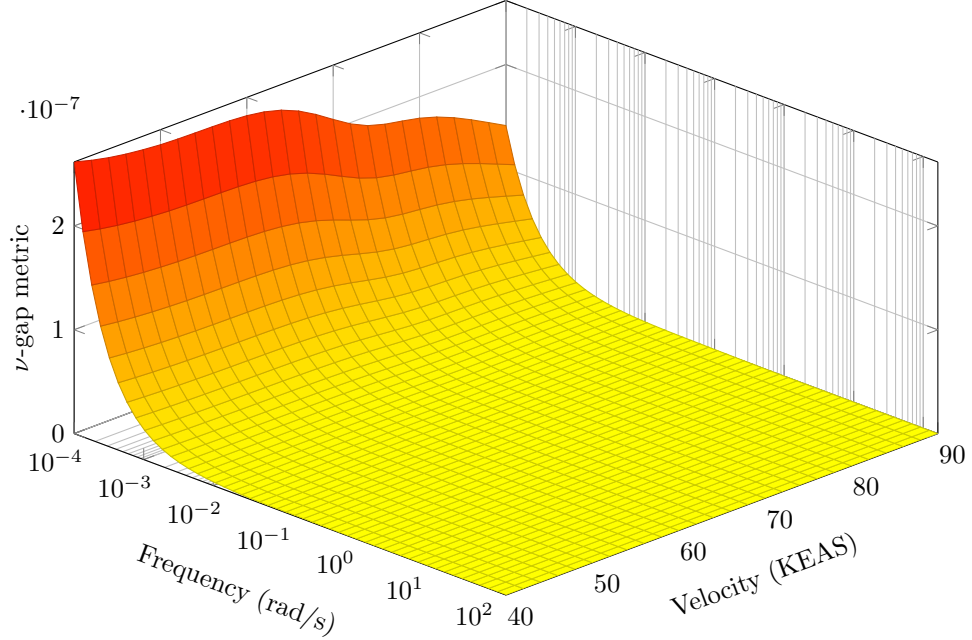
Figure 4.4: Variation of the ν-gap metric with respect to frequency and airspeed: Computed between full order model (148 states) and truncated model (146 states)

content outside the bandwidth of interest as described in the following subsection.

4.3.2 Modal Truncation

Modal truncation is chosen to eliminate the high-frequency modes outside the bandwidth of interest. A constant linear transformation, T_{64}, computed at 64 KEAS, is used to display the states with major contributions to the modes of the model with 146 states. This modal transformation decouples the model at 64 KEAS and exhibits that 50 states are related to high-frequency modes outside the bandwidth of interest. A quasi-modal LPV model is generated by applying the constant transformation T_{64} at all flight conditions and 50 identified high-frequency states are truncated from the model. This step leads to a LPV model with 96 states.

Figure 4.6 shows a comparison of the frequency responses between the truncated model with 146 states and the new modal reduced model with 96 states. As in the previous subsection, the bode plots correspond to the transfer functions from the left body flap deflection to the pitch rate measurement and the right outboard flap deflection to the left forward wing accelerometer at 42 and 72 KEAS flight conditions. In this case, model mismatches beyond 160 rad/s, corresponding to lightened areas, are not considered. The
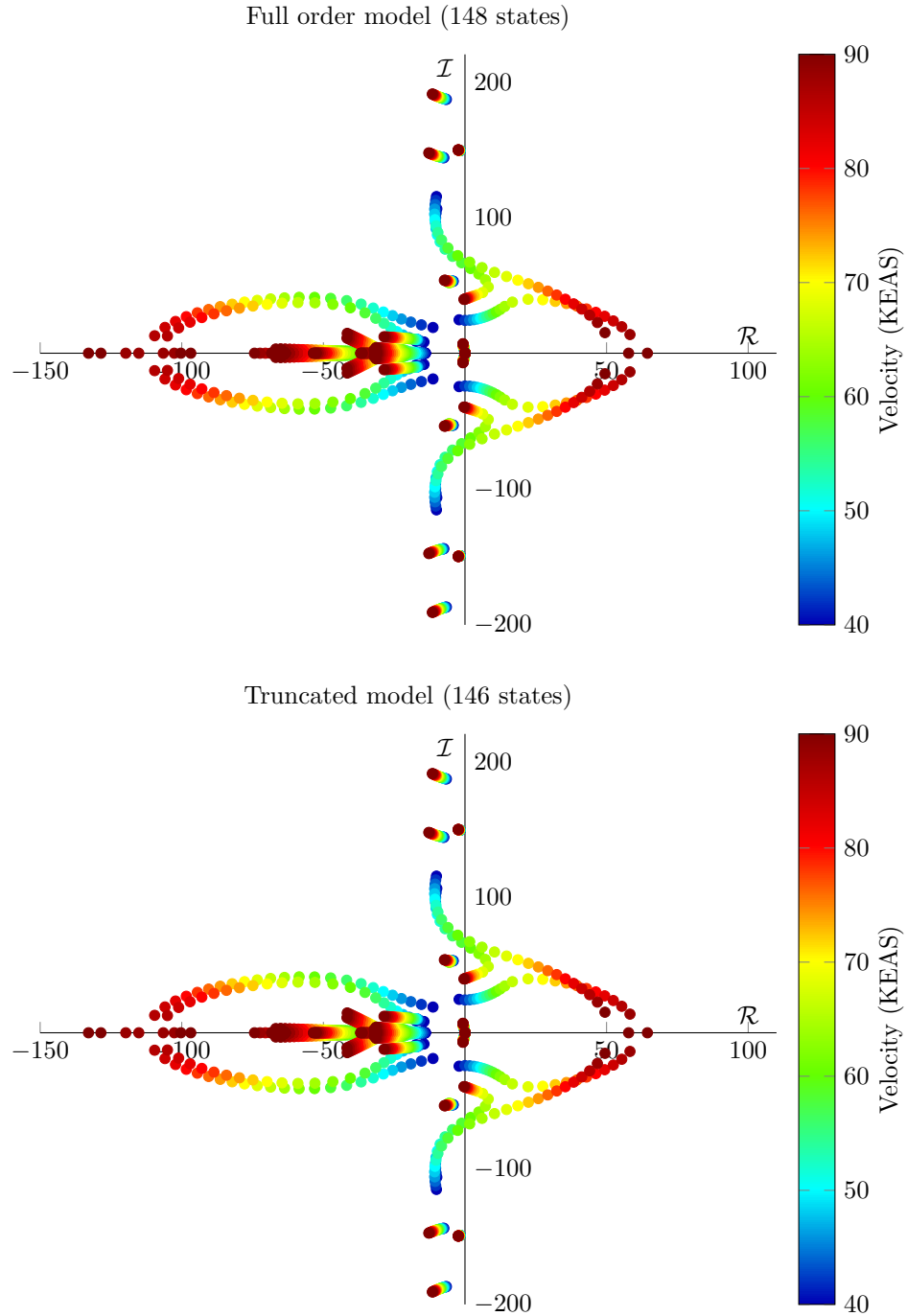
Figure 4.5: Pole migration across the flight envelope for full order model and truncated model

plots show that the frequency response of the selected input/output transfer functions match accurately within the bandwidth of interest (10-160 rad/s).
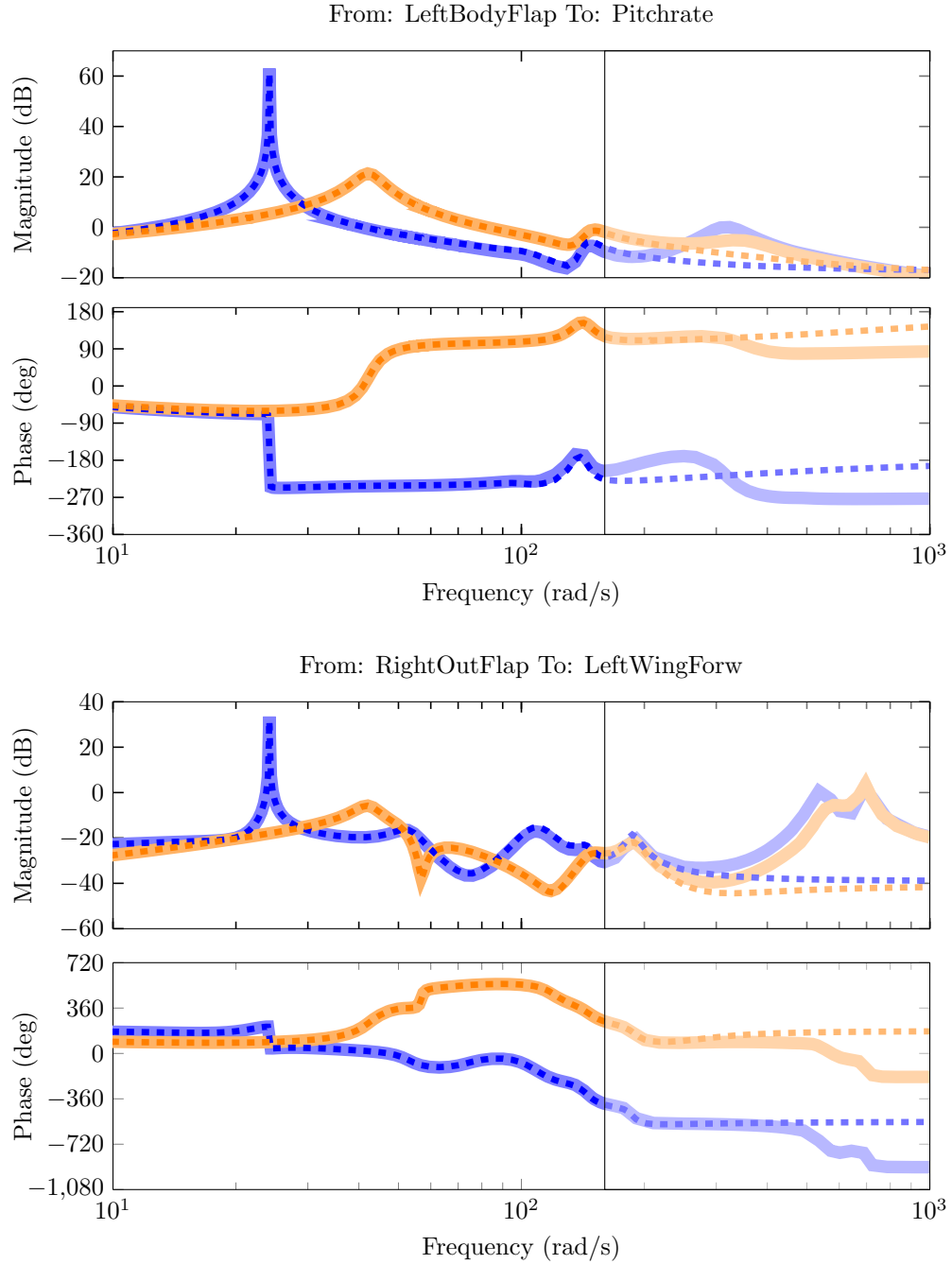
Figure 4.6: Bode plots of truncated model (146 states) at 42 KEAS (▬) and 72 KEAS (▬) compared to modal truncated model with 96 states (▪▪▪ / ▪▪▪). Lighter areas denote frequency range of no interest.

Figure 4.7 plots the frequency dependency of ν-gap metric between the truncated model and the new modal reduced model with 96 states for all flight conditions. Notice here that

the ν-gap metric is below 0.2 at all flight conditions in the bandwidth of interest. These values for the ν-gap metric are considered good and indicate that the closed-loop response of both reduced models are very similar.
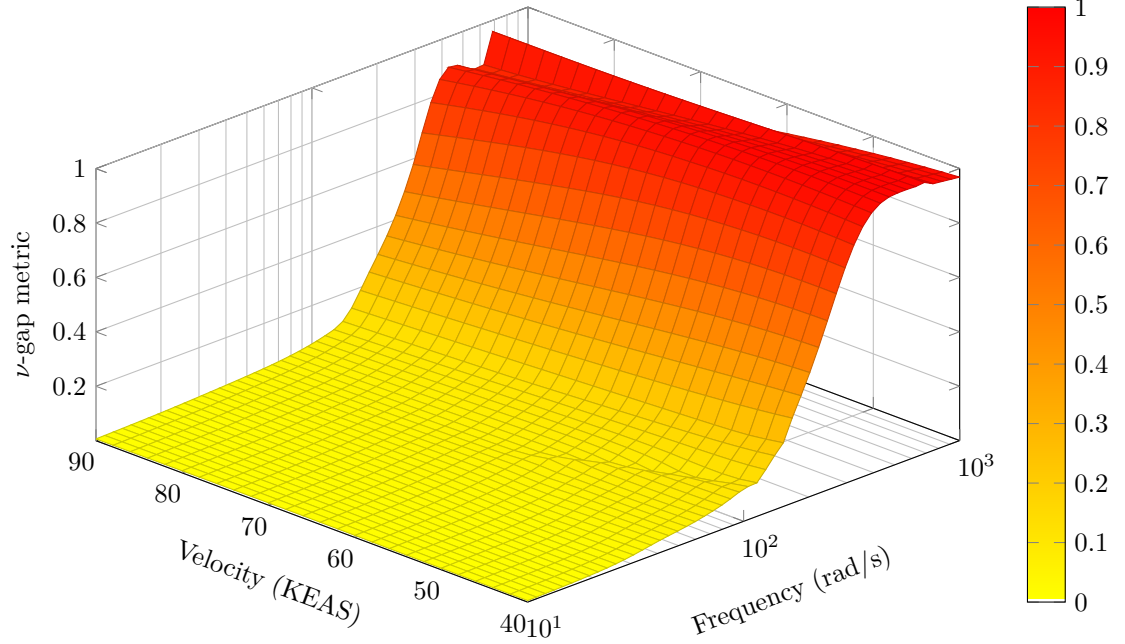
Figure 4.7: Variation of the ν-gap metric with respect to frequency and airspeed: Computed between truncated model (146 states) and modal truncated model (96 states)

Figure 4.8 shows the pole migration of the modal truncated model with respect to the velocity. Comparing this plot to the full order model pole migration (Fig. 4.5), it is observed that the unstable dynamics follows the expected trajectory. Hence, the truncation of high-frequency modes beyond 160 rad/s does not affect the predominant dynamics of the system. With this last validation, the LPV model with 96 states is accepted as a good match of the LPV full order model within the bandwidth of interest. Following, the elimination of modes with multiplicity greater than 1 is presented.

4.3.3 Residualization

Residualization of states is preferred when fidelity of the approximation at low frequencies is of interest. In this step, modes of multiplicity greater than 1 are residualized based on their ν-gap metric values. The ν-gap metric elimination threshold is set at 0.1, meaning that a state is eliminated if the ν-gap metric between the non-residualized and residualized model, within the bandwidth of interest, is less than 0.1 at all flight conditions. From this
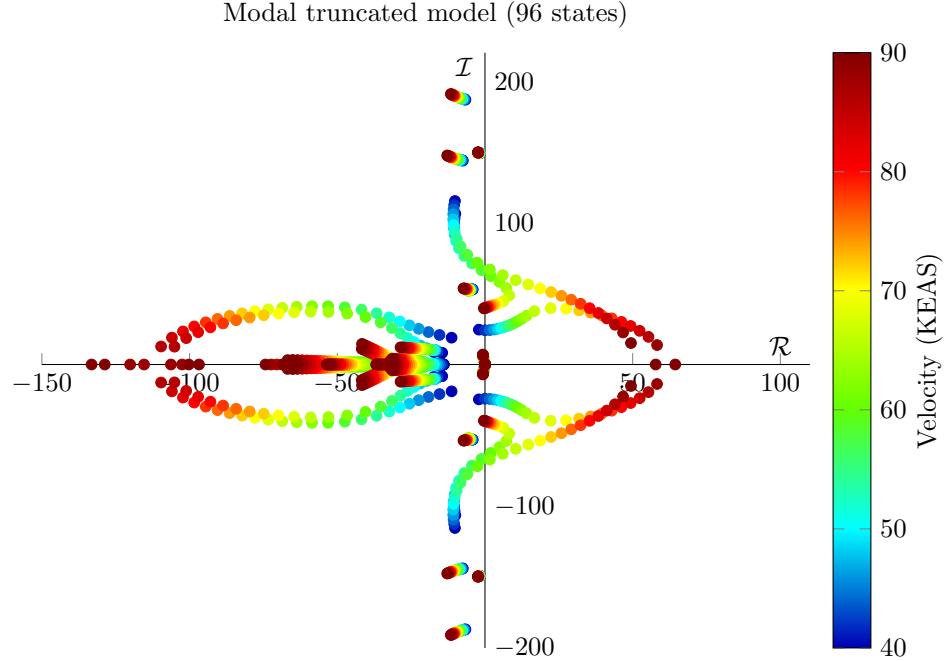
Figure 4.8: Pole migration across the flight envelope for modal truncated model

iteration, 55 states that achieve the ν-gap metric threshold are residualized to obtain a LPV model with 41 states.

Figure 4.9 shows a comparison of the frequency responses between the modal truncated model with 96 states and the new residualized model with 41 states. Again, bode plots of the transfer functions from the left body flap deflection to the pitch rate measurement and the right outboard flap deflection to the left forward wing accelerometer are shown for the 42 and 72 KEAS flight conditions. The bandwidth of interest (10-160 rad/s) corresponds to the highlighted area. Notice that there is a phase shift in the transfer functions corresponding to 42 KEAS. Originally, this flight condition is marginally stable, having a pair of complex poles very close to the imaginary axis. This indicates that the modal damping is almost zero and hence, small changes in the real value of these poles can lead to shifts in the phase values. In this case, the modal damping corresponding to the marginal stable mode is of the order of 10^{-4} in the full order model. The residualization procedure slightly moves this marginal stable pole to the right half plane, which has a new modal damping approximately of -10^{-4}. Here, negative damping indicates unstable modes. From this analysis it is concluded that the slightly shift of the pole at 42 KEAS does not affect the response of the system and hence, can be neglected. This statement is also confirmed from the ν-gap metric values across the frequency range of interested presented next.
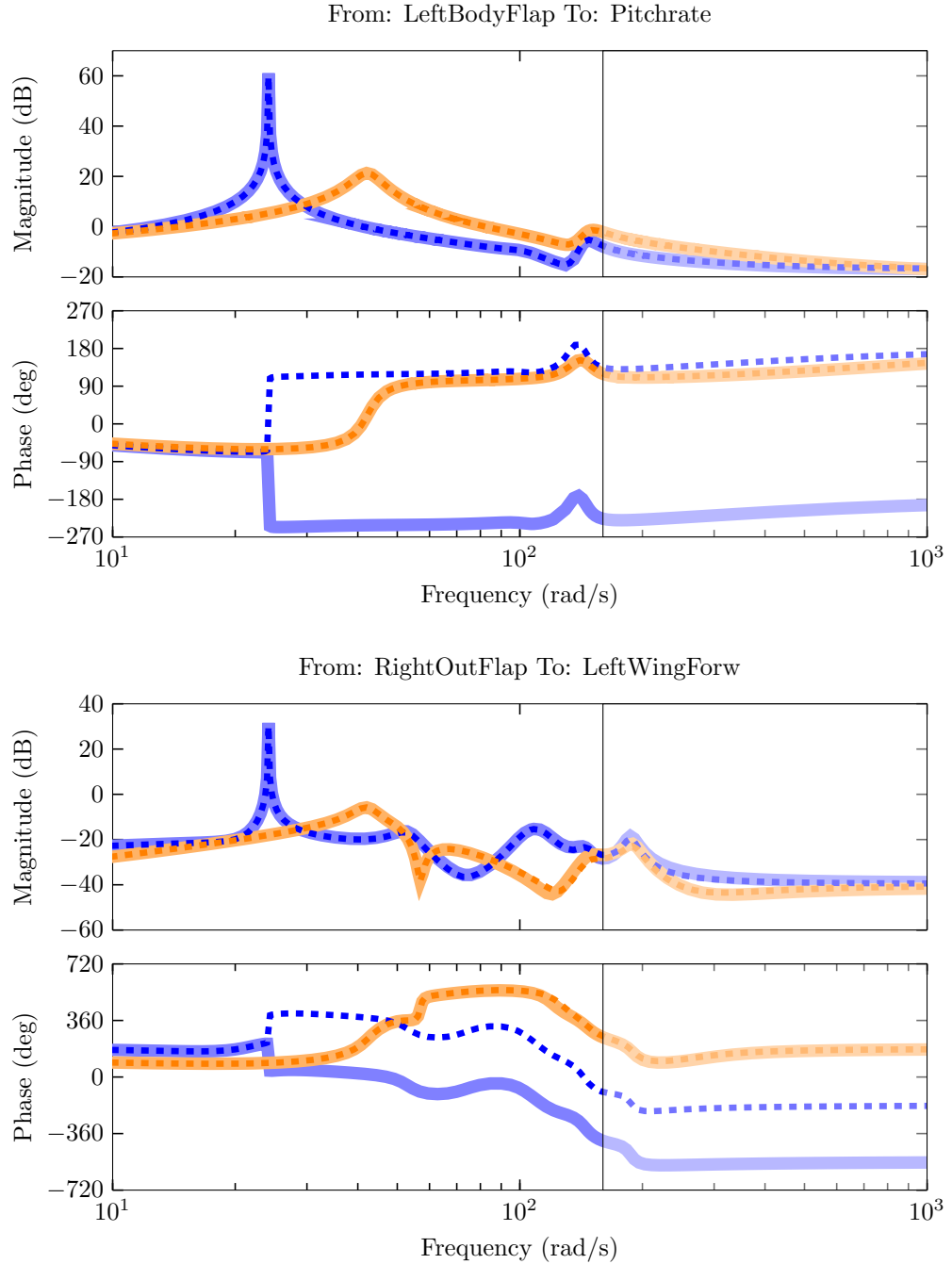
Figure 4.9: Bode plots of modal truncated model (96 states) at 42 KEAS (■) and 72 KEAS (■) compared to residualized model with 41 states (▪▪▪/▪▪▪). Lighter areas denote frequency range of no interest.

Figure 4.10 plots the frequency dependency of ν-gap metric between the modal truncated

model and the new residualized model with 41 states for all flight conditions. It is observed that the ν-gap metric is below 0.2 at all flight conditions in the bandwidth of interest. Notice that these values for the ν-gap metric are higher than the decision threshold set for elimination of states. However, the elimination of the whole set of states that individually introduce a ν-gap metric less than 0.1, can only be expected to be worse than this threshold. In addition, values for the ν-gap metric less than 0.2 are considered good and hence, the LPV residualized model is said to be similar to the LPV modal truncated model in the ν-gap metric.
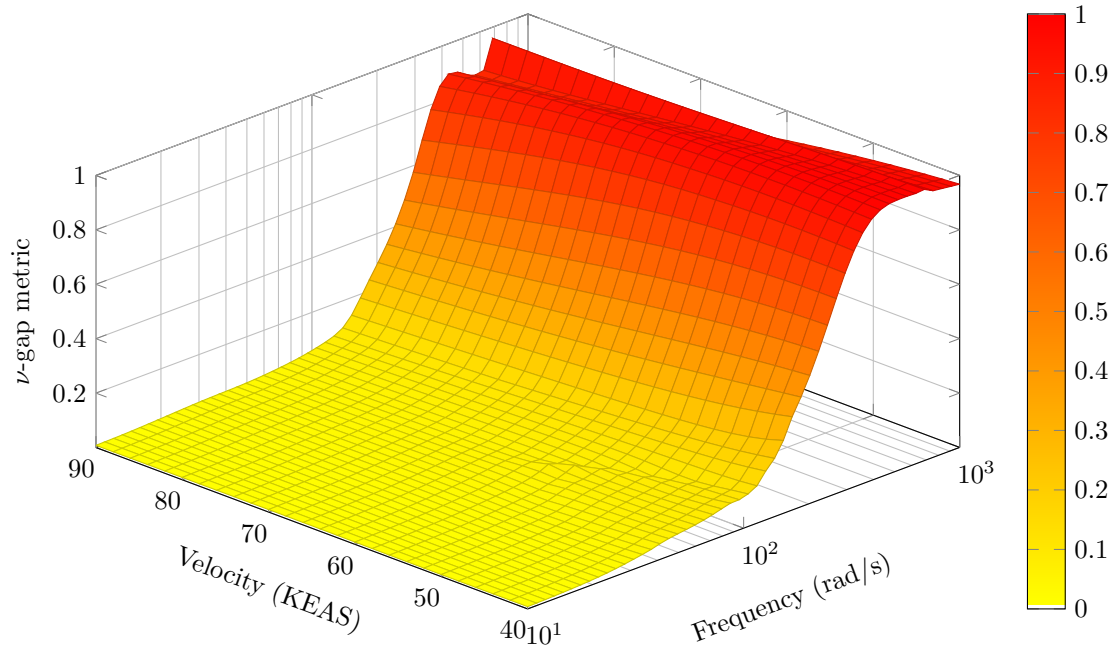
Figure 4.10: Variation of the ν-gap metric with respect to frequency and airspeed: Computed between modal truncated model (96 states) and residualized model (41 states)

Figure 4.11 shows the pole migration of the residualized model with respect to the velocity. Comparing this plot to the modal reduced model pole migration (Fig. 4.8), it is observed that the unstable dynamics follows the expected trajectory. Note that this residualization step removes the complex pair poles located very close to the imaginary axis that were still present in the modal truncated model. Also note that the shifting of the pole at 42 KEAS follows the trajectory expected and hence, does not make a big difference in the system response. The next step is then to find a LPV balanced realization of this residualized model with 41 states and eliminate the least controllable and observable states. This last procedure is presented below.

Residualized model (41 states)
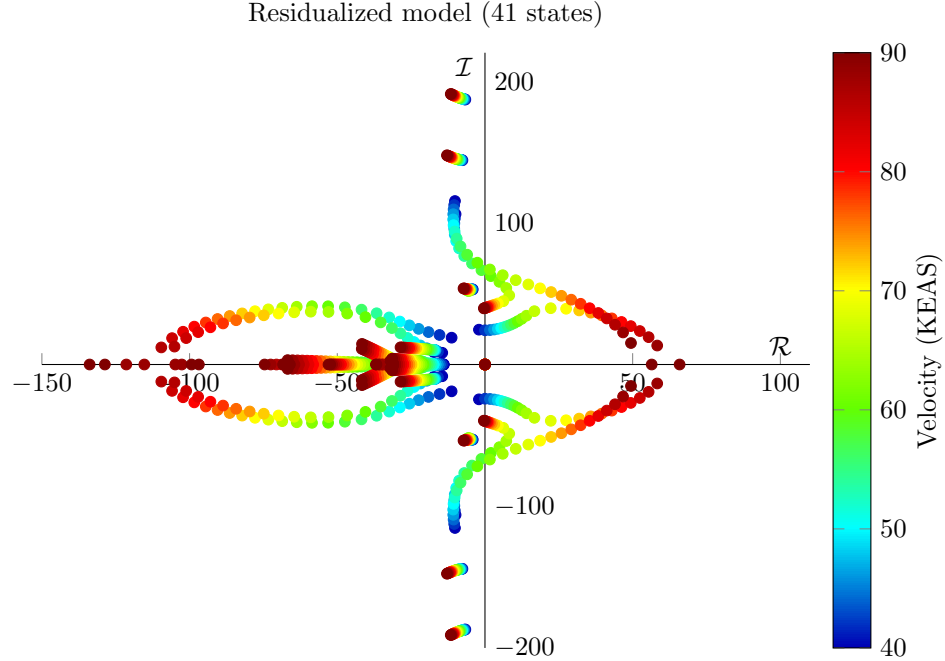
Figure 4.11: Pole migration across the flight envelope for residualized model

4.3.4 Balanced Coprime Factorization Residualization

The objective is to find a balanced realization based on the coprime factorization of the LPV system and eliminate the least controllable and observable states. A right-coprime factorization of the 41 states LPV model is used to compute the generalized controllability and observability Gramians of the system. These Gramians are built from the solutions of Riccati inequalities associated to the LMIs in (4.36) and (4.37).

Note that the size of each LMI problem grows as function of the state order n, number of parameters n_ρ, and parameter griding ρ_i of the LPV system. The number of decision variables, k, to solve for symmetric matrices is related with the state order as $k = n(n+1)/2$. Hence, the LMI problem specified for the residualized LPV model with 41 states requires the solution of 861 decision variables subject to 27 feasibility constraints. These constraints result from the parameter gridding of the LPV system, in this case the 26 flight conditions available for the BFF model, and the required positive definite condition of the variable matrices, X and Y. LMI Lab in the Robust Control Toolbox for MATLAB [51] is used to find positive definite, symmetric feasible solutions for X and Y of 41×41 dimension. These solutions are computed after 3 hours using a standard personal computer. Then, the controllability and observability Gramians, P and Q are obtained by replacing the X and

Y feasible solutions in (4.34).

The balancing transformation T_b is obtained from singular value decompositions of the generalized Gramians as in (4.42). This transformation finds a balanced realization of the LPV coprime factorization such that its Gramians are equal and diagonal. The diagonal entries of the balanced Gramians are the so called Hankel singular values. These values, associated with the combined controllability and observability of the system, are plotted in the Fig. 4.12. This bar plot shows that 20 balanced states have Hankel singular values less than 0.25. Hence, a balanced LPV model with 21 states is obtained by residualizing the 20 states with the smallest Hankel singular values. This last procedure is validated by comparing the LPV balanced model with the LPV full order model as presented below.
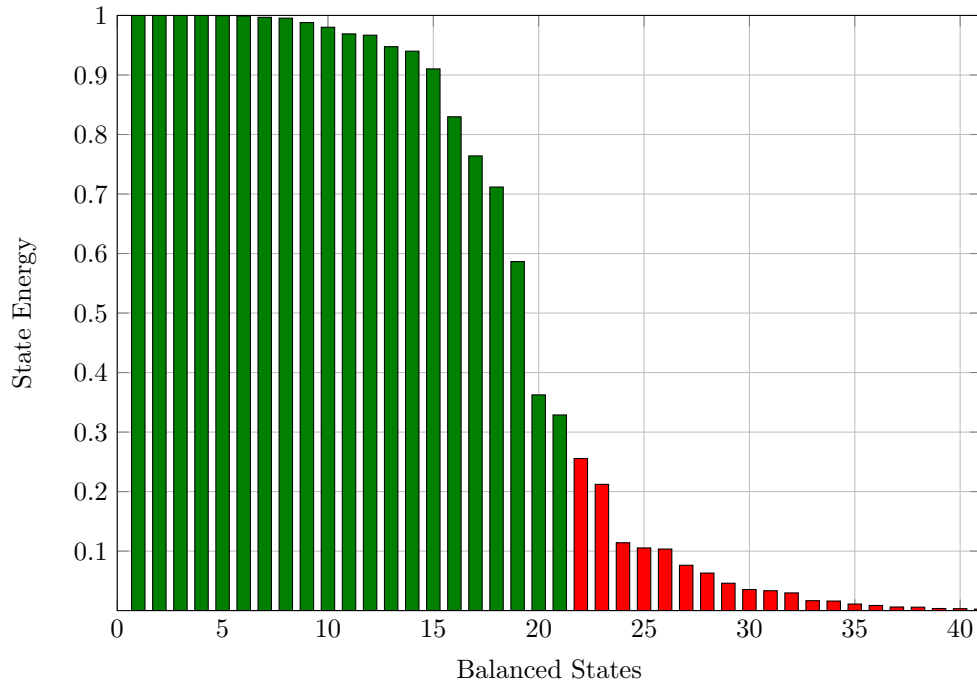
Figure 4.12: Hankel singular values: States contribution to controllability and observability

Figure 4.13 shows a comparison of the frequency responses between the full order model with 148 states and the balanced reduced model with 21 states. The same input/output transfer functions presented in previous subsections, are shown in these bode plots. Notice that the balanced residualized model at $42\,\mathrm{KEAS}$ reduces significantly the magnitude of the marginally stable mode. However, the phase shift produced by the model reduction indicates that the response of the system grows infinitely with time and hence, the amplification of the system at this particular frequency is very high. On the other hand, the balanced reduced model seems to capture accurately the input/output relationships in the frequency

range of interest at all flight conditions.

Figure 4.13: Bode plots of full order model (148 states) at 42 KEAS ( ) and 72 KEAS ( ) compared to balanced residualized model with 21 states (- - - / - - -). Lighter areas denote frequency range of no interest.

66

Figure 4.14 plots the frequency dependency of ν-gap metric between the full order model with 148 states and the new balanced reduced model with 21 states for all flight conditions. This plot shows that the ν-gap metric is less than 0.2 for almost all the frequency range of interest. A higher ν-gap metric value of 0.3 is achieved at approximately 160 rad/s, however ν-gap metric values of 0.3 are acceptable because the closed-loop responses of both systems are still similar when the same controller is used.

Figure 4.15 shows the pole migration of the balanced reduced model with respect to the velocity. Comparing this plot to the residualized model pole migration (Fig. 4.11), it is observed that balancing the system modifies the location of the stable poles (i.e. left-half plane poles). This is to be expected from balanced reduction methods because only the singular hankel values are invariant under balanced transformations (see (4.38)). On the other hand, it is observed that the unstable poles and their trajectory across the flight envelope are preserved on the balanced reduced model. However, notice that the unstable real poles present at 90 KEAS are slightly changed into a complex pair pole with equivalent frequency and modal damping. Because the second order system created with the positive real poles is equivalent to the system with the complex poles, it is concluded that the balanced residualized model represents accurately the predominant dynamics of the aircraft. The following subsection compares this LPV balanced reduced model (41 states) with a set of LTI reduced order models resulting from neglecting the LPV nature of the system.

4.3.5 LTI Model Reduction at Individual Flight Conditions

This subsection shows that a lower order model can be obtained by treating the models at individual flight conditions as LTI systems. These results set a lower bound for the model reduction problem for the LPV ASE model of the vehicle. The model reduction procedure applied to the LTI systems is the same as described for the LPV model. However, in this case individual similarity transformations are computed for each of the 26 models. For instance, the corresponding modal transformations at each flight condition decouple the LTI systems at those particular velocities. Hence, the naturally LPV description of the ASE model is lost under these transformations.

On the other hand, the solutions for the controllability and observability Gramians are obtained by solving the equivalent form of the Riccati equations in (4.33) and (4.35) at each flight condition. Here, the balanced realization of the LTI coprime factorization is also obtained by computing the corresponding similarity transformations at each flight condition. In this case, LTI reduced models with 17 states are obtained. This means that

67
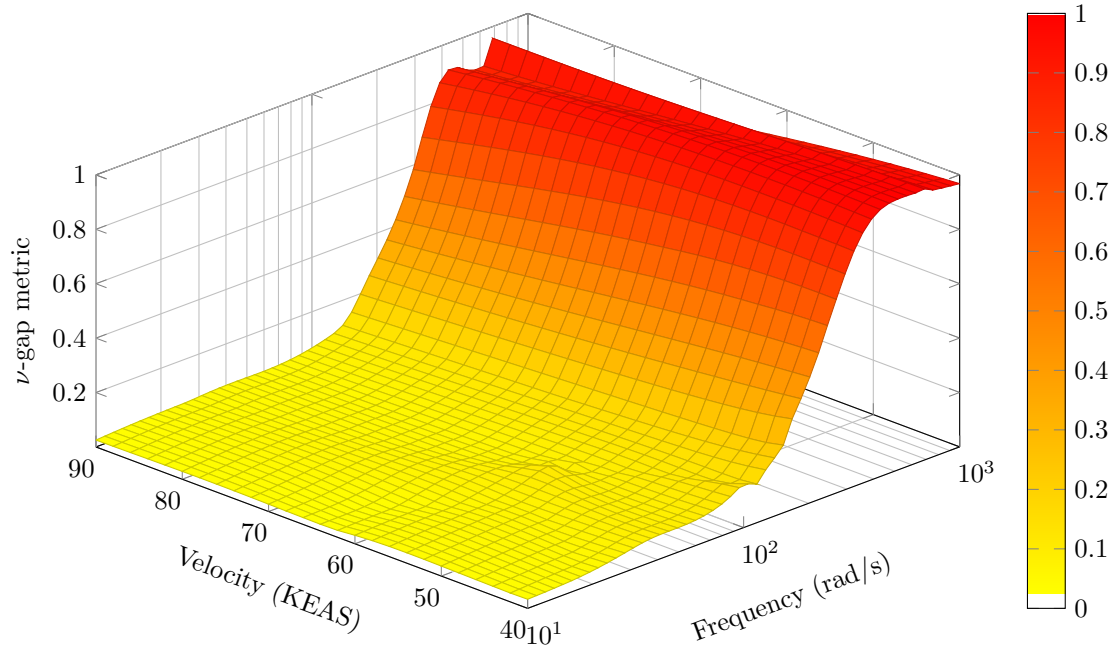
Figure 4.14: Variation of the ν-gap metric with respect to frequency and airspeed: Computed between full order model (148 states) and balanced residualized model (21 states)

Balanced residualized model (21 states)
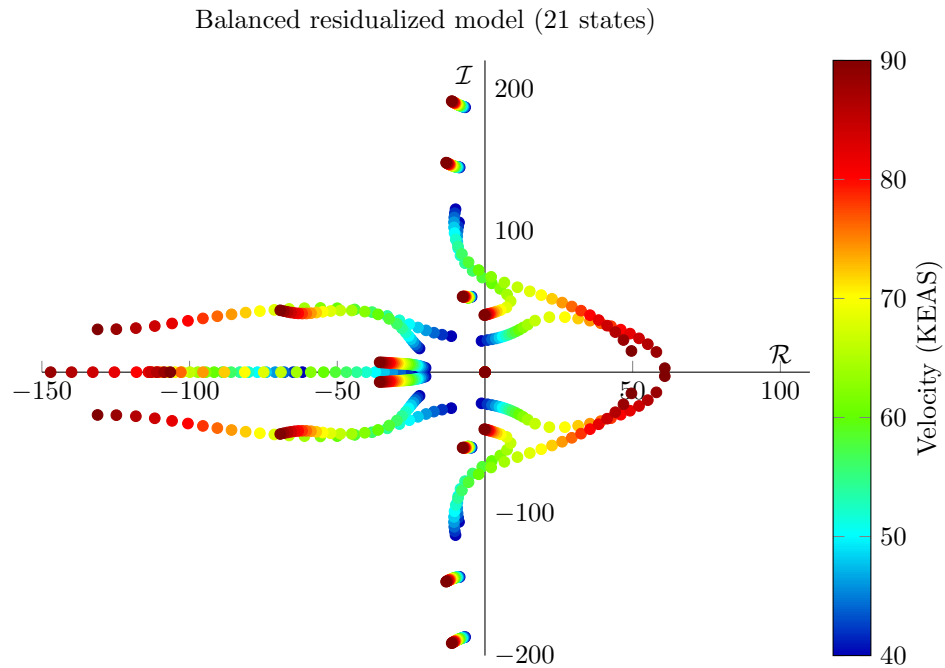
Figure 4.15: Pole migration across the flight envelope for balanced residualized model

the ASE model can not be reduced further than 17 states even when a single LTI model at a particular flight condition is used.

Figure 4.16 compares the frequency response of the full order model (148 states), LPV balanced reduced model (21 states) and LTI balanced reduced model (17 states) for flight conditions at $42\,\text{KEAS}$ and $72\,\text{KEAS}$. The plots show that the LTI reduced model is very similar to the LPV reduced model as it matches accurately the frequency bandwidth of interest. This is confirmed by the ν-gap metric values between the full order model and the LTI reduced model in Fig. 4.17. Here the ν-gap metric values across the frequency range of interest is below 0.25 for all individual flight conditions. In addition, the ν-gap metric values between the LPV reduced model and LTI reduced model are shown in Fig. 4.18. This plot indicates that the LPV and LTI reduced models are extremely close in the ν-gap metric sense, which means that both models preserve the important dynamics in the bandwidth of interest. Notice that the highest differences between the LPV and LTI reduced models is presented around velocities of $60\,\text{KEAS}$. Recall that the aircraft exhibits three unstable flutter interactions at these velocities. Because the dynamics of the system varies significantly at those velocities, the LPV reduced model needs to retain additional states to capture accurately these variations across the flight envelope.

4.4   Summary

This chapter described a four-step model reduction procedure for aeroservoelastic models based on classical and balanced model reduction techniques. These techniques are: (1) truncation, (2) modal truncation, (3) residualization, and (4) balanced coprime factor residualization. The motivation of using the first three procedures in aeroservoelastic systems is related to the computational complexity associated to balancing coprime factors of very high order. Because the balancing problem grows with the number states of the system and varying-parameters, feasible solutions to this problem are very hard to find for high-order systems. Hence the need of pre-processing steps previous to the balanced coprime reduction problem.

The procedure was successfully applied to the experimental Body Freedom Flutter aircraft, originally modeled with 148 states, to obtain an LPV balanced reduced model with 21 states. This model is considered suitable for control synthesis as it will allow the design of gain-scheduled multivariable controllers that guarantee robust stabilization and performance across the flight envelope. The following chapter discusses the actuator and sensor selection considerations previous to the design of robust controllers.
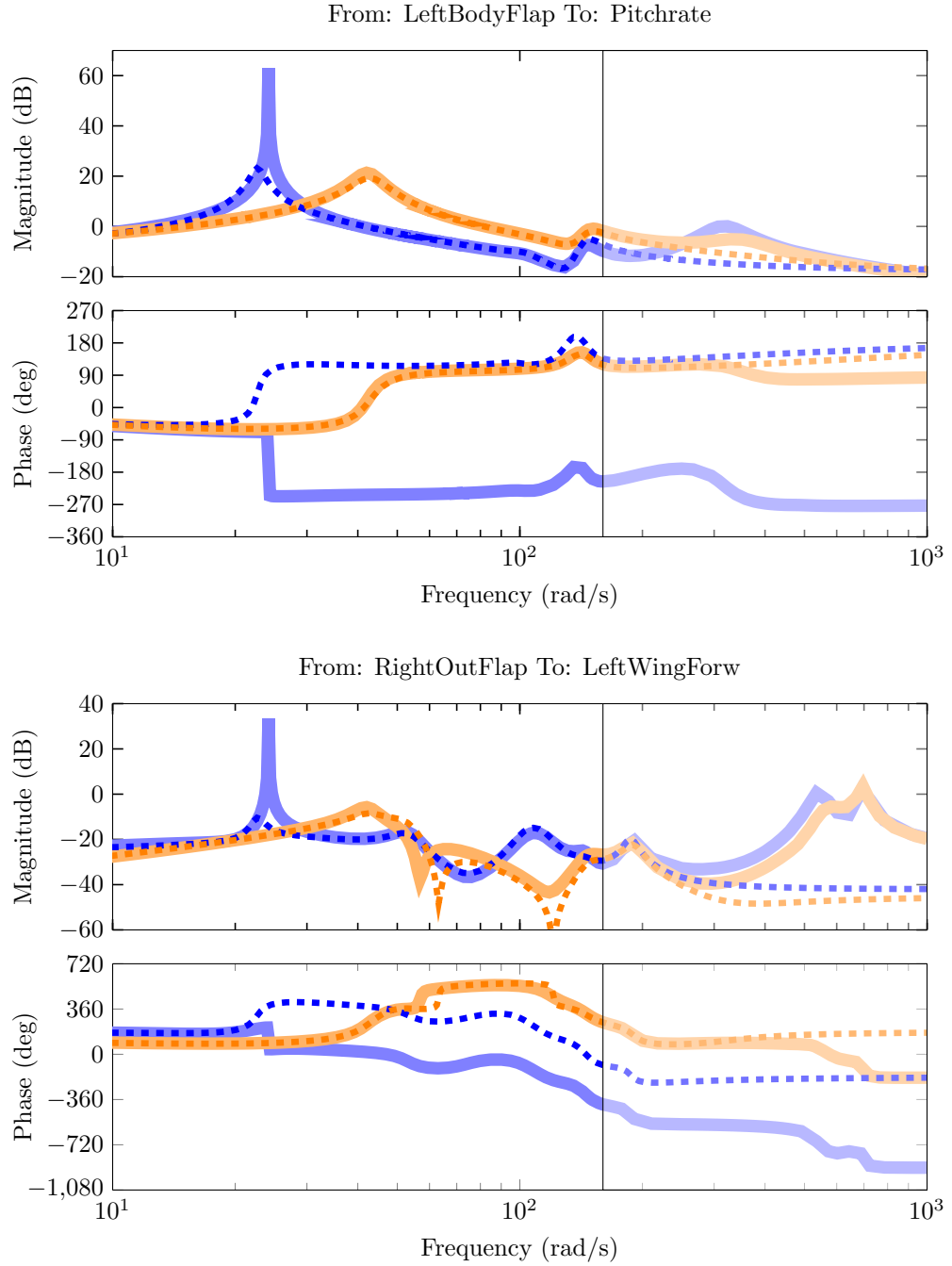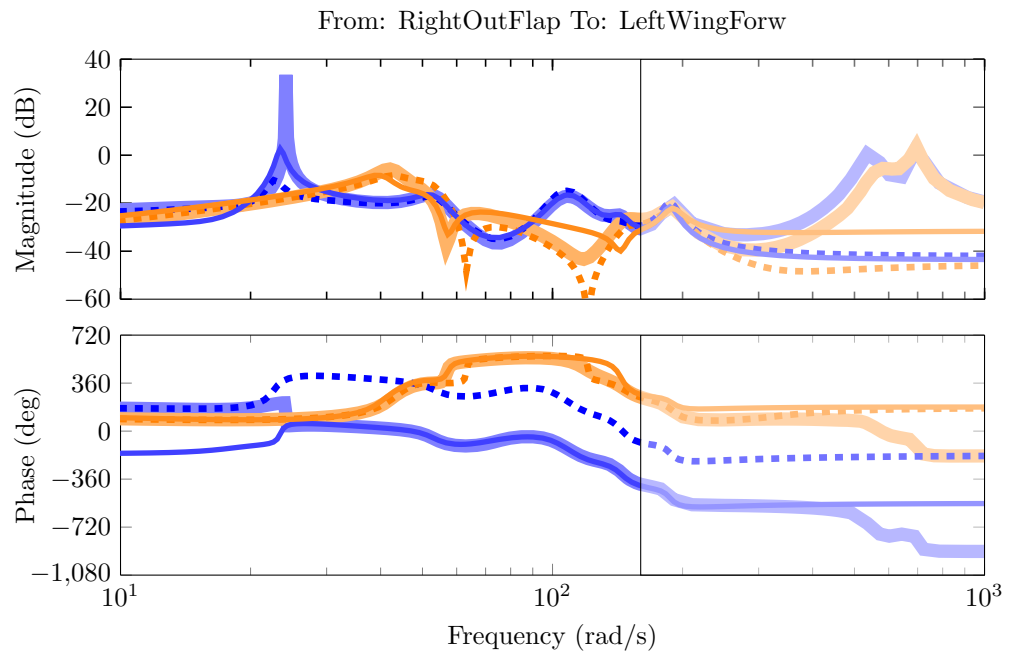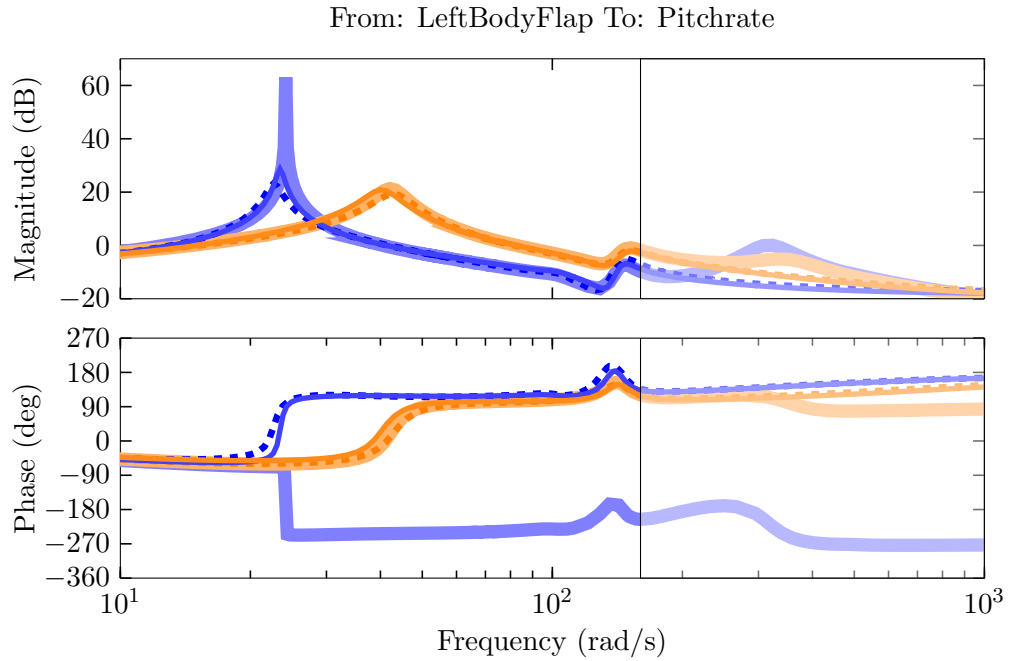
Figure 4.16: Bode plots of full order model (148 states) at 42 KEAS (▬▬) and 72 KEAS (▬▬) compared to LPV balanced reduced model with 21 states (▪▪▪/▪▪▪) and LTI balanced reduced model with 17 states (▬▬/▬▬). Lighter areas denote frequency range of no interest.
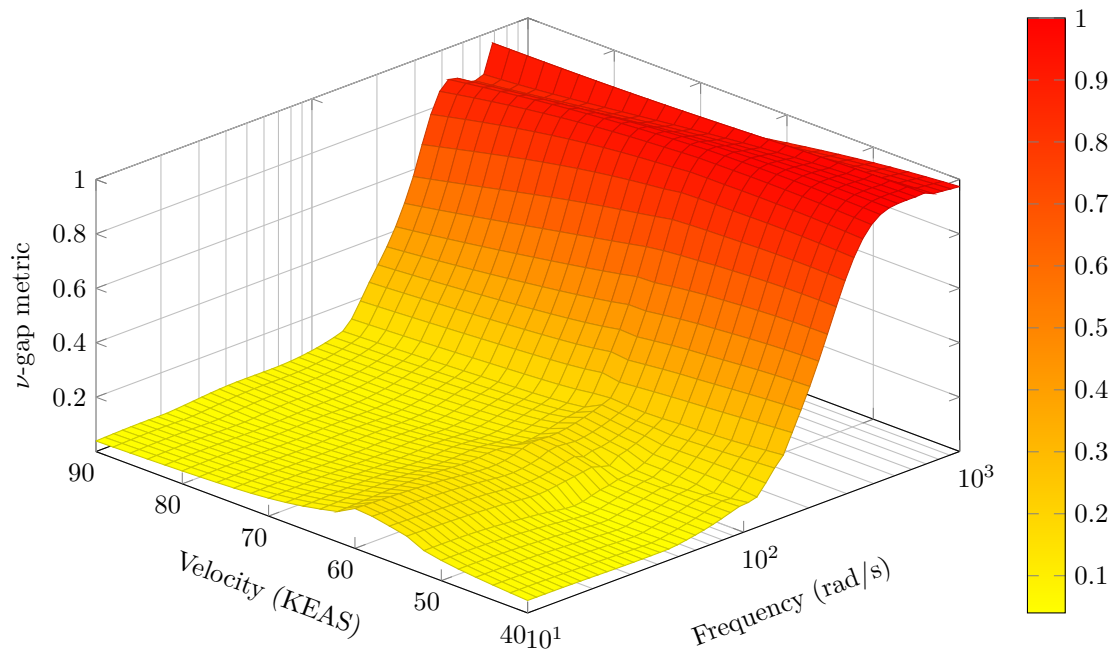
Figure 4.17: Variation of the ν-gap metric with respect to frequency and airspeed: Computed between full order model (148 states) and LPV balanced reduced model (21 states)
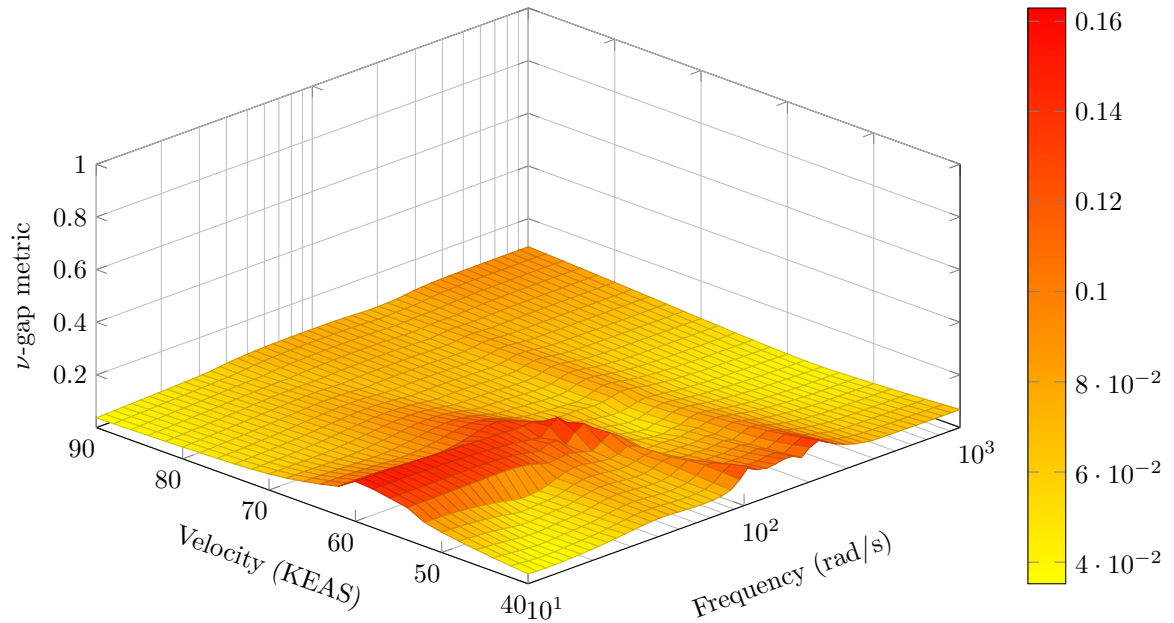
Figure 4.18: Variation of the ν-gap metric with respect to frequency and airspeed: Computed between LPV balanced model (21 states) and LTI balanced reduced model (17 states)

Chapter 5

Actuator and Sensor Selection for Aeroservoelastic Systems

This chapter presents an actuator and sensor selection approach for aeroservoelastic (ASE) systems. Selection of adequate sensor measurements and control effectors plays a critical role in the control design process. A wrong choice of actuator and sensors may put fundamental limitations on the performance and robustness that cannot be overcome by available advanced control design techniques. Hence, special attention to selection of input and output measurements for feedback control is required as an initial step in the design of controllers in order to successfully meet the desired performance. A brief review of the main methods for input/output selection found in the literature is presented in Section 5.1. Section 5.2 describes the problem formulation of the proposed actuator and sensor approach. Lastly, Section 5.3 presents the actuator and sensor selection results for the body freedom flutter (BFF) vehicle.

5.1   Literature Review: Input/Output Selection Methods

The selection of an appropriate number, place, and type of actuators and sensors plays a significant role in the design of controllers. Satisfying a set of performance objectives for a control system depends highly on the ability of its sensor measurements to determine the predominant dynamics and the ability of the actuators to correct the output responses. In general, a high number of sensors will provide more information to the controller and a high number of actuators will have a large influence on the system. However, these large quantities of instrumentation increase the costs of operation and maintenance of the

system, which is one of the major motivations for effective actuator and sensor selection. In addition, the use of less instrumentation for control decreases the probability of failure of the system, which makes the system more reliable. Hence, selection of actuator and sensors for feedback control has become a prerequisite for control design leading to the development of systematic methods that aid engineers in the design process [72].

Several methods to address the actuator and sensor selection problem are found in the literature. A majority of these methods can be grouped as control design independent and control design dependent methods. The great advantage of control independent methods is that they eliminate sets of inputs and outputs in a direct and efficient manner without involving any complete controller design. These methods are usually based on measures of input-output controllability and observability of the plant. They include the popular system frequency dependent condition number and relative gain array (RGA) measures [73–75]. A brief overview of these two methods is given below.

The condition number of the plant is defined as the ratio between its maximum and minimum singular values, $\text{cond}(G) = \bar{\sigma}(G)/\underline{\sigma}(G)$. This means that the condition number is large if both G and G^{-1} have large elements. In general, a small condition number indicates that the multivariable effects of uncertainty are not likely to be serious. On the other hand, a large condition number implies that the system is sensitive to unstructured input uncertainty. Large condition numbers may also mean that the RGA elements of the plant are large [67]. The RGA of a transfer matrix was introduced as a measure of robustness and interactions in decentralized control. This measure is defined as $\text{RGA}(G) = G \times (G^{-1})^T$, where $\times$ denotes element-by-element multiplication. Systems with large RGA elements are very sensitive to diagonal multiplicative input uncertainty if an inverse-based controller is used [72, 75]. This indicates that the system is fundamentally difficult to control and therefore, sets of inputs and outputs that causes large RGA elements should be avoided.

Even though control independent methods are direct and efficient, controllability measures are only a crude representation of the actual control objectives. In some cases, when the achievable closed-loop performance of the system is an important criterion, including the controller design in the selection of actuators and sensors results beneficial. Consequently, several methods for actuator and sensor selection based on closed-loop objectives have been developed. These methods can refer to nominal performance [76–80], robust stability and/or robust performance [81–84]. The most relevant control-dependent methods to this dissertation are reviewed next.

Balas et al. [80] proposed a systematic approach for sensor selection based on $\mathcal{H}_2$ optimal control design techniques. This approach exploits the well-known separation structure of

the $\mathcal{H}_2$ problem which is solved by combining the full information and output estimation problems. Here, the full information cost represents the best control possible by having all the system information available for feedback. Hence, if the full information cost is a large fraction of the output feedback $\mathcal{H}_2$ performance level, then the selected measurements are providing enough information of the system and hence, additional measurements will not help to improve the performance. The method was applied to the selection of sensors for active vibration attenuation on an experimental structure indicating that acceleration measurements for feedback control are better than displacement measurements for this particular problem.

Recently, the problem of sensor and actuator selection based on nominal performance was also approached by Dhingra et al. [77]. The proposed method evaluates the degradation of the $\mathcal{H}_2$ performance level by designing a global optimal state feedback controller for actuator selection and a global optimal state observer for sensor selection. In addition, a convex sparsity-promoting term is included in order to eliminate the combinatorial nature of the problem. The optimal solutions for this problem are obtained from a customized algorithm that is well-suited for large-scale systems. Here, the design of $\mathcal{H}_2$ optimal controllers does not include modeling error in the problem formulation. Hence, this methodology is particularly suitable when the achievable robust performance level is close to the optimal nominal performance of the system.

Robust performance objectives are included in the actuator and sensor selection method developed by Lee et al. [84]. This method eliminates undesirable input/output candidates for which a robust controller does not exist. The screening tools are based on the structured singular value theory to compare the level of performance achieved in the presence of model uncertainty. A shortcoming of the method is that the necessary conditions for existence of a controller achieving the desired robust performance is a result of dropping the stabilizing property of the controller. This means that sets of actuator and sensors for which a stabilizing controller achieves the specified robust performance may not be constructed. Hence, this method is particularly challenging for ASE systems where stabilization plays a significant role.

This chapter proposes an actuator and sensor selection method for ASE systems that is based on robust stability and robust performance closed-loop objectives. Here, $\mathcal{H}_\infty$ controllers that are robust to uncertainties in the model are used to compare the level of robust performance for a determined group of sensors or actuators. Similar to the approach presented in [80], the selection of actuators is based on the full information problem where the information provided to the controller corresponds to all the states of the system. On

the other hand, the selection of sensors is based on the full control problem where the control signal has access to the all the states through output injection. The proposed method for input and output selection is described in the next section followed by its application to the body freedom flutter (BFF) vehicle.

5.2 Problem Formulation

The actuator and sensor selection for ASE systems is formulated as follows: Given a number of available actuators and sensors for feedback control, we are interested in obtaining a subset of control inputs and measurements that achieves the desired performance objectives and provides sufficient robustness to model uncertainty.

The approach proposed to address this problem consists of two procedures. First, robust full-information (FI) controllers are designed for different actuator configurations u_i, and their performance is compared to obtain an optimal selection of actuators. Second, robust full-control (FC) controllers are designed for different sensor configurations y_i. Again, the performance is compared to optimally select sensors. Notice that the full set of all combinatorial choices of actuators and sensors is large and unwieldy. Hence, this procedure is executed for a limited number of configurations to expedite the analysis.

The FI and FC problems are special cases of the output feedback control problem, where the FI plant provides the controller directly with states as measurements, while the FC plant assumes that the controller directly affects the states. The advantage of using the FI and FC formulations is that they are both convex problems. Hence, a globally optimal controller can be synthesized for each sensor/actuator configuration, and the controller performance for each configuration can be directly compared.

On the other hand, the design of output feedback controllers without the FI and FC assumptions, yields a non-convex problem [85]. A well-known method to solve this non-convex problem is the DK-iteration [86,87]. However, the DK-iteration does not synthesize globally nor locally optimal controllers, leaving the performance of controllers depending not only on the selected configuration but also the initial condition of the algorithm. Hence, the performance of these controllers cannot be directly compared for different configurations. Thus, this dissertation uses the FI and FC assumptions for the actuator and sensor selection analysis.

A review of the mathematical details of the robust control formulation follows. Consider the general control synthesis configuration for uncertain systems in Fig. 5.1. Here G is a linear time invariant (LTI) system, K is the controller, and Δ is the model uncertainty.

The performance objectives are collected in e, and the disturbances are collected in d. The controller is provided with measurements y and generates control inputs u. In addition, the dynamic model uncertainty Δ is assumed to lie in the set

$$\mathbf{\Delta}_{1/\gamma} =: \{\mathrm{diag}(\Delta_1, \ldots, \Delta_s)|\, \|\Delta_k\| \leq \gamma^{-1}, k = 1, \ldots, s\} \tag{5.1}$$
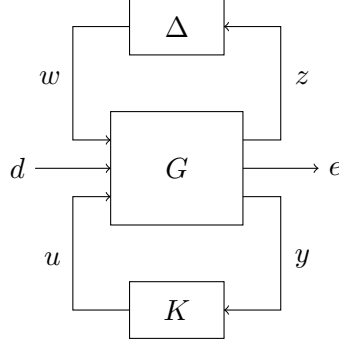
Figure 5.1: Robust control configuration

The robust control problem is to find a stabilizing controller K that minimizes the $\mathcal{H}_\infty$ norm of the closed-loop transfer function from d to e while maximizing the robustness against the uncertainty Δ. This robust performance synthesis is formulated as

$$\inf_K \left(\sup_{\Delta \in \mathbf{\Delta}_{1/\gamma}} \|F_U(F_L(G, K), \Delta)\| \right) \leq \gamma \tag{5.2}$$

where the linear fractional transformation $F_U(F_L(G, K), \Delta)$ denotes the uncertain closed-loop transfer function, $\|\cdot\|$ denotes the induced L_2 norm of the system, and γ denotes the robust performance (RP) level achieved by the controller.

The optimization problem in (5.2) can be turned into a norm computation of a scaled system such that

$$\inf_K \left(\inf_{\Theta \in \mathbf{\Theta}} \left\| \Theta^{1/2} F_L(G, K) \Theta^{-1/2} \right\| \right) < \gamma \tag{5.3}$$

where the scalings Θ belong to the set

$$\mathbf{\Theta} := \{\mathrm{diag}(\theta_1 I_{m_1}, \ldots, \theta_s I_{m_s}, I_h)|\theta_k > 0, k = 1, \ldots, s\} \tag{5.4}$$

with m_k as the dimension of the kth uncertainty block in (5.1) and h as the dimension of the performance objectives. Here, it is assumed that disturbance and performance channels

are both of dimension h. Notice that with this definition each $\Theta \in \boldsymbol{\Theta}$ has the property that it commutes with each $\Delta \in \boldsymbol{\Delta}_{1/\gamma}$, i.e. $\Theta\Delta = \Delta\Theta$.

The optimization problem in (5.3) is non-convex and there is no direct method to synthesize an optimal output feedback controller. However, this problem results in a convex optimization if the FI and FC special assumptions are considered for the control design. Following, the conditions for the FI problem are derived.

The FI nominal plant, G_{FI}, is defined by the state space model

$$
\begin{bmatrix} \dot{x} \\ e \\ y \end{bmatrix} = \begin{bmatrix} A & B_1 & B_2 \\ C_1 & D_{11} & D_{12} \\ I & 0 & 0 \end{bmatrix} \begin{bmatrix} x \\ d \\ u \end{bmatrix}
\tag{5.5}
$$

where $x \in \mathbb{R}^n$, $e \in \mathbb{R}^{n_e}$, $d \in \mathbb{R}^{n_d}$, $y \in \mathbb{R}^{n_y}$, and $u \in \mathbb{R}^{n_u}$.

The $\mathcal{H}_\infty$ robust FI problem is to find a stabilizing controller $u = Kx$ such that

$$
\inf_{\Theta \in \boldsymbol{\Theta}} \left\| \Theta^{1/2} F_L(G_{FI}, K)\Theta^{-1/2} \right\| < \gamma
\tag{5.6}
$$

where the scaled closed-loop transfer matrices $\Theta^{1/2} F_L(G_{FI}, K)\Theta^{-1/2}$ yields the state space

$$
\left[\begin{array}{c|c} A + B_2 K & B_1 \Theta^{-1/2} \\ \hline \Theta^{1/2}(C_1 + D_{12}K) & \Theta^{1/2} D_{11} \Theta^{-1/2} \end{array} \right]
\tag{5.7}
$$

The $\mathcal{H}_\infty$ norm computation in (5.6) can be transferred into a linear matrix inequality (LMI) optimization described by the following lemma.

Lemma 5.2.1 *Let the scaled closed-loop transfer function in (5.7) be a stable LTI system. Then* $\left\| \Theta^{1/2} F_L(G_{FI}, K)\Theta^{-1/2} \right\| < \gamma$ *if and only if* $\Theta \in \boldsymbol{\Theta}$ *and there exists a symmetric matrix* $P > 0$ *such that [88]*

$$
\begin{bmatrix} (A + B_2 K)^T P + P(A + B_2 K) & P B_1 \Theta^{-1/2} \\ \Theta^{-1/2} B_1^T P & -\gamma^2 I \end{bmatrix} +
\tag{5.8}
$$
$$
\begin{bmatrix} (C_1 + D_{12}K)^T \\ \Theta^{-1/2} D_{11}^T \end{bmatrix} \Theta \begin{bmatrix} (C_1 + D_{12}K) & D_{11}\Theta^{-1/2} \end{bmatrix} < 0
$$

The bi-linear terms in (5.8) are simplified using the Schur-complement. The result is then pre- and post-multiplied by the diagonal matrix $\mathrm{diag}(I, \Theta^{1/2}, \Theta^{-1/2})$ to obtain

$$
\begin{bmatrix} A^T P + PA + K^T B_2^T P + P B_2 K & P B_1 & C_1^T + K^T D_{12}^T \\ B_1^T P & -\gamma^2 \Theta & D_{11}^T \\ C_1 + D_{12}K & D_{11} & -\Theta^{-1} \end{bmatrix} < 0
\tag{5.9}
$$

As a final simplification, the first row and column of (5.9) are pre- and post-multiplied by P^{-1}. By defining $Q = P^{-1}$, $L = KQ$ and applying a Schur Complement, we obtain

$$\begin{bmatrix} QA^T + AQ + L^T B_2^T + B_2 L & QC_1^T + L^T D_{12}^T \\ C_1 Q + D_{12} L & -\Theta^{-1} \end{bmatrix}$$
$$+ \frac{1}{\gamma^2} \begin{bmatrix} B_1 \Theta^{-1} B_1^T & B_1 \Theta^{-1} D_{11}^T \\ D_{11} \Theta^{-1} B_1^T & D_{11} \Theta^{-1} D_{11}^T \end{bmatrix} < 0 \tag{5.10}$$

The LMI formulation in (5.10) is turned into a generalized eigenvalue problem to solve for a controller K that minimizes the RP level γ. This eigenvalue problem is computed using existing software such as LMILab and YALMIP. On the other hand, the conditions for the FC problem are similarly derived using the FI dual problem. Here, the full control plant is defined as $G_{FC} = G_{FI}{}^T$. These conditions are then used for the selection of sensors. Following, the application of these two procedures are presented for the experimental ASE vehicle.

5.3 Actuator and Sensor Selection for Body Freedom Flutter Vehicle

This section presents the actuator and sensor selection for feedback control of the BFF vehicle using the approach described in Section 5.2. The aircraft has 8 control surfaces and 11 sensors available for control. Sensor measurements include gyros, accelerometers and hot-film sensors located at the leading-edge stagnation point (LESP) to estimate the lift distribution. This configuration of sensors and control surfaces was depicted in Fig. 3.4.

The reduced order models with 21 states obtained in Chapter 4 are used to synthesize FI and FC controllers for several subsets of control surfaces and sensor measurements. The control objectives are to suppress the unstable flutter interactions observed at $44, 60$, and $62\,\mathrm{KEAS}$ and to increase the structural damping of the vehicle. Damping of modes can be achieved by generating a signal that is in phase with the modal velocities to reduce the structural vibration energy [89]. However, with the existent description of inputs and outputs of the system, modal velocities are not observed explicitly. Hence, a modification of the system's description is required to extract modal velocities as the performance objectives.

Modal velocities can be obtained by transforming the reduced order system, G_{ρ_r}, into

a second order modal realization such that at a fixed parameter $\rho = \kappa$

$$
\begin{bmatrix} \dot{\xi}_1 \\ \ddot{\xi}_1 \\ \vdots \\ \dot{\xi}_k \\ \ddot{\xi}_k \end{bmatrix} = \begin{bmatrix} 0 & 1 & & & \\ -\omega_1^2(\kappa) & -2\zeta_1(\kappa)\omega_1(\kappa) & & & \\ & & \ddots & & \\ & & & 0 & 1 \\ & & & -\omega_k^2(\kappa) & -2\zeta_k(\kappa)\omega_k(\kappa) \end{bmatrix} \begin{bmatrix} \xi_1 \\ \dot{\xi}_1 \\ \vdots \\ \xi_k \\ \dot{\xi}_k \end{bmatrix} + \begin{bmatrix} \bar{b}_{11,1}(\kappa) \\ \bar{b}_{21,1}(\kappa) \\ \vdots \\ \bar{b}_{1k,1}(\kappa) \\ \bar{b}_{2k,1}(\kappa) \end{bmatrix} u \quad (5.11)
$$

Here, it is assumed that the reduce order model has only complex conjugate eigenvalues $\lambda_k = -\zeta_k\omega_k \pm \omega_k\sqrt{1-\zeta^2}i$, where ω_k is the modal frequency and ζ_k is the modal damping. Consequently, the transformed coordinates ξ_k represent the modal deflections and $\dot{\xi}_k$ represent the modal velocities. The goal is now to find the transformation T, such that $\xi = Tx_r$ and (5.11) holds.

Rewriting the state matrix of the system in the real block diagonal form at (5.11), involves the real modal decomposition and the controllability matrices associated to each of the modes. The first step is to bring the reduced order model to its real modal decomposition such that $\hat{A}_r(\kappa) = T_1 A_r(\kappa)T_1^{-1}$ is block diagonal

$$
\hat{A}_r(\kappa) = \begin{bmatrix} \hat{A}_1(\kappa) & & & \\ & \hat{A}_2(\kappa) & & \\ & & \ddots & \\ & & & \hat{A}_k(\kappa) \end{bmatrix} \quad (5.12)
$$

where $\hat{A}_k(\kappa)$ is a 2×2 block representing the complex conjugate eigenvalue k and has the form

$$
\hat{A}_k(\kappa) = \begin{bmatrix} -\zeta_k(\kappa)\omega_k(\kappa) & \sqrt{\omega_k^2(\kappa) - \zeta_k^2(\kappa)} \\ -\sqrt{\omega_k^2(\kappa) - \zeta_k^2(\kappa)} & -\zeta_k(\kappa)\omega_k(\kappa) \end{bmatrix} \quad (5.13)
$$

If the system has real eigenvalues, $\hat{A}_k(\kappa)$ is a 1×1 with the corresponding real pole λ_k as entry. This block diagonal structure is then induced by the transformation matrix defined as

$$
T_1^{-1} = \begin{bmatrix} \Re\{v_1(\kappa)\} & \Im\{v_1(\kappa)\} & \cdots & \Re\{v_k(\kappa)\} & \Im\{v_k(\kappa)\} \end{bmatrix} \quad (5.14)
$$

where $v_k(\kappa)$ is the eigenvector associated to the complex conjugate eigenvalue $\lambda_k(\kappa)$ of the original state matrix $A_r(\kappa)$. Again, if the system has real eigenvalues then the corresponding real eigenvector is the only entry in the transformation matrix [90].

Once the system is in the real modal realization described by (5.13), each 2×2 block

$\hat{A}_k(\kappa)$ can be transformed into the second order form

$$\bar{A}_k(\kappa) = \begin{bmatrix} 0 & 1 \\ -\omega_k^2(\kappa) & -2\zeta_k(\kappa)\omega_k(\kappa) \end{bmatrix} \tag{5.15}$$

using a similarity transformation $t_k = s_k m_k$ where

$$s_k = \begin{bmatrix} \hat{B}_{k,1}(\kappa) & \hat{A}_k(\kappa)\hat{B}_{k,1}(\kappa) \end{bmatrix} \tag{5.16}$$

$$m_k = \begin{bmatrix} 2\zeta_k(\kappa)\omega_k(\kappa) & 1 \\ 1 & 0 \end{bmatrix} \tag{5.17}$$

Here, $\hat{B}_{k,1}(\kappa)$ corresponds to the first column of $\hat{B}_k = T_1 B_r(\kappa)$ and s_k represents the controllability matrix associated to the mode k. Then, a transformation T_2 such that $\bar{A}_r(\kappa) = T_2 \hat{A}_r(\kappa) T_2^{-1}$ is in the form (5.11) can be constructed by stacking the local modal transformations t_k as

$$T_2 = \begin{bmatrix} t_1 & & & \\ & t_2 & & \\ & & \ddots & \\ & & & t_k \end{bmatrix} \tag{5.18}$$

where $t_k = 1$ if the system has pure real eigenvalues [89].

Finally, the real modal transformation T_1 and controllability transformation T_2 build up the transformation matrix $T = T_2 T_1$ to express the reduced order system in terms of modal deflections and velocities. Notice that the transformation T depends on the varying parameter ρ. However, this transformation is only used to generate additional outputs and hence, the state consistency of the LPV systems is not affected. With these modal velocities as performance objectives, several controllers are designed using different subsets of actuators or sensors for each flight condition. Then, a comparison between the performance levels and robustness measures achieved by these controllers is used to decide on the appropriate subset of actuators and sensors that effectively stabilize and increase the structural damping of the system. The following subsections present the results for the two selection procedures.

5.3.1   Control surface selection

The FI problem is used for selecting the appropriate set of actuation for the BFF aircraft. The interconnection used to synthesize the FI controllers is depicted in Fig. 5.2. Here, e represents the modal velocity outputs where T_κ is the collection of all local second order

modal transformations across the flight envelope. As expected, the controller K_{FI} takes all the system's states x as feedback measurements. The controller minimizes the RP level from actuation disturbances, d, to modal velocities, e, while maximizing the robustness to model uncertain for each input channel.
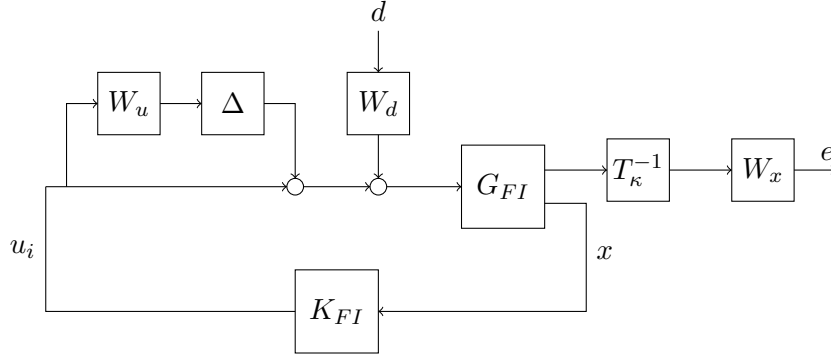
Figure 5.2: Control interconnection for actuator selection

Constant weights, W_d, are used to model the disturbances to each control surface. This weight is selected as $W_d = 0.5$ for all control surfaces. In addition, multiplicative input uncertainty is included to avoid destabilizing unmodeled high-frequency flexible modes outside the control bandwidth. Recall that the available actuator bandwidth corresponds to $125\,\mathrm{rad/s}$. The uncertainty weight represents approximately 40% model error up to $100\,\mathrm{rad/s}$ and as much as 100% uncertainty at $300\,\mathrm{rad/s}$ for each input channel. This uncertainty is described by the weight, $W_u = 500(s+121.4)/(s+1.6\times10^5)$. The uncertainty block Δ is diagonal with $||\Delta_k|| \leq 1$ representing independent variations for each input channel.

On the other hand, the damping of critical modes is enforced by a constant performance weight W_x. The three modal velocities selected as control objectives correspond to symmetric wing bending, symmetric wing torsion and anti-symmetric wing torsion. These modes are critical for the flutter phenomena and hence, a high gain attenuation of $W_x = 8$ is assigned to each of them in order to ensure damping. Once all the weights are defined, the next step is to design FI controllers for several actuation subsets u_i using the interconnection in Fig. 5.2. The RP levels, γ, obtained by each controller, K_{FI}, are plotted as a function of airspeed in Fig. 5.3.

Fig. 5.3 shows that the selection of different control surfaces subset do not have a significant effect in the performance of the aircraft unless only a pair of flaps is used. Furthermore, it is observed that the combination of the Body and Midboard flaps shows
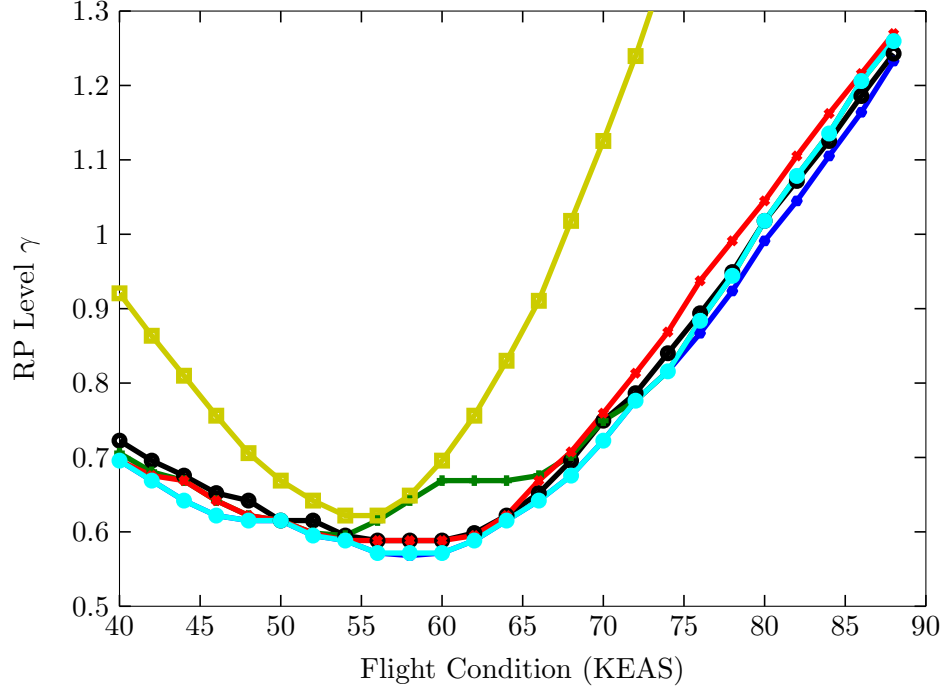
Figure 5.3: Performance level γ variation across the flight envelope for all available flaps (——), inboard+outboard (——), body+midboard (——), body+outboard (——), body+midboard+outboard (——) and only body flaps (——)

a different result between 58 and 66 KEAS. Recall that the aircraft has 1 unstable mode at 58 KEAS, 2 unstable modes at 60 KEAS and 3 unstable modes beyond 62 KEAS. Notice that for all cases the performance starts to rapidly degrade when the aircraft has three unstable modes (62 KEAS). The robustness analysis follows next.

Fig. 5.4 shows the phase disk margins for each of the actuators used in the different subsets for control. A disk margin is the largest region for each channel that, for all simultaneous gain and phase variations inside the region, the nominal closed-loop system is stable. It is observed that the phase margins for the outboard flap are the most affected when the airspeed increases, even if all the available actuators are used. Using only body flaps results in, as expected, small robustness margins when the aircraft has more than one unstable mode. On the other hand, the combination of three flap pairs (body+midboard+outboard) seems to obtain the best phase margins across the flight envelope. Gain margins are sufficiently large for all the combinations across the flight envelope which means that they do not constitute a constraint for actuator selection and thus, plots are not shown.

From this analysis, the conclusion is that the best combination of actuators to achieve
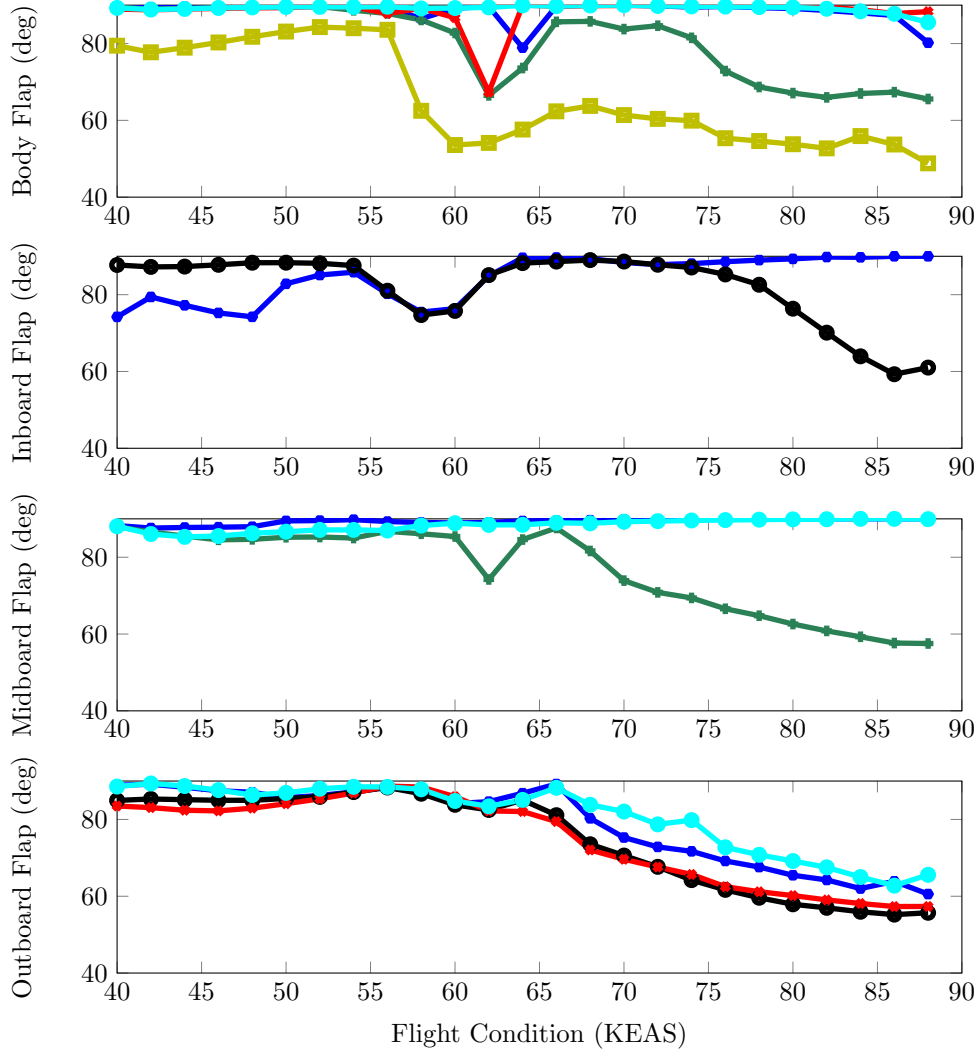
Figure 5.4: Actuators phase disk margins (loop-at-a-time) using all available flaps (——), inboard+outboard (——), body+midboard (——), body+outboard (——), body+midboard+outboard (——) and only body flaps (——)

the desired performance is the body, midboard and outboard flaps. In addition, the best combination of two pairs of surfaces seems to be the set of body and outboard flaps. Fig. 5.5 and Fig. 5.6 show the closed-loop frequency responses at 42 and 72 KEAS for two optimal controllers synthesized using different control effectors. It is observed that the controller synthesized with two pairs of flaps provides almost the same damping to the three flutter that the controller using the three pairs of flaps.
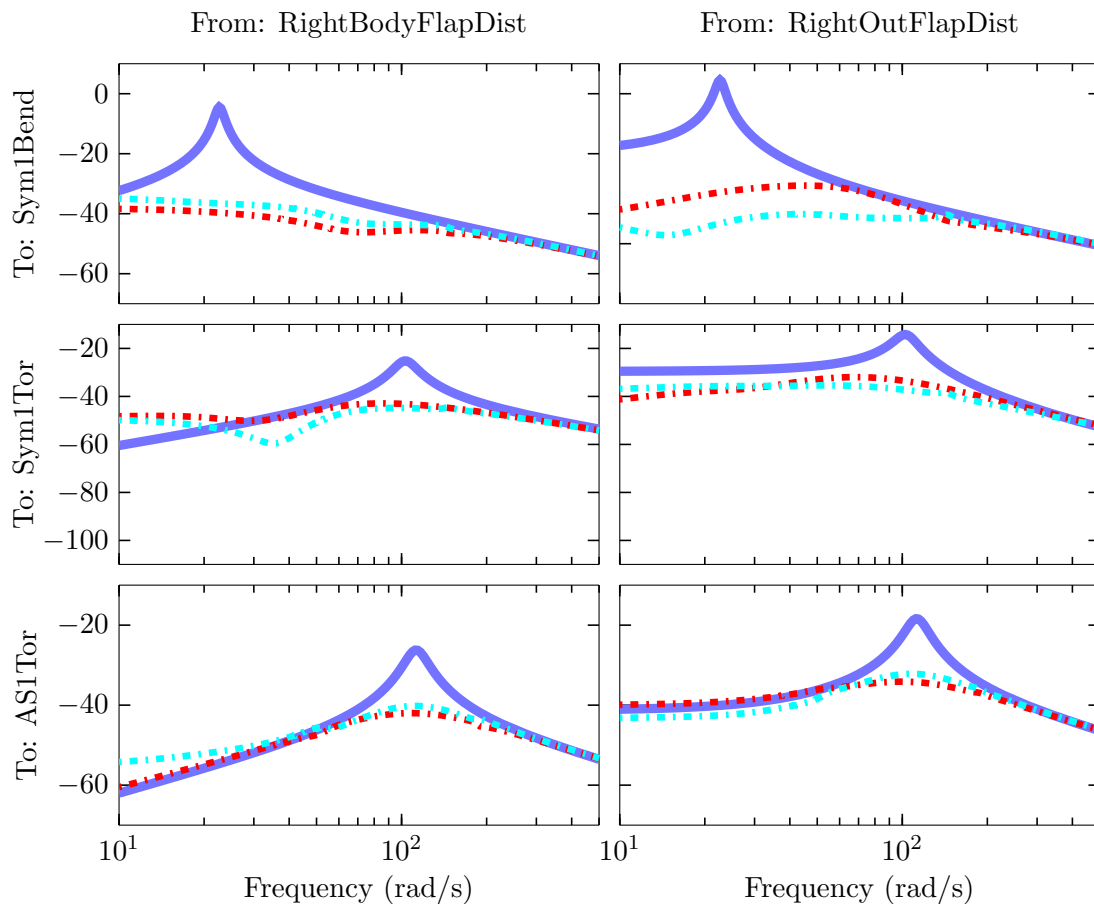
Figure 5.5: Frequency response from disturbances in the body and outboard flaps to the three critical modal velocities for the open-loop system (———), closed-loop system with body+outboard flaps (▪▪▪), and body+midboard+outboard flaps (▪▪▪) at 42 KEAS

5.3.2 Sensor measurement selection

The FC problem is used for selecting the appropriate set of measurements for the BFF aircraft. The interconnection used to synthesize the FC controllers is depicted in Fig. 5.7. Here, d represents the disturbances to modal velocities. As described previously, the controller K_{FC} affects directly all the system states. This controller minimizes the RP level from modal disturbances, d, to output measurements, e, while maximizing the robustness to model uncertainty for each output.

The weights used for design are $W_x = 1$ for the three critical modes and $W_e = 1$ for all measurements. Multiplicative output uncertainty is included to avoid sensitivity to measurement noise outside the control bandwidth. The uncertainty weight, $W_u = 500(s +$
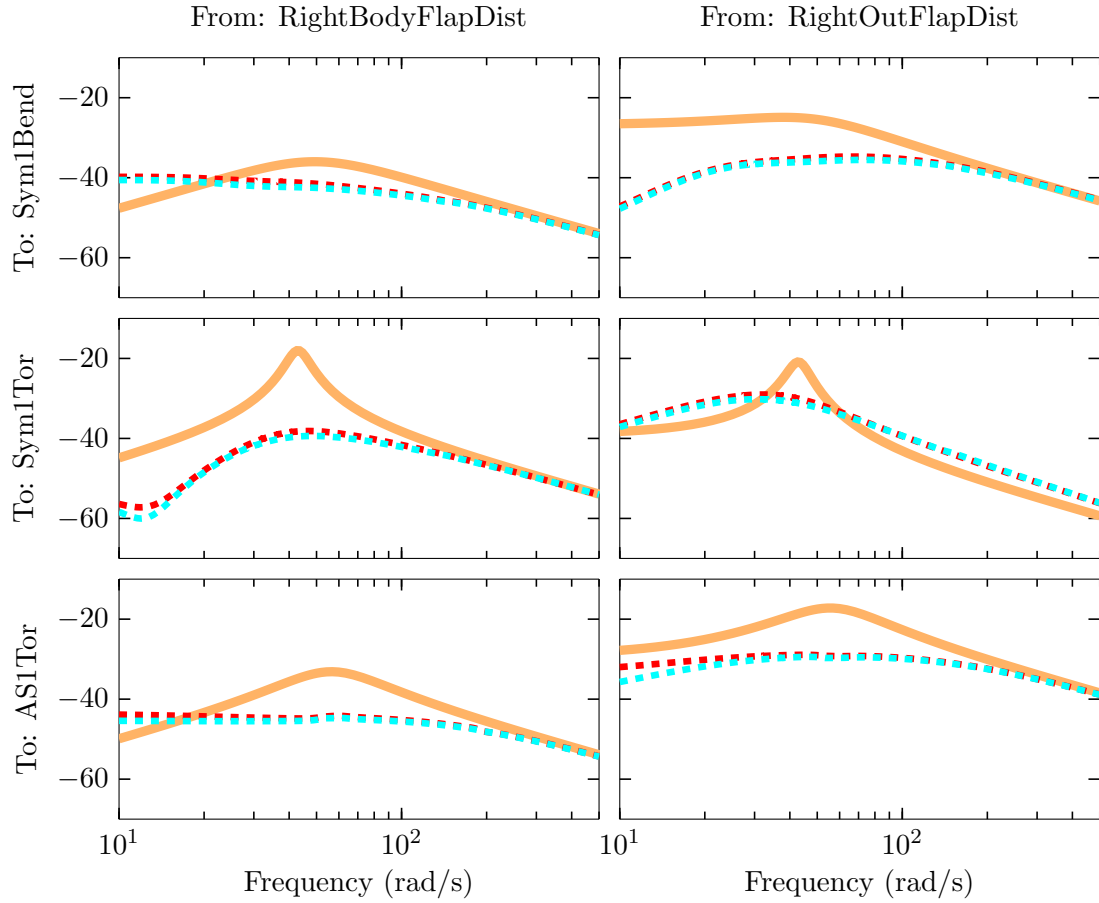
Figure 5.6: Frequency response from disturbances in the body and outboard flaps to the three critical modal velocities for the open-loop system at (———), closed-loop system with body+outboard flaps (▪▪▪), and body+midboard+outboard flaps (▪▪▪) at 72 KEAS
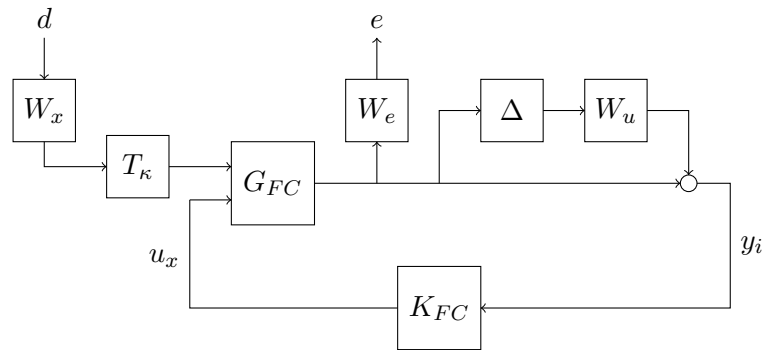
Figure 5.7: Control interconnection for sensor selection

$109.1)/(s+1.4\times10^5)$, represents approximately 40% model error up to 80 rad/s and as much as 100% uncertainty for frequencies higher than 300 rad/s. Here, the diagonal uncertainty block Δ with $||\Delta_k|| \leq 1$ represents the sensor noise variation for each measurement.

Several sensor combinations were tested but only the most relevant results are plotted. Fig. 5.8 shows the variation of RP levels, γ, for six different sets of measurements as a function of airspeed. This plot shows that the system's robust performance is more sensitive to the selection of sensors than to the selection of actuators shown in the previous subsection.
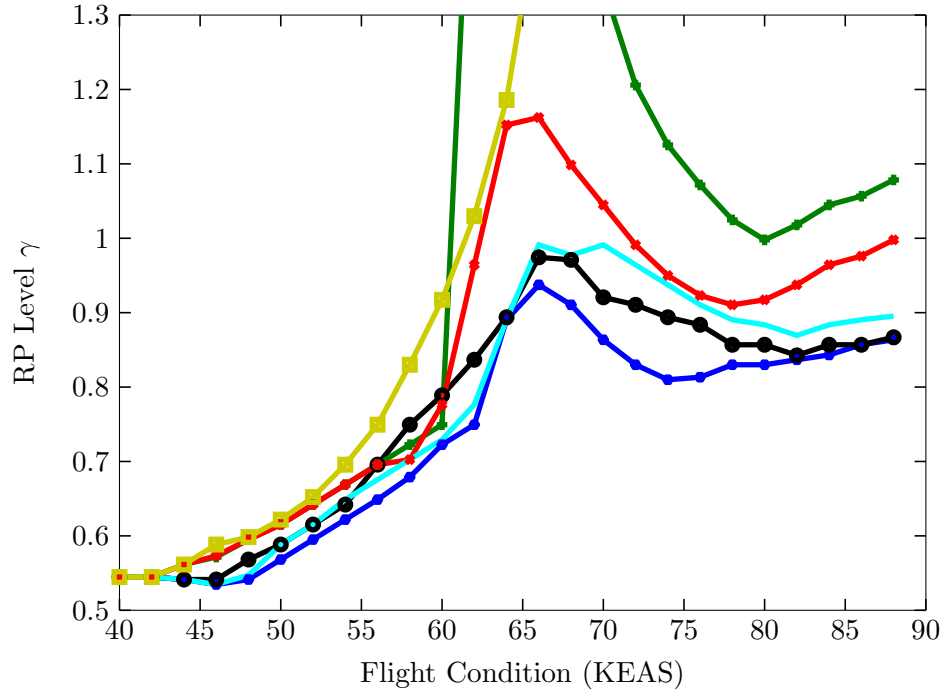
Figure 5.8: Performance level γ variation across the flight envelope for all available sensors (———), 6 accelerometers (———), pitch rate+wing aft accels (———), pitch rate+wing fwd accels (———), pitch rate+fwd accels+LESP (———) and only rate sensors (———)

The best robust performance is given, as expected, by the usage of all available measurements. However, using all the acceleration information in the aircraft, which corresponds to 6 accelerometers distributed between the body and both wings, obtains acceptable robust performance. Notice also that for all cases, the performance is degraded across the flight envelope and it is critical at 66 KEAS. Recall that at this critical speed, the body freedom flutter is close in proximity to the symmetric torsional flutter mode.

In addition, a comparison between the set of sensors corresponding to the pitch rate

together with the wing aft/forward accelerometers is shown in Fig. 5.8. Here, the combination that includes the accelerometers at the leading edge of the wing provides better information to the controller than the accelerometers at the trailing edge. It is also noticed that the performance for the leading edge set, compared to the set with 6 accelerometers, is degraded for flight conditions starting at 74 KEAS. In this case, the body freedom flutter is close in proximity to the anti-symmetric torsional flutter mode. This means that acceleration information from both leading and trailing edge is required to successfully damp out the anti-symmetric mode. Moreover, using the LESP sensors together with the pitch rate and leading edge accelerometers can improve the performance at high speeds. Lastly, it is observed that the performance is significantly degraded starting at 58 KEAS if only the vehicle rates are used for feedback. At this critical speed, the aircraft is in transition to have two flutter modes.

Fig. 5.9 and Fig. 5.10 compare the modal damping in the closed-loop system for two sensor combinations at 42 and 72 KEAS. The plots show, as expected, that the FC controller synthesized with all available sensors can provide more damping to the critical flutter modes than the combination with the 6 accelerometers. Notice that the controller is not able to add damping to the symmetric torsion mode. Penalizing this mode with a higher weight W_d will increase damping, however the robustness of the system will be significantly degraded. This means that the available sensor information is not able to capture the dynamics of all three critical modes. Next, the robustness analysis comparing the phase disk margins for each measurement is presented. Gain margins, as in the actuator selection case, are sufficiently large for all the combinations and hence, are not plotted.

Fig. 5.11 and Fig. 5.12 plot the phase disk margins obtained for each sensor combination across the flight envelope. Both plots show that using all the available sensors for control is not always the best case scenario for robustness. This means that maximizing the robustness of more channels while achieving the desired performance is harder than if less sensors are used. Furthermore, it is observed that the controller using the 6 accelerometers for feedback, achieves good phase margins and in cases like the wing accelerometers in the trailing edge are better than the margins provided when all available sensors are used. From this analysis, the conclusion is that the suitable combination of sensors for control feedback of the BFF vehicle, given the desired performance and robustness, corresponds to the 6 accelerometers available in the aircraft.
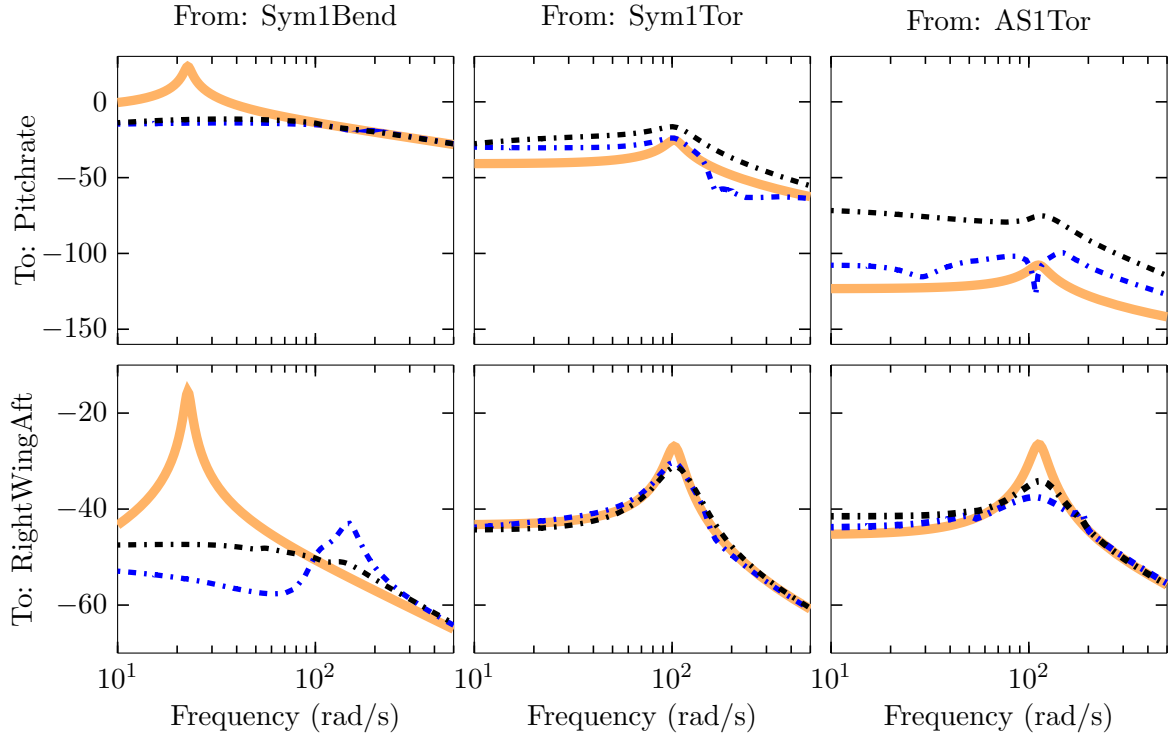
Figure 5.9: Frequency response from the three modal velocity disturbances to the pitch rate and accelerometer in the wing trailing edge for the open-loop system (━━), closed-loop system with all sensors available (·—·—·), and only accelerometers (·—·—·) at 42 KEAS

5.4   Summary

This chapter described an approach for selection of actuators and sensors for aeroservoelastic systems. The approach is based on special cases of robust control synthesis when the system has access to all the states information and actuation. These cases, called FI and FC problems, provide a globally optimal controller that allows a fair comparison between the performance achieved by different sensor/actuator combinations.

The proposed actuator/sensor selection method was applied to the experimental Body Freedom Flutter aircraft that has three flutter modes occurring across the flight envelope. The desired performance is determined to stabilize the aircraft and add sufficient damping to the three critical flutter modes. From this analysis it is concluded that the most suitable subset of control surfaces corresponds to the body and outboard flaps. Following, the most suitable subset of sensor measurements for feedback corresponds to the combination with the 6 accelerometers available in the aircraft wings and center body. These actuator
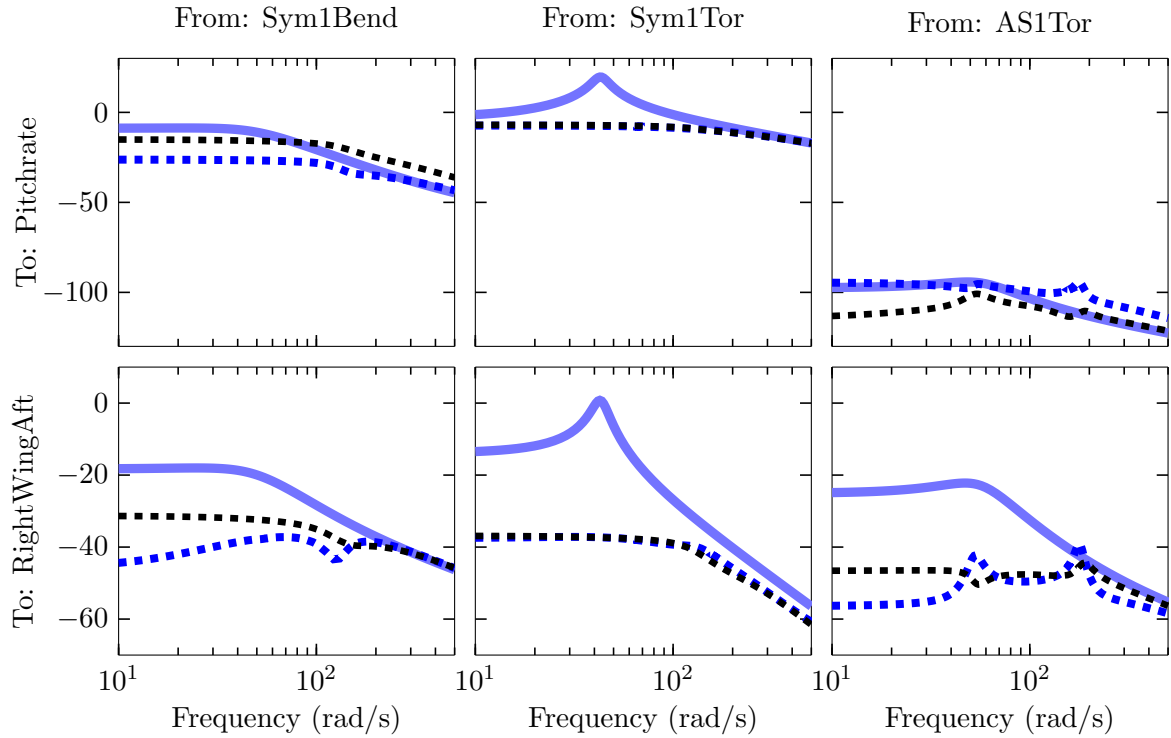
Figure 5.10: Frequency response from the three modal velocity disturbances to the pitch rate and accelerometer in the wing trailing edge for the open-loop system (▬▬), closed-loop system with all sensors available (••••), and only accelerometers (••••) at 72 KEAS

and sensor selection results will then be used to design output feedback controllers. The following chapter presents the results for these designs. Notice here that the performance obtained by the output feedback controllers can only be expected to be worse than the performance levels reported for the FI and FC special cases.
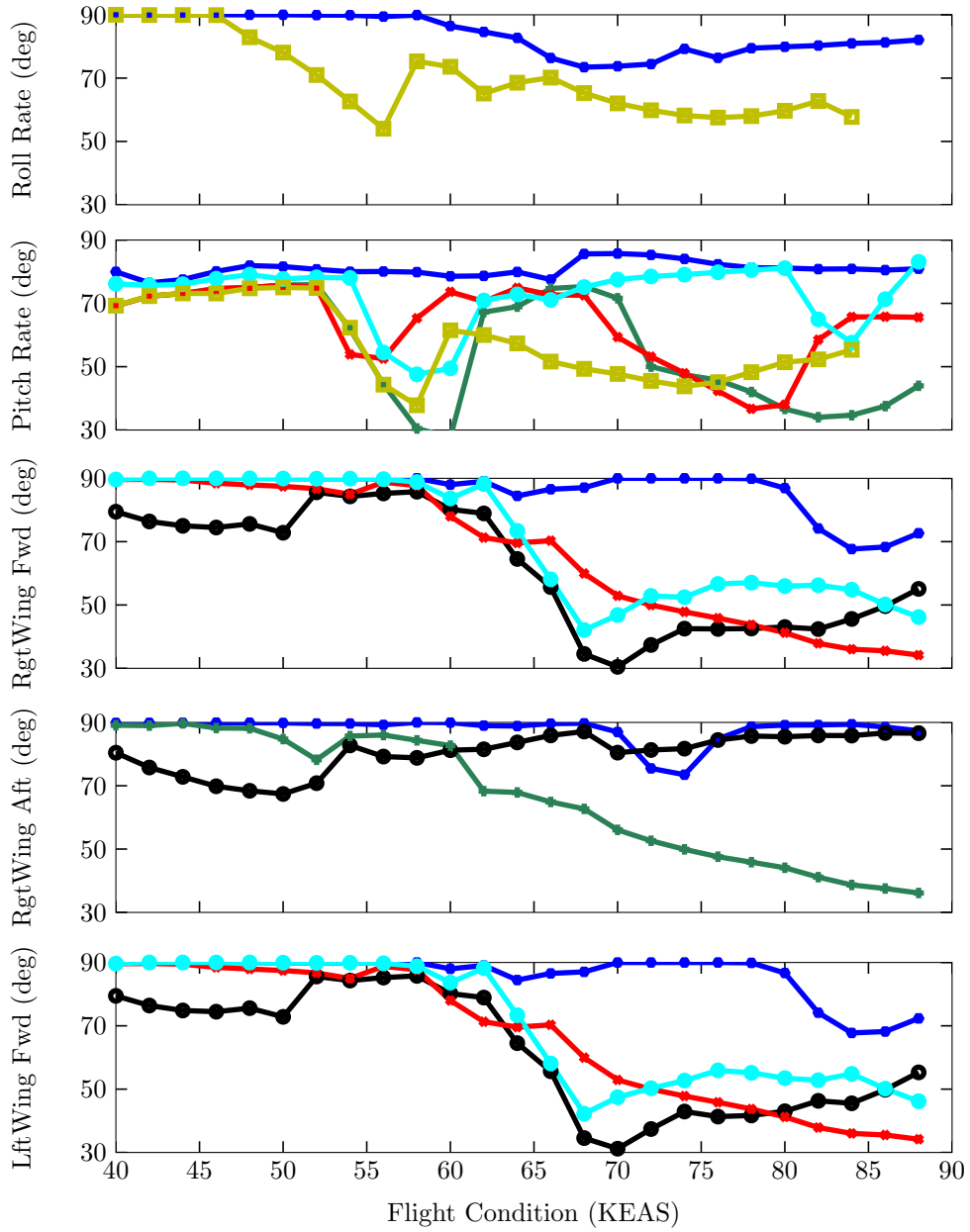
Figure 5.11: Rates and wing accelerometers phase disk margins (loop-at-a-time) using all available sensors (━●━), 6 accelerometers (━●━), pitch rate+wing aft accels (━+━), pitch rate+wing fwd accels (━✱━), pitch rate+fwd accels+LESP (━━) and only rate sensors (━■━) for control
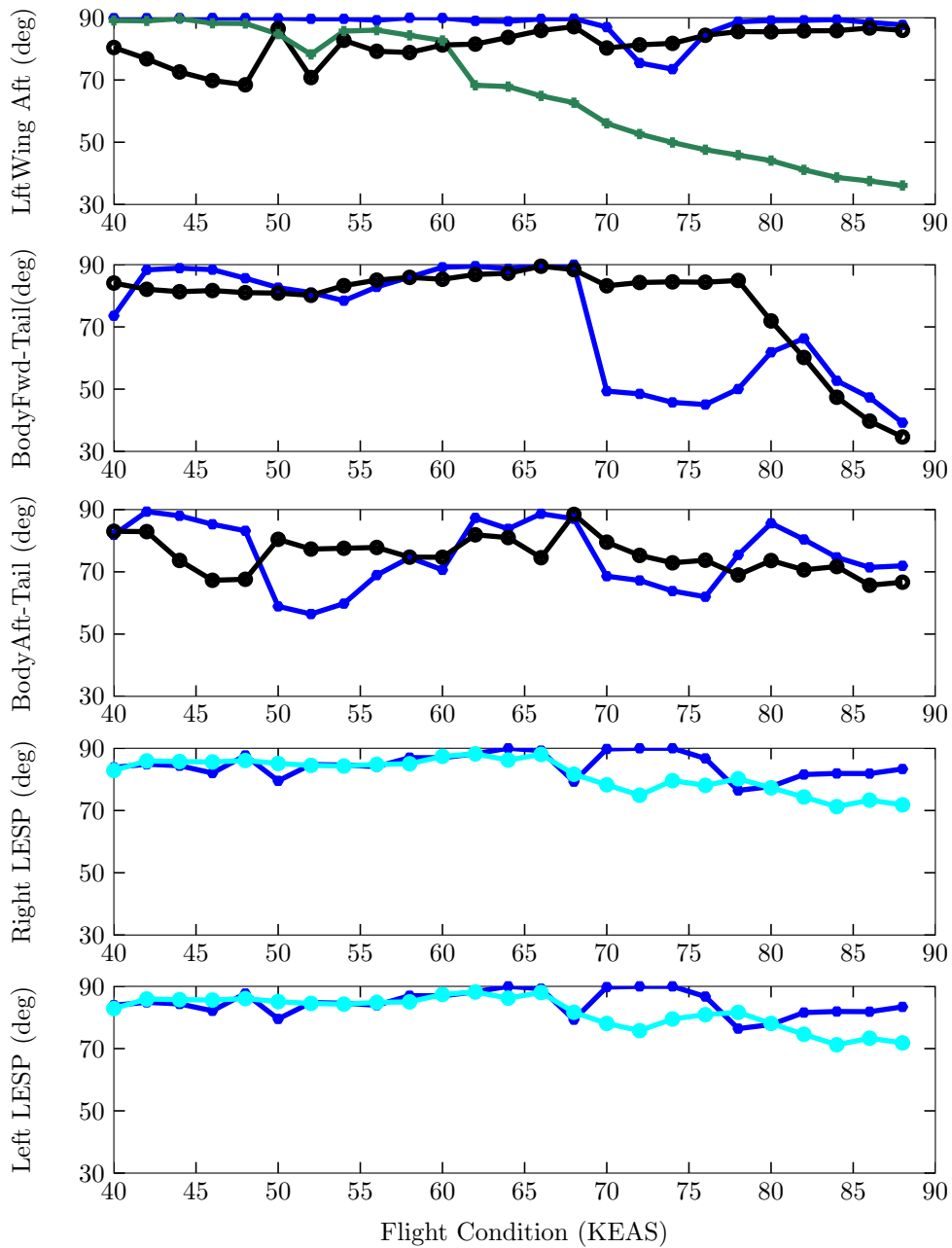
Figure 5.12: Body accelerometers and LESP phase disk margins (loop-at-a-time) using all available sensors (━●━), 6 accelerometers (━●━), pitch rate+wing aft accels (━●━), pitch rate+wing fwd accels (━●━), pitch rate+fwd accels+LESP (━━) and only rate sensors (━■━) for control

Chapter 6

Robust Control Synthesis for Aeroservoelastic Systems

The design of multivariable feedback controllers for aerospace systems is often based on the interpolation of linear controllers at various operation points. This procedure is known as gain-scheduling control. One advantage of gain-scheduling control is the potential to incorporate linear robust control methodologies into non-linear control design. However, traditional gain-scheduling methods are still an ad hoc procedure that do not guarantee the robustness, performance or stability of the system for rapid changes in the scheduling variables [11, 30, 91]. These drawbacks were the main motivation to develop multivariable gain-scheduled control techniques based on the linear, parameter-varying (LPV) description of non-linear systems. The advantage of LPV techniques is that they allow the performance, robustness, and stability limitations to be incorporated in a unified framework. These control techniques are described in Section 6.1.

Aeroservoelastic (ASE) systems can be modeled in the LPV framework as described in Chapter 2. In particular, this chapter refers to the design of multivariable robust controllers for the body freedom flutter (BFF) aircraft, where the scheduling parameter for the controllers corresponds to airspeed. Section 6.2 presents the design of linear, time-invariant (LTI) robust controllers for the BFF aircraft at individual flight conditions. The point design formulation for these controllers is the base for the synthesis of an LPV controller that guarantees the stabilization and robust performance of the aircraft. Lastly, Section 6.3 presents the results of an LPV controller and compares the robust performance achieved with respect to the LTI controllers designed at individual flight conditions.

6.1 LPV Controller Synthesis

The method for LPV controller synthesis presented in this section is a generalized version of the standard $\mathcal{H}_\infty$ problem. This synthesis problem is depicted in Fig. 6.1. Here, G_ρ represents an LPV system and K_ρ represents an LPV controller. The performance objectives are collected in e and the disturbances are collected in d. In addition, the controller is provided with measurements, y, and generates control inputs, u.
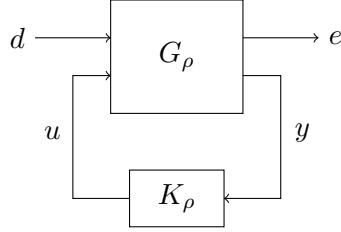
Figure 6.1: LPV control configuration

Recall from Chapter 2 that the LPV system G_ρ has the form

$$\begin{aligned}
\dot{x} &= A(\rho)x + B(\rho)d \\
e &= C(\rho)x + D(\rho)d
\end{aligned} \tag{6.1}$$

where the set of admissible trajectories is defined as

$$\mathcal{A} := \left\{ \rho : \mathbb{R}^+ \to \mathbb{R}^{n_\rho} : \rho(t) \in \mathcal{P}, \dot{\rho}(t) \in \dot{\mathcal{P}} \ \forall t \geq 0 \right\} \tag{6.2}$$

and the parameter rates of variation are assumed to lie in

$$\dot{\mathcal{P}} := \{ \dot{\rho} \in \mathbb{R}^{n_\rho} \mid |\dot{\rho}_i| \leq \nu_i, i = 1, \ldots, n_\rho \} \tag{6.3}$$

Now, the robust control objective in Fig. 6.1 is to find a controller K_ρ such that the resultant closed-loop system is exponentially stable and the induced $\mathcal{L}_2$-norm from d to e is less than γ. This problem is commonly known as the quadratic LPV γ-performance problem [92]. Formal definitions and assumptions for the solution of this synthesis problem follow.

The quadratic LPV γ-performance problem is written as

$$\begin{aligned}
&\min_{K_\rho} \gamma \ \text{s.t} \ \forall(\rho, \dot{\rho}) \\
&\quad \| F_L(G_\rho, K_\rho) \|_{\mathcal{L}_2 \to \mathcal{L}_2} < \gamma \\
&\quad F_L(G_\rho, K_\rho) \ \text{is exponentially stable}
\end{aligned} \tag{6.4}$$

where the linear fractional transformation $F_L(G_\rho, K_\rho)$ denotes the closed-loop system, $\|\cdot\|_{\mathcal{L}_2 \to \mathcal{L}_2}$ denotes the induced $\mathcal{L}_2$-norm of the system, and γ denotes the robust performance (RP) level achieved by the controller. Here, the induced $\mathcal{L}_2$-norm is defined as

$$\|F_L(G_\rho, K_\rho)\|_{\mathcal{L}_2 \to \mathcal{L}_2} = \sup_{\rho \in \mathcal{A}} \sup_{d \neq 0, d \in \mathcal{L}_2} \frac{\|e\|_2}{\|d\|_2} \tag{6.5}$$

where $\|\cdot\|_2$ represents the signal $\mathcal{L}_2$-norm, i.e. $\|d\|_2 = \left(\int_0^\infty d^T d \ dt\right)^{1/2}$. Following, the mathematical performance conditions in (6.4) are presented.

The general open-loop LPV system G_ρ is transformed under mild assumptions on $D(\rho)$ into the form [93]

$$\begin{bmatrix} \dot{x} \\ e_1 \\ e_2 \\ y \end{bmatrix} = \begin{bmatrix} A(\rho) & B_{11}(\rho) & B_{12}(\rho) & B_2(\rho) \\ C_{11}(\rho) & D_{1111}(\rho) & D_{1112}(\rho) & 0 \\ C_{12}(\rho) & D_{1121}(\rho) & D_{1122}(\rho) & I_{n_{e_2}} \\ C_2(\rho) & 0 & I_{n_{d_2}} & 0 \end{bmatrix} \begin{bmatrix} x \\ d_1 \\ d_2 \\ u \end{bmatrix} \tag{6.6}$$

where $\rho \in \mathcal{A}$, $x \in \mathbb{R}^n$, $e_1 \in \mathbb{R}^{p_1}$, $e_2 \in \mathbb{R}^{p_2}$, $y \in \mathbb{R}^{n_y}$, $d_1 \in \mathbb{R}^{m_1}$, $d_2 \in \mathbb{R}^{m_2}$, and $u \in \mathbb{R}^{n_u}$. Similarly, the controller K_ρ is defined as

$$\begin{bmatrix} \dot{x}_K \\ u \end{bmatrix} = \begin{bmatrix} A_K(\rho, \dot{\rho}) & B_K(\rho, \dot{\rho}) \\ C_K(\rho, \dot{\rho}) & D_K(\rho, \dot{\rho}) \end{bmatrix} \begin{bmatrix} x_K \\ y \end{bmatrix} \tag{6.7}$$

where $x_K \in \mathbb{R}^{n_K}$ denotes the controller states and $\dot{\rho} \in \dot{\mathcal{P}}$ denotes the parameter variation rates. With these, the closed-loop LPV system $F_L(G_\rho, K_\rho)$ yields the state-space representation

$$\begin{bmatrix} \dot{x}_{cl} \\ e \end{bmatrix} = \begin{bmatrix} A_{cl}(\rho, \dot{\rho}) & B_{cl}(\rho, \dot{\rho}) \\ C_{cl}(\rho, \dot{\rho}) & D_{cl}(\rho, \dot{\rho}) \end{bmatrix} \begin{bmatrix} x_{cl} \\ d \end{bmatrix} \tag{6.8}$$

Here, $x_{cl}^T = \begin{bmatrix} x^T & x_K^T \end{bmatrix}$, $e^T = \begin{bmatrix} e_1^T & e_2^T \end{bmatrix}$, $d^T = \begin{bmatrix} d_1^T & d_2^T \end{bmatrix}$, and

$$A_{cl}(\rho, \dot{\rho}) = \begin{bmatrix} A(\rho) + B_2(\rho)D_K(\rho, \dot{\rho})C_2(\rho) & B_2(\rho)C_K(\rho, \dot{\rho}) \\ B_K(\rho, \dot{\rho})C_2(\rho) & A_K(\rho, \dot{\rho}) \end{bmatrix} \tag{6.9}$$

$$B_{cl}(\rho, \dot{\rho}) = \begin{bmatrix} B_{11}(\rho) & B_{12}(\rho)D_K(\rho, \dot{\rho}) \\ 0 & B_K(\rho, \dot{\rho}) \end{bmatrix} \tag{6.10}$$

$$C_{cl}(\rho, \dot{\rho}) = \begin{bmatrix} C_{11}(\rho) & 0 \\ C_{12}(\rho) + D_K(\rho, \dot{\rho})C_2(\rho) & C_K(\rho, \dot{\rho}) \end{bmatrix} \tag{6.11}$$

$$D_{cl}(\rho, \dot{\rho}) = \begin{bmatrix} D_{1111}(\rho) & D_{1112}(\rho) \\ D_{1121}(\rho) & D_{1122}(\rho)D_K(\rho, \dot{\rho}) \end{bmatrix} \tag{6.12}$$

Now, the $\mathcal{L}_2$-norm and stability conditions of $F_L(G_\rho, K_\rho)$ in (6.4) can be transferred into a linear matrix inequality described in the following lemma.

Lemma 6.1.1 *The LPV system $F_L(G_\rho, K_\rho)$ is exponentially stable with $\|F_L(G_\rho, K_\rho)\|_{\mathcal{L}_2 \to \mathcal{L}_2} < \gamma$, if there exists a continuously differentiable matrix function $W : \mathbb{R}^{n_\rho} \to \mathbb{R}^{(n+n_K) \times (n_K+n)}$, $W(\rho) = W(\rho)^T > 0$ and continuous bounded matrix functions $A_K : \mathbb{R}^{n_\rho} \times \mathbb{R}^{n_\rho} \to \mathbb{R}^{n_K \times n_K}$, $B_K : \mathbb{R}^{n_\rho} \times \mathbb{R}^{n_\rho} \to \mathbb{R}^{n_K \times n_y}$, $C_K : \mathbb{R}^{n_\rho} \times \mathbb{R}^{n_\rho} \to \mathbb{R}^{n_u \times n_K}$, and $D_K : \mathbb{R}^{n_\rho} \times \mathbb{R}^{n_\rho} \to \mathbb{R}^{n_u \times n_y}$ such that [93]*

$$\begin{bmatrix} A_{cl}^T(\rho, \dot\rho)W(\rho) + W(\rho)A_{cl}^T(\rho, \dot\rho) + \sum_{i=1}^{s} \dot\rho_i \frac{\partial W}{\partial \rho_i} & W(\rho)B_{cl}(\rho, \dot\rho) & \gamma^{-1}C_{cl}^T(\rho, \dot\rho) \\ B_{cl}^T(\rho, \dot\rho)W(\rho) & -I_{n_d} & \gamma^{-1}D_{cl}^T(\rho, \dot\rho) \\ \gamma^{-1}C_{cl}(\rho, \dot\rho) & \gamma^{-1}D_{cl}(\rho, \dot\rho) & -I_{n_e} \end{bmatrix} < 0 \tag{6.13}$$

for all $\rho \in \mathcal{A}$ and $|\dot\rho_i| \leq \nu_i$, $i = 1, \cdots, n_\rho$.

This synthesis problem can be solved numerically when expressed as the feasibility of a set of affine matrix inequalities. The following theorem presents the main results for the existence of an LPV controller that solves Lemma 6.1.1.

Theorem 6.1.2 *The quadratic LPV γ-performance problem in (6.4) is solvable if there exist continuously differentiable matrix functions $X : \mathbb{R}^{n_\rho} \to \mathbb{R}^{n \times n}$ and $Y : \mathbb{R}^{n_\rho} \to \mathbb{R}^{n \times n}$ such that for all $\rho \in \mathcal{A}$, $X(\rho), Y(\rho) > 0$, and [93]*

$$\begin{bmatrix} X(\rho)\check{A}_X^T(\rho) + \check{A}_X(\rho)X(\rho) - \sum_{i=1}^{s} \pm \left(\nu_i \frac{\partial X}{\partial \rho_i}\right) - B_2(\rho)B_2^T(\rho) & X(\rho)C_{11}^T(\rho) & \gamma^{-1}\check{B}_X(\rho) \\ C_{11}(\rho)X(\rho) & -I_{n_{e_1}} & \gamma^{-1}D_{111\cdot}(\rho) \\ \gamma^{-1}\check{B}_X^T(\rho) & \gamma^{-1}D_{111\cdot}^T(\rho) & -I_{n_d} \end{bmatrix} < 0 \tag{6.14}$$

$$\begin{bmatrix} \check{A}_Y^T(\rho)Y(\rho) + Y(\rho)\check{A}_Y(\rho) + \sum_{i=1}^{s} \pm \left(\nu_i \frac{\partial Y}{\partial \rho_i}\right) - C_2(\rho)^T C_2(\rho) & Y(\rho)B_{11}(\rho) & \gamma^{-1}\check{C}_Y^T(\rho) \\ B_{11}^T(\rho)Y(\rho) & -I_{n_{d_1}} & \gamma^{-1}D_{11\cdot 1}^T(\rho) \\ \gamma^{-1}\check{C}_X(\rho) & \gamma^{-1}D_{11\cdot 1}(\rho) & -I_{n_e} \end{bmatrix} < 0 \tag{6.15}$$

$$\begin{bmatrix} X(\rho) & \gamma^{-1}I_n \\ \gamma^{-1}I_n & Y(\rho) \end{bmatrix} \geq 0 \tag{6.16}$$

where

$$D_{111\cdot(\rho)} = [D_{1111}(\rho), \ D_{1112}(\rho)], \qquad D_{112\cdot(\rho)} = [D_{1121}(\rho), \ D_{1122}(\rho)],$$

$$D_{11\cdot 1(\rho)} = \begin{bmatrix} D_{1111}(\rho) \\ D_{1121}(\rho) \end{bmatrix}, \qquad D_{11\cdot 2(\rho)} = \begin{bmatrix} D_{1112}(\rho) \\ D_{1122}(\rho) \end{bmatrix},$$

95

and

$$\check{A}_X(\rho) = A(\rho) - B_2(\rho)C_{12}(\rho), \qquad \check{B}_X(\rho) = B_1(\rho) - B_2(\rho)D_{112\cdot}(\rho),$$
$$\check{A}_Y(\rho) = A(\rho) - B_{12}(\rho)C_2(\rho), \qquad \check{C}_Y(\rho) = C_1(\rho) - D_{11\cdot2}(\rho)C_2(\rho),$$

The controller K_ρ is constructed with the feasible solutions for $X(\rho)$, $Y(\rho)$ and γ. Implementation of the feasibility problem in Theorem 6.1.2 requires the parametrization of $X(\rho)$ and $Y(\rho)$ with some pre-selected basis functions. Details about the controller construction and implementation of the synthesis algorithm can be found in [93]. This dissertation uses the synthesis algorithm developed in the Matlab LPVTools [94].

6.2   Output Feedback $\mathcal{H}_\infty$ Controllers

This section presents the point design (i.e., fixed ρ) of $\mathcal{H}_\infty$ controllers for the BFF vehicle. The control objectives are to suppress the unstable flutter interactions observed at 44, 60, and 62 KEAS and to increase the structural damping of the vehicle. These modes vary between 20 and 70 rad/s and consist of the first symmetric wing bending, anti-symmetric wing bending, symmetric wing torsional, and anti-symmetric wing torsional modes. The performance measure is to minimize the maximum frequency response of the four flexible modes against input disturbances.

As described in Chapter 5, the structural damping of the aircraft is achieved by reducing the vibration energy from the modal velocities. This specification is formulated as minimizing the $\mathcal{H}_\infty$-norm between the input disturbances and the modal velocities. Here, the set of actuators and sensors chosen to achieve this desired performance correspond to the body and outboard flaps together with the acceleration measurements in the aircraft wings and center body. This control problem formulation is shown in Fig. 6.2.

The block diagram in Fig. 6.2 shows a weighted control interconnection with multiple performance specifications. These performance specifications are in the form of closed-loop transfer functions which are to be made small through feedback. The mathematical objective is to make the $\mathcal{H}_\infty$-norm of the multiple-input, multiple-output closed-loop transfer function, γ, less than 1. This means that the weighting functions express the demand on disturbance rejection, damping augmentation, robustness, and control usage of the system. Hence, the design task is to find the appropriate tuning weights that meet the aircraft performance objectives.

The weighting functions in the control interconnection are related to the closed-loop
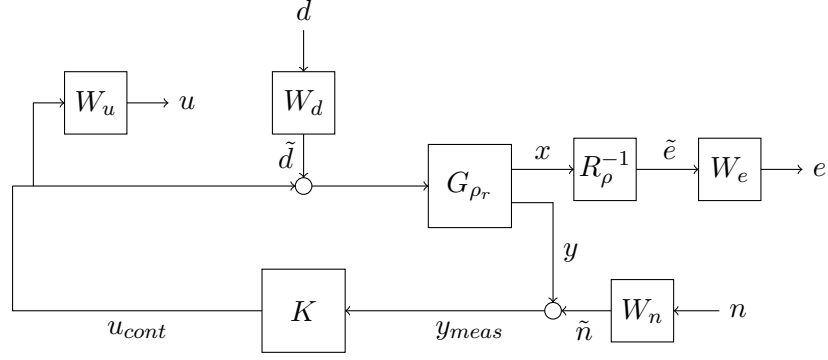
Figure 6.2: Control interconnection for $\mathcal{H}_\infty$ output feedback design

transfer functions of the aircraft as

$$
\begin{bmatrix} e \\ u \end{bmatrix} = \begin{bmatrix} W_e R_\rho^{-1} G_x S_I W_d & W_e G_x S_I K W_n \\ W_u T_I W_d & W_u S_I K W_n \end{bmatrix} \begin{bmatrix} d \\ n \end{bmatrix}
\tag{6.17}
$$

where $S_I = (I - KG_y)^{-1}$ is the input sensitivity transfer function and $T_I = KG_y(I - KG_y)^{-1}$ is the complementary input sensitivity transfer function. Here, G_y represents the vehicle dynamics with sensor measurement outputs and K the controller to be synthesized. Similarly, G_x corresponds the full information vehicle dynamics with the states as outputs, and R_ρ corresponds to the modal velocities transformation. In addition, W_e and W_u represent the performance weights and W_d and W_n represent the input scalings. The selection of these weights is explained following.

The performance weight for vibration attenuation, W_e, is selected as a constant scaling on the modal velocity outputs. This constant weighting shapes the closed-loop transfer function to be flat across frequency. Because the four flexible modes between 20 and 100 rad/s are isolated from the output response, a constant scaling provides a good performance objective without adding additional states to the control problem. The constant weightings are chosen to penalize the open-loop modes across the flight envelope. This diagonal constant weighting is selected to be $W_e = \mathrm{diag}(10, 10, 15, 18)$ which correspond to the first symmetric wing bending, anti-symmetric wing bending, symmetric wing torsional, and anti-symmetric wing torsional modes, respectively.

In addition, constant weights W_d are used to adjust the importance of input disturbances. These weights are selected as $W_d = 0.4$ for all four control surfaces. Notice that the closed-loop transfer function from disturbances, d, to modal velocities, e, is shaped by these two weights W_e and W_d. This closed-loop performance objective expresses the demands

97

in damping and disturbance rejection of the aircraft as compared with their open-loop response. Fig. 6.3 shows the open-loop frequency response magnitude from the disturbances $\tilde{d}$ to the modal velocities $\tilde{e}$ compared with the desired shaped closed-loop transfer function. As mentioned before, this transfer function depends on the weighting functions. In this case, the desired closed-loop behavior against disturbances is given by W_e^{-1} and W_d^{-1}. Observe that the three flutter modes change dramatically across the flight envelope. This behavior will be the main challenge in the design of scheduling controllers.

In addition, the control signal usage is penalized by the weight W_u. The performance objective is to limit the control action while avoiding unmodeled high-frequency modes that could destabilize the system. This objective is achieved by setting W_u as a high-pass filter. Particularly, the body flaps are penalized by the first order filter $1000\frac{s+330.36}{s+3.67\times10^5}$ which corresponds to control roll-off at $160\,\mathrm{rad/s}$. Recall that the flutter modes vary from 10-160 rad/s. Similarly, the outboard flaps are penalized by $1000\frac{s+123.88}{s+1.38\times10^5}$ which corresponds to control roll-off at $60\,\mathrm{rad/s}$. Here, the sensitivity to disturbances observed in Chapter 5 is the motivation to impose a lower bandwidth in the outboard flaps.

The sensor noise level for the accelerometers is also included as a performance limitation in the problem formulation. The weighting function W_n is selected to be 0.05 for all sensors and represents an accelerometer signal to noise ratio of 20. Here, the closed-loop transfer function from noise disturbances, n, to control signals, u, is shaped by the weighting functions W_n and W_u. Fig. 6.4 shows the desired closed-loop transfer function defined by W_u^{-1} and W_n^{-1}. Notice that these weights are limiting the control bandwidth and energy used.

$\mathcal{H}_\infty$ controllers are synthesized at each flight condition based on the block diagram in Fig. 6.2. The weighting functions described previously remain unchanged with airspeed. This means that the same control objectives are expected for all flight conditions and hence, the controllers can be directly compared. Fig. 6.5 plots the performance level achieved for each controller across the flight envelope. Here, the desired performance is achieved if the $\mathcal{H}_\infty$-norm of the closed-loop system in (6.17) is $\gamma < 1$. Notice that only part of the flight envelope, from 50 to $68\,\mathrm{KEAS}$, achieves the specified performance by the weighting functions.

Fig. 6.6 shows the maximum singular values plot of the open loop gain of the system for all flight conditions. As expected, the largest loop gains are provided in the frequency range of the flutter modes. In addition, it is observed that a higher control bandwidth is required at high velocities to achieve the desired performance. This control bandwidth is the result of the limitations imposed by the instabilities of the aircraft at high airspeed. More details about these limiting conditions will be given in later sections. Fig. 6.7 shows
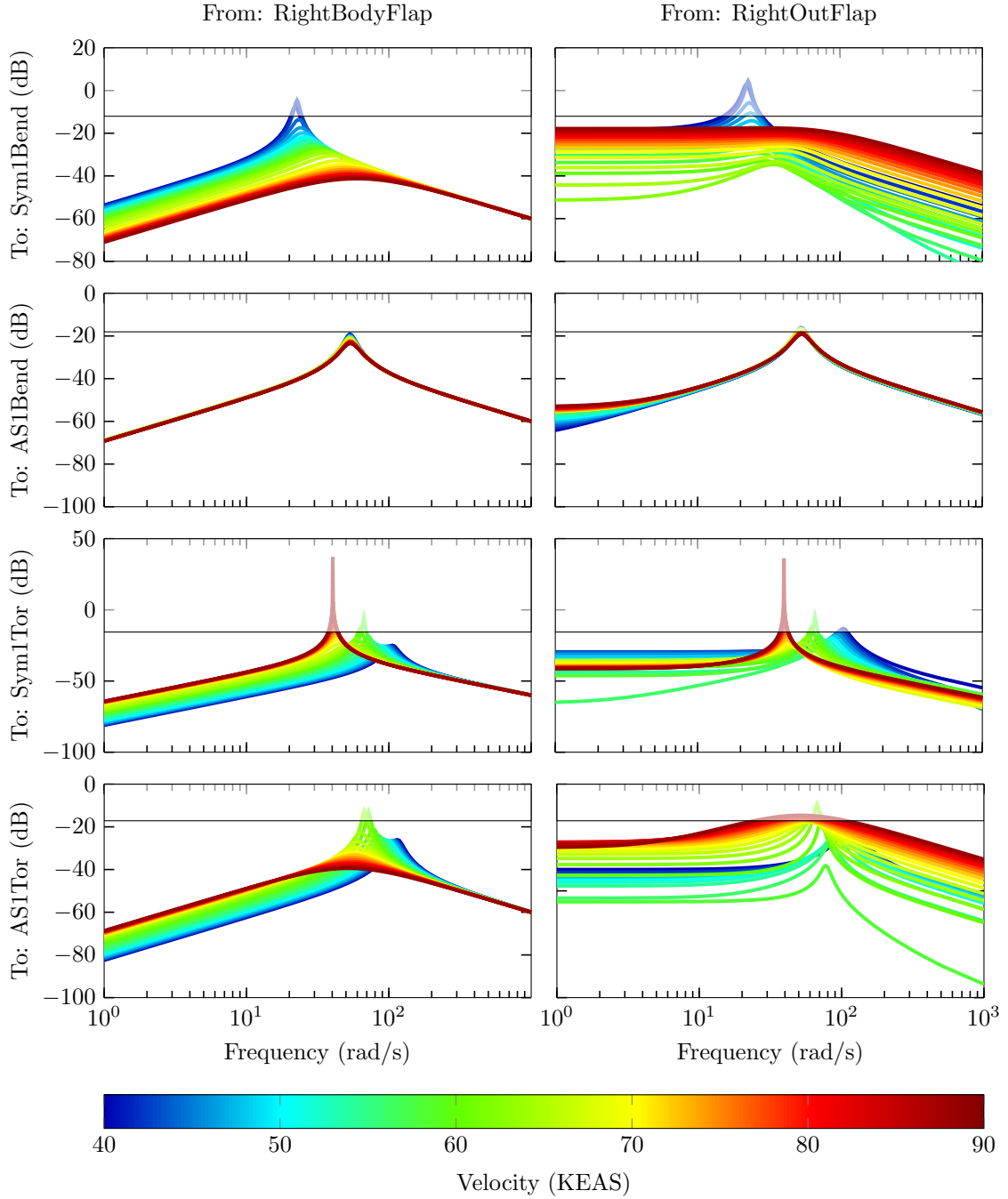
Figure 6.3: Frequency response magnitude of the open-loop transfer function from input disturbances, $\tilde{d}$, at right body flap and right outboard flap to modal velocities, $\tilde{e}$. Lighter areas correspond to undesired closed-loop magnitudes limited by W_e^{-1} and W_d^{-1}
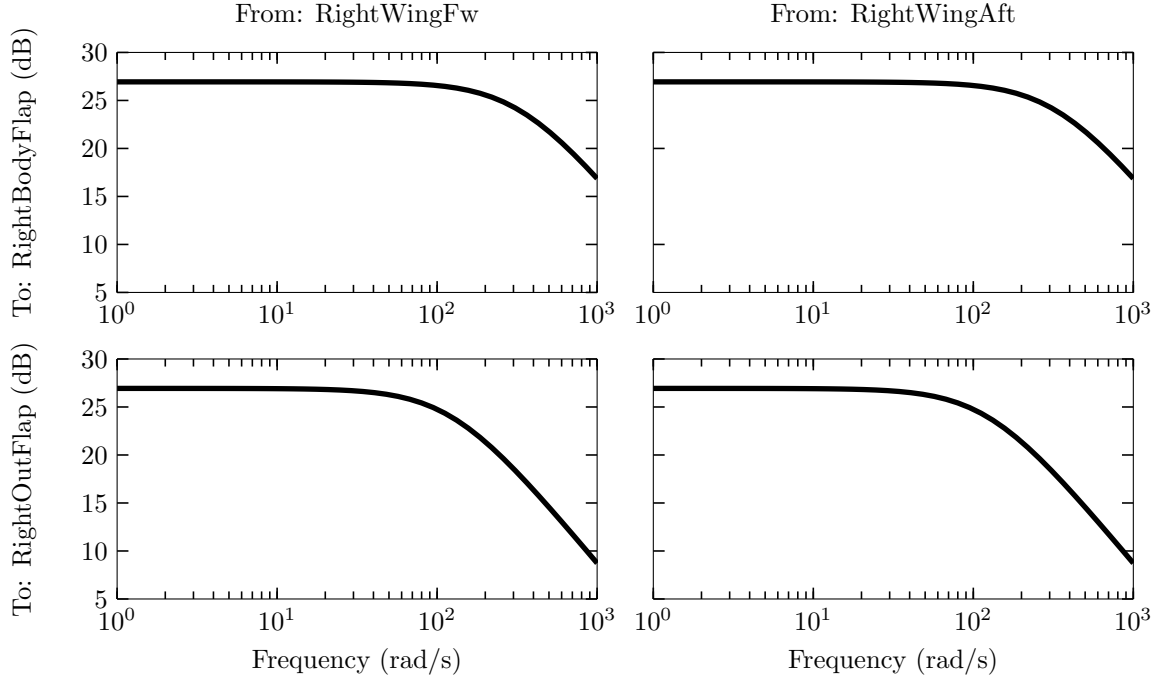
Figure 6.4: Frequency response magnitude of the desired closed-loop transfer function from noise disturbances, $\tilde{n}$, to control signals, u_{cont}, defined by W_u^{-1} and W_n^{-1}

the transfer functions from disturbances in the body and outboard flaps to the four modal velocities objectives. Observe that all controllers provide damping to the four critical modes in comparison to the open loop system. Following, an analysis of the tradeoffs between vibration attenuation, control usage, and robustness objectives is presented.

Fig. 6.8 plots the maximum singular values across frequency for the weighted transfer function from input disturbances, d, to modal velocities, e. It is observed that the controllers designed at higher velocities (——) overpass the specified limit at critical frequencies. This means that the controller can not achieve the desired performance at those frequencies. On the other hand, the control design at slow velocities (——) is also surpassing the magnitude limit at lower frequencies. However, this does not constitute a bad design since the modes at low frequencies are very well damped. Fig. 6.9 shows the maximum singular values plot across frequency for the transfer function from sensor noise, n, to control action, u. This transfer function limits the control usage of the controller to avoid saturation. As expected, the control usage increases with airspeed due to the stabilization of the three flutter modes. As before, it is observed that the controller requires a higher bandwidth as velocity increases.
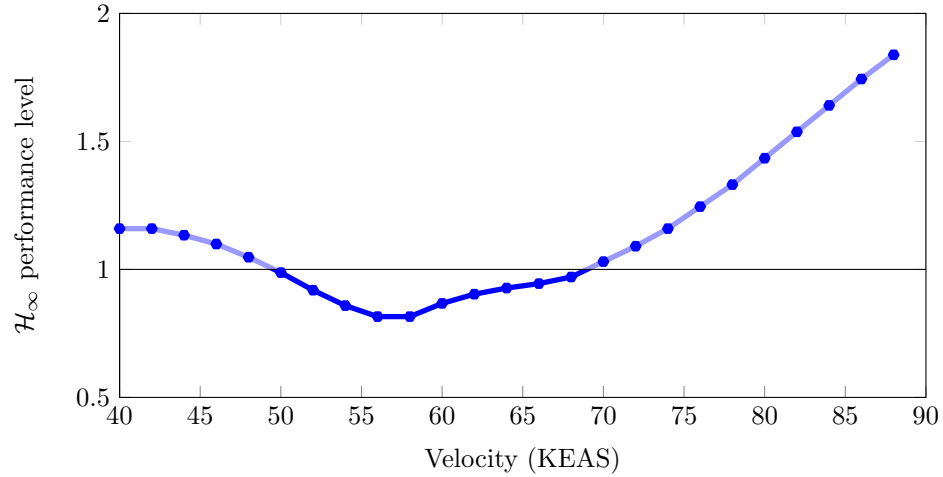
Figure 6.5: Performance level γ variation across the flight envelope achieved by the $\mathcal{H}_\infty$ point design controllers
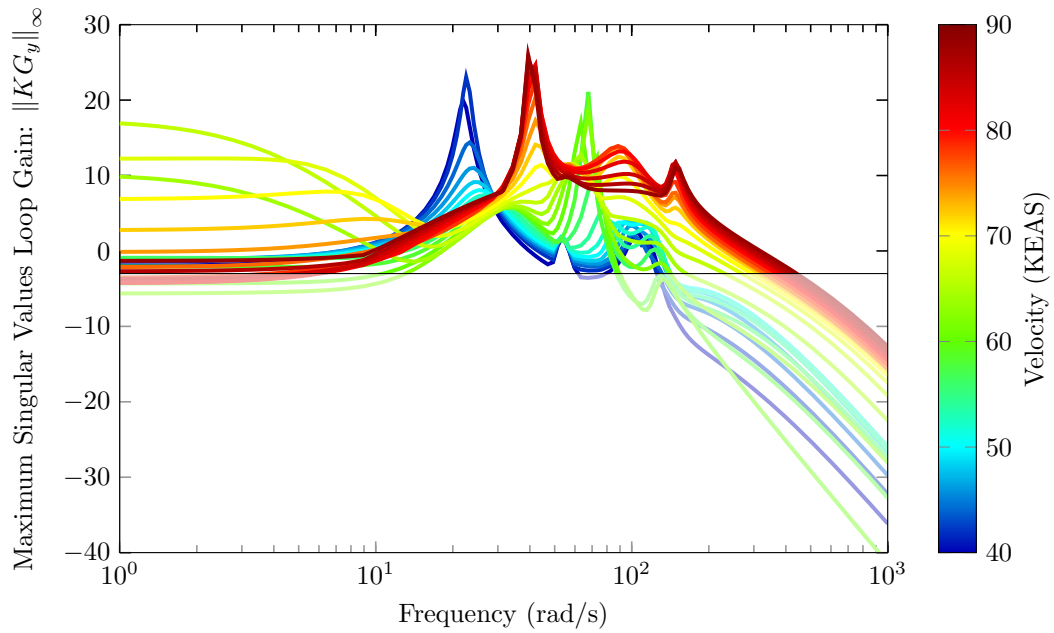
Figure 6.6: Maximum singular value plot of loop gain KG_y

The robustness in the system is imposed by the transfer function from input disturbances, d, to control action signals, u, and by the transfer function from noise disturbances, n, to the modal velocities, e. Fig. 6.10 and Fig. 6.11 show the maximum singular values for these weighted transfer functions. Both plots show that the desired robustness is harder
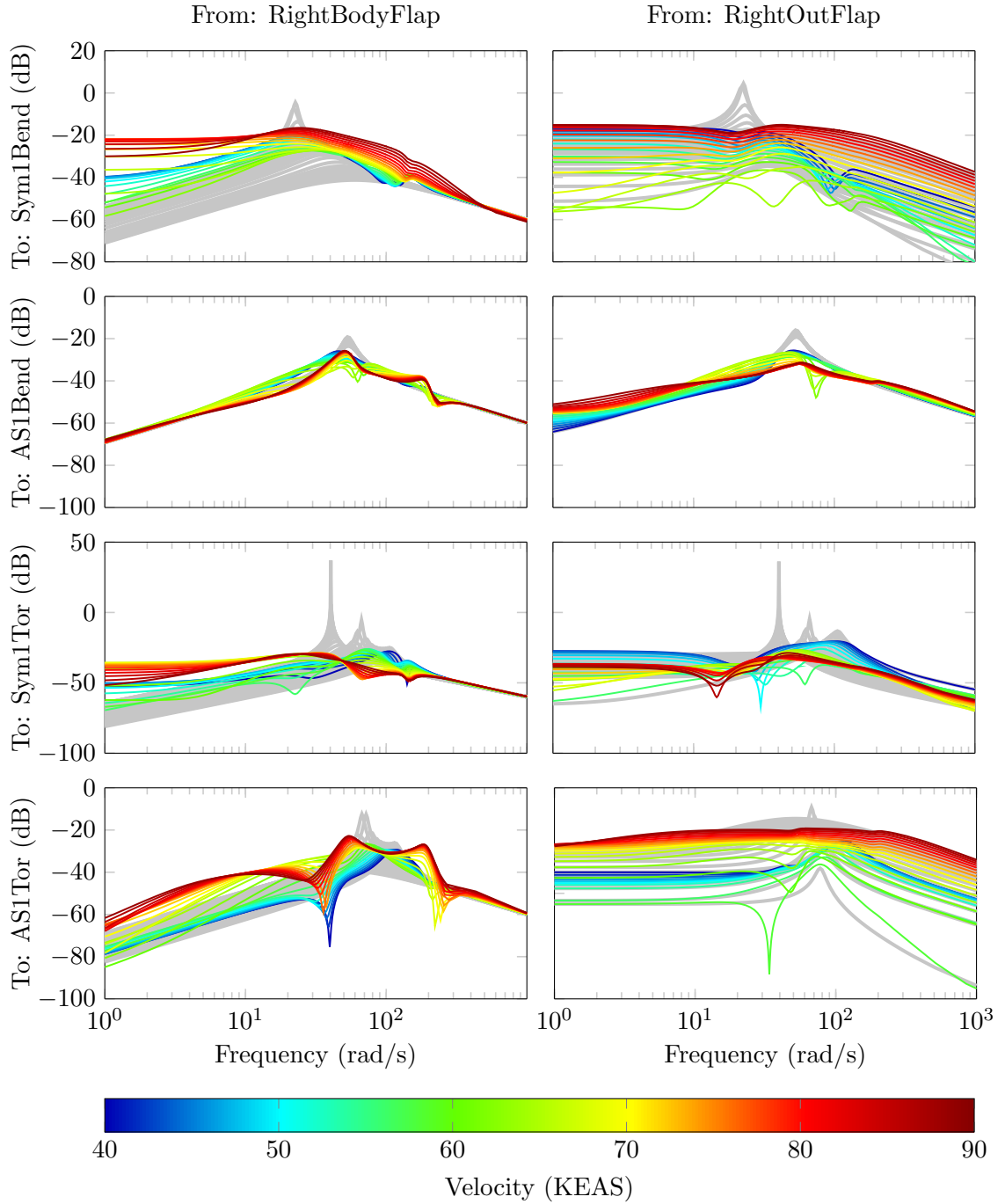
Figure 6.7: Frequency response magnitude from input disturbances, $\tilde{d}$, to modal velocities, $\tilde{e}$. Open-loop (———) and closed-loop (———/———) system comparison.

to achieve as airspeed increases. Fig. 6.12 and Fig. 6.13 plot the input and output disk margins achieved by the controller across the flight envelope. Notice that the input disk
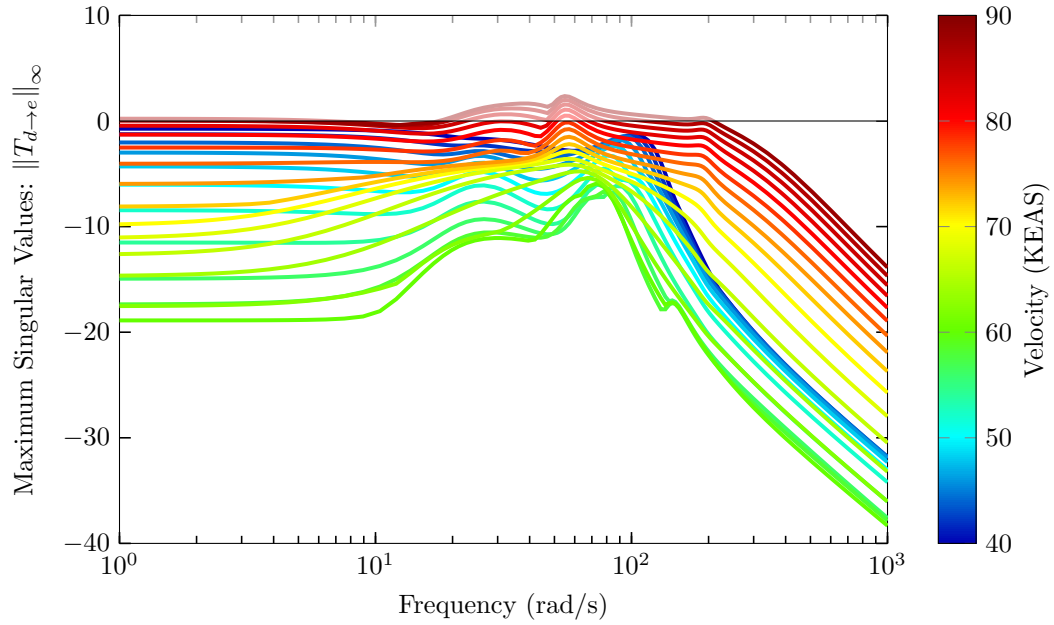
Figure 6.8: Maximum singular value plot of the weighted closed-loop system from input disturbances, d, to modal velocities, e.
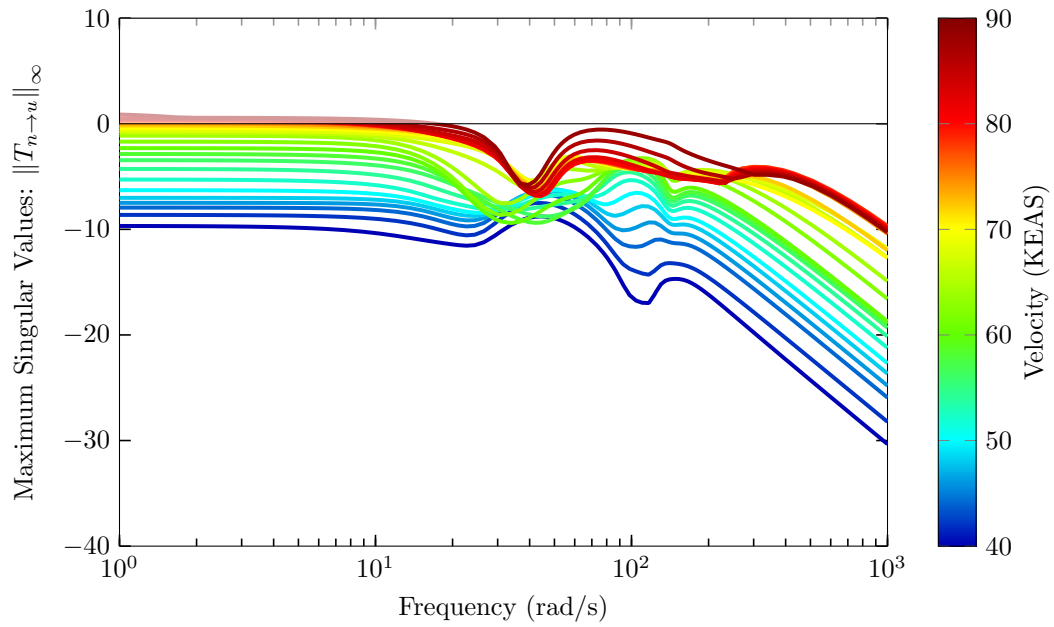
Figure 6.9: Maximum singular value plot of the weighted closed-loop system from noise disturbances, n to control signal deflections, u.
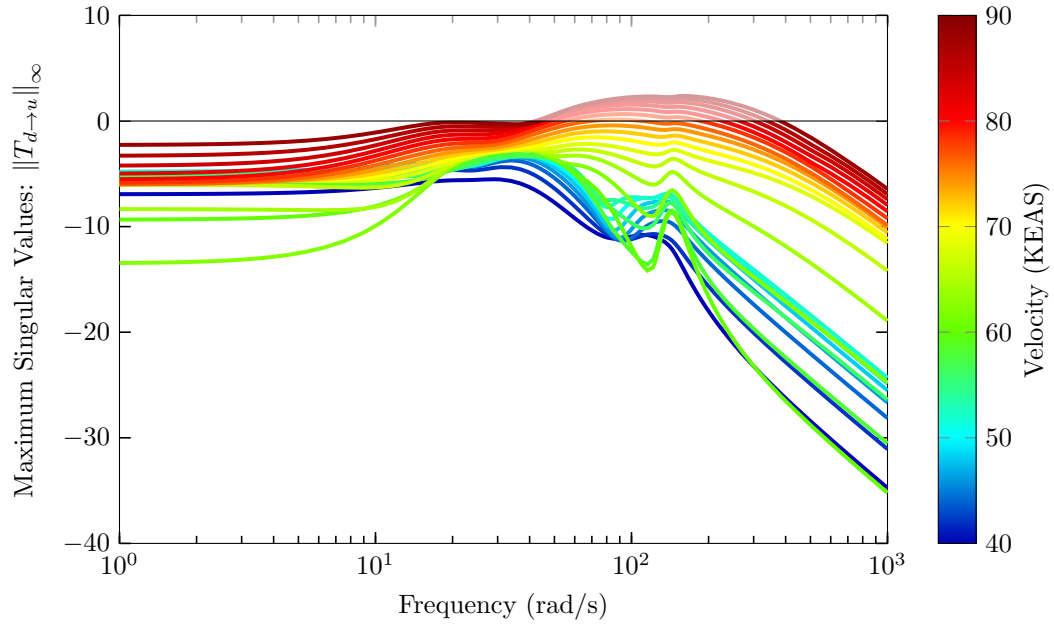
Figure 6.10: Maximum singular value plot of the weighted closed-loop system from input disturbances, d, to control signal deflections, u.
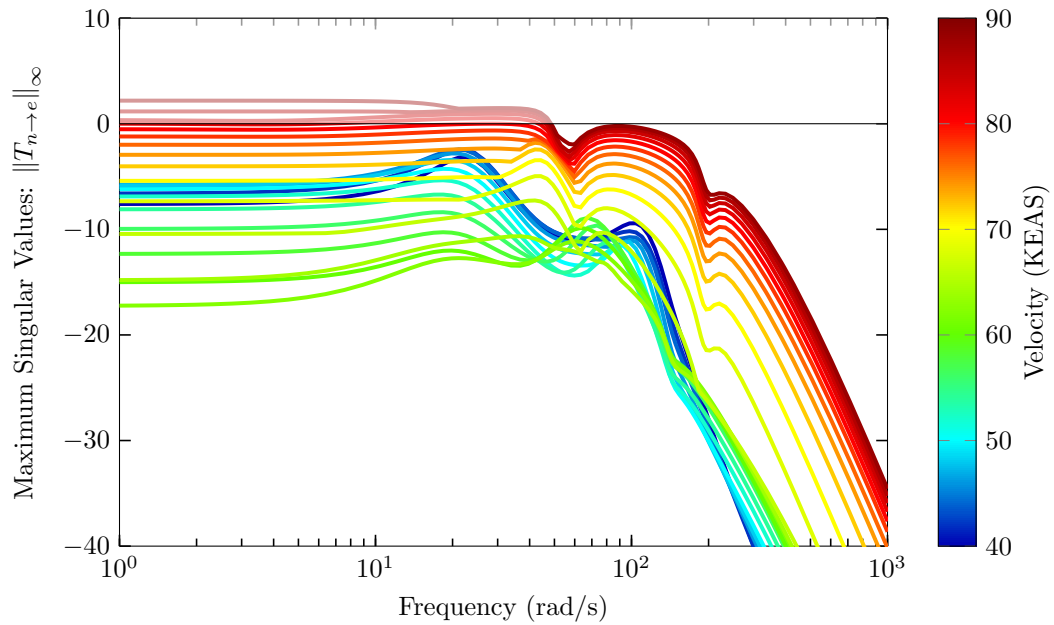
Figure 6.11: Maximum singular value plot of the weighted closed-loop system from noise disturbances, n, to modal velocities, e.

margins of the outboard flaps are higher for velocities at which the body freedom flutter is the only instability in the aircraft. These results are to be expected because the body freedom flutter is mainly suppressed by the body flaps.

In addition, it is observed that the body flaps margins degrade across the flight envelope with a slightly improvement at velocities between 60 and 70 KEAS. This means that the system stability is more sensitive to perturbations in the body flaps at velocities between 40 and 60 KEAS. Instead, the outboard disk margins degrade significantly at velocities higher than 60 KEAS. Recall that the two wing flutter modes occur at this airspeed. This means that the outboard flaps are mainly suppressing the two wing flutter modes and hence they are more sensitive to perturbations at higher velocities. Following, a similar analysis for the output disk margins is presented.
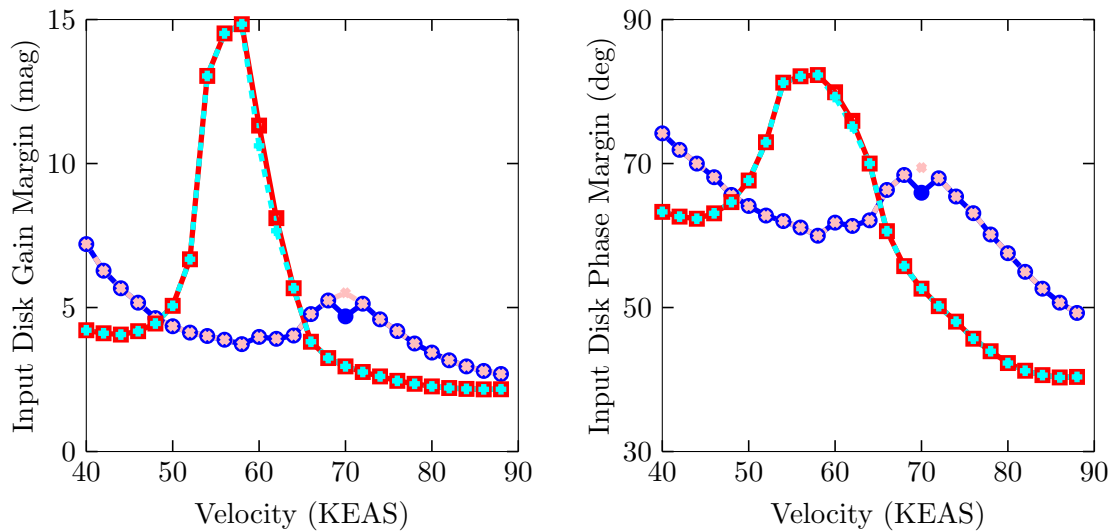
Figure 6.12: Input disk margins for right/left body flap (━●━/━ ━) and right/left outboard flap (━■━/━ ━)

The output disk margins in Fig. 6.13 show that the control system is more sensitive to disturbances in the sensor measurements. It is observed that the margins for the accelerometers in the wing decrease significantly with airspeed. This is to be expected as the information provided by the wing accelerometers is key for the suppression of all three flutter modes. On the other hand, the accelerometers in the center body achieve higher margins. Here, the information provided by the aft accelerometer seems to be more important for stability of the body freedom flutter than the forward body accelerometer.

In addition, the multivariable gain and phase margins of the system are plotted in
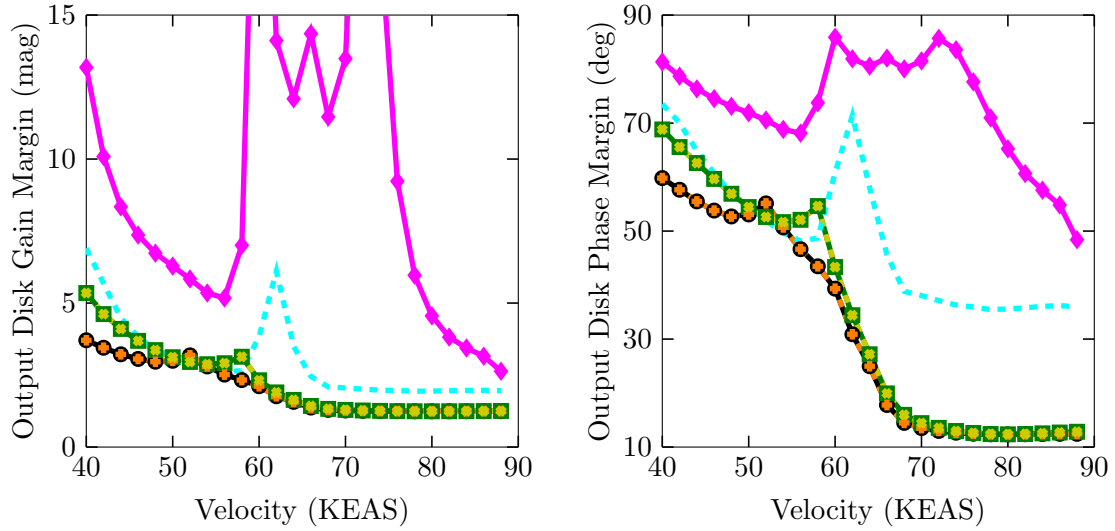
Figure 6.13: Output disk margins for right/left wing forward accels (●/ ●), right/left wing aft accels (■/ ■), body forward accel (◆), and body aft accel ( )

Fig. 6.14. This plot shows that if the input/output channels are perturbed simultaneously, the system has poor robustness margins across the flight envelope. These results will be analyzed in Section 6.4. Finally, the control simulation with the full order model of the aircraft (148 states) is presented next.
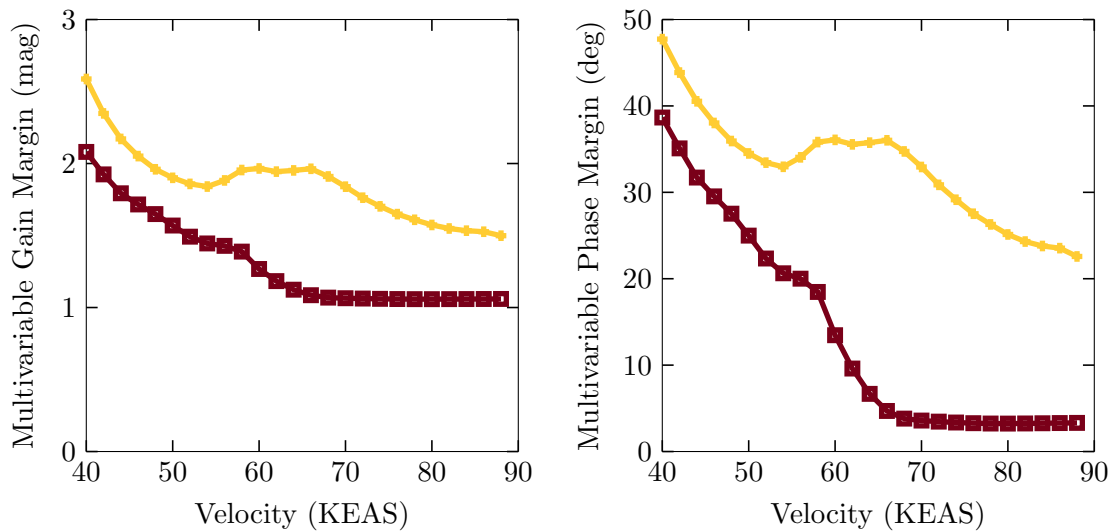
Figure 6.14: Multivariable input ( ) and output ( ) margins

Fig. 6.15 shows the frequency response magnitude for four different transfer functions of the open-loop and closed-loop full order model. Here, the controller successfully adds damping to the modes between 10 and 100 rad/s. Notice that the controller increases the sensitivity to disturbance rejection at low frequencies (10-20 rad/s) and crossover frequencies (60-200 rad/s) in the fastest velocities of the flight envelope. Despite this, the controllers do not destabilize the system at frequencies beyond 160 rad/s where the reduced order model is not accurate.
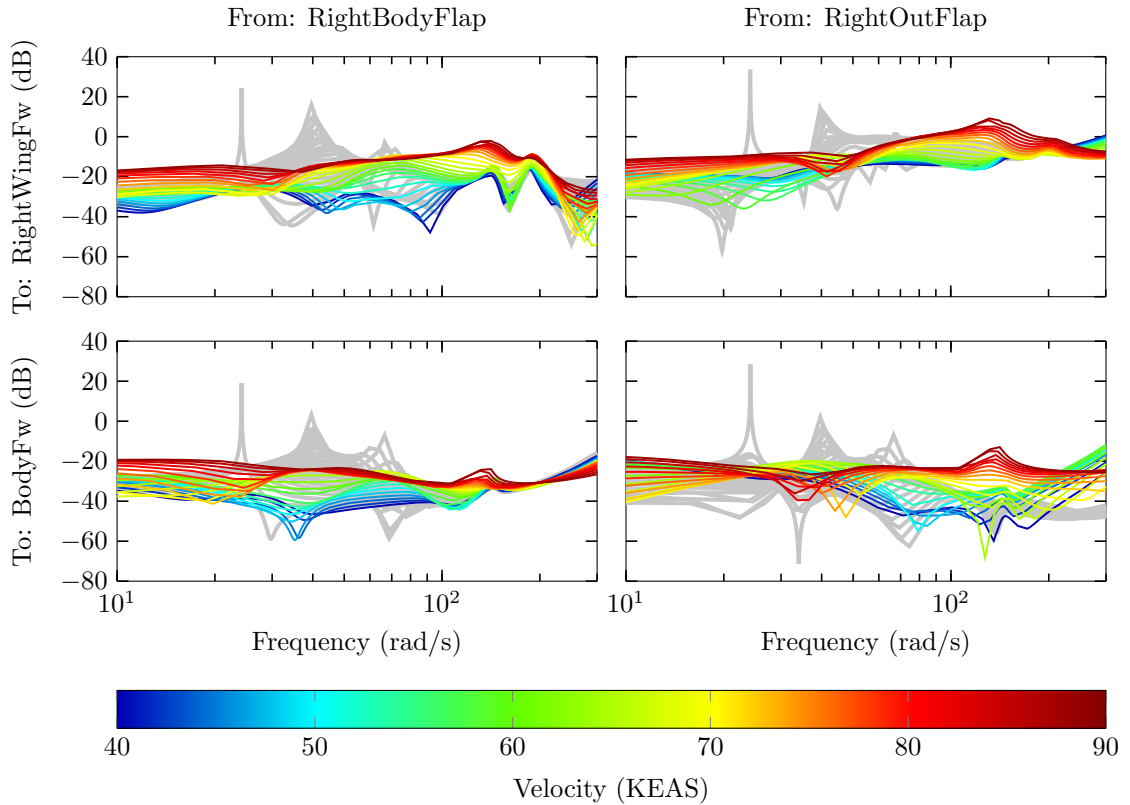
Figure 6.15: Frequency response magnitude from input disturbances at right body flap and right outboard flap to right wing forward accelerometer and body forward accelerometer. Open-loop (——) and closed-loop (——/——) full order model (148 states) comparison.

Two time simulations are carried out with the $\mathcal{H}_\infty$ controllers for the reduced order model and full order model. First, a disturbance acting on the body flaps are evaluated. Fig. 6.16 shows the disturbance wave and magnitude applied to the simulation. Second, disturbances acting on the outboard flaps are evaluated and Fig. 6.17 depicts those disturbances.
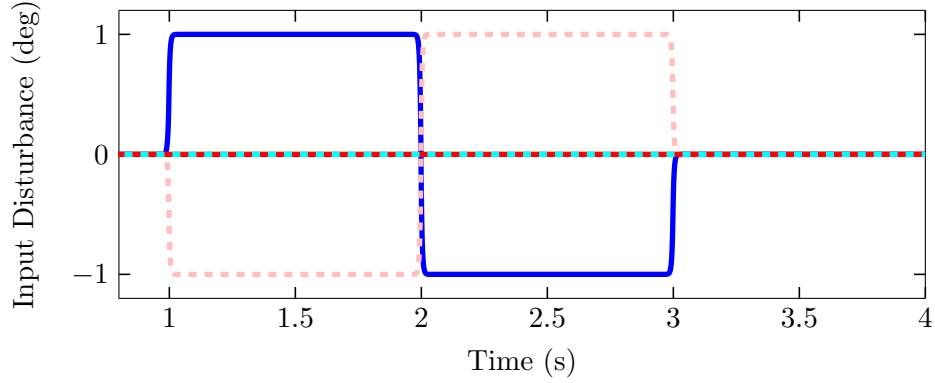
Figure 6.16: Case A. Disturbance on right/left body flap (▬▬/▪▪▪) and right/left outboard flap (▬▬/▪▪▪)
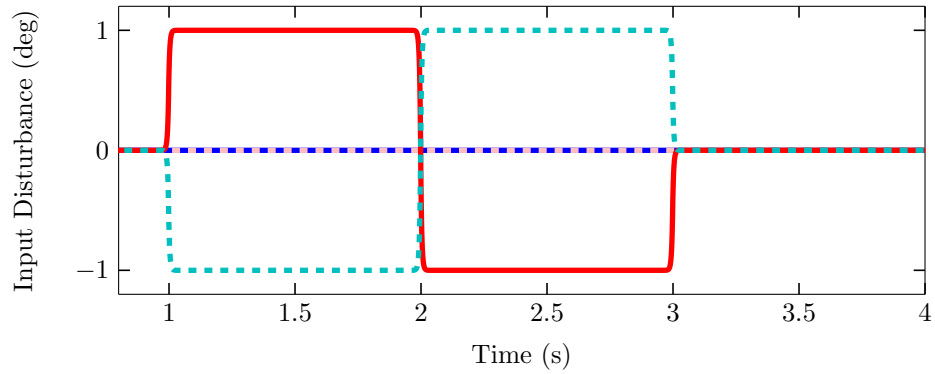
Figure 6.17: Case B. Disturbance on right/left body flap (▬▬/▪▪▪) and right/left outboard flap (▬▬/▪▪▪)

Fig. 6.18 shows the acceleration of vibrations in the wing and center body of the vehicle flying at 62 KEAS and subject to disturbances in the body flaps (Case A). Notice that the vibrations in the center body are completely eliminated by the control action. However, the disturbances in the body flaps induce some vibrations in the wings. Even though the controller stabilizes the system and successfully rejects the disturbances, it does not provide sufficient damping to the anti-symmetric bending mode. However, these levels of accelerations are still tolerable in flight. Fig. 6.19 shows the control action provided by the four flaps in the vehicle. Here, both set of flaps are deflected less than 1 deg to stabilize and provide damping to the system. Given that the maximum deflection of the flaps is 25 deg, this simulation results will not saturate the system.

Fig. 6.20 shows the acceleration of vibrations in the wing and center body of the vehicle flying at 62 KEAS and subject to disturbances in the outboard flaps (Case B). As in Case A, the vibrations in the center body are completely eliminated by the control action and vibrations in the wings are also present in the vehicle. Notice that the levels of accelerations are higher when the vehicle is subject to disturbances in the outboard flaps. This is to be expected because the outboard flaps generate a higher moment when they are perturbed. Fig. 6.19 shows the control action provided by the four flaps in the vehicle. Again, both set of flaps are deflected less than 1 deg to stabilize and provide damping to the system.

On the other hand, the plots also shows a comparison between simulations with the reduced order model and the full order model. In both cases, the responses obtained with the full order model match accurately with the responses of the reduced order model for which the controller was designed. This means that the reduced order model is accurate for the control objectives specified. The next section presents the results of an LPV controller designed with these same specifications.

Figure 6.18: Case A. Acceleration time responses of closed-loop full order system (▬▬) and closed-loop reduced order system (- - -) at 62 KEAS
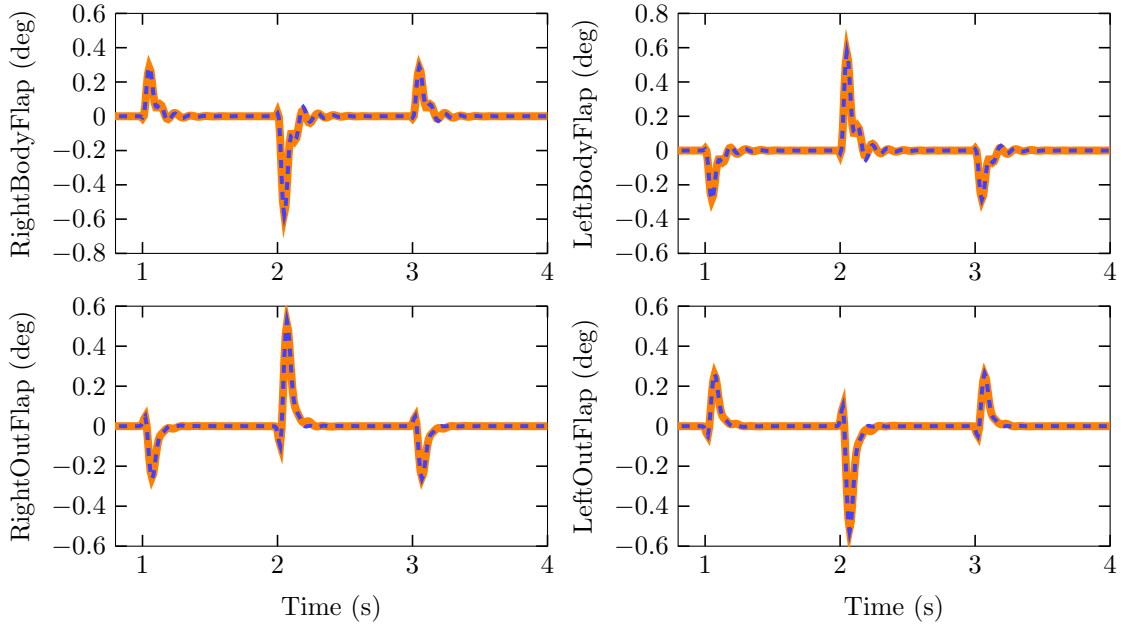
Figure 6.19: Case A. Flap control time responses of closed-loop full order system (━━) and closed-loop reduced order system (- - -) at 62 KEAS

6.3 Output Feedback LPV Controller

An LPV controller is synthesized for the BFF vehicle based on the control formulation shown in Fig. 6.2. This control formulation uses the same weighting functions as in the $\mathcal{H}_\infty$ point designs. However, the flight envelope to study in this section corresponds to velocities between 40 and 64 KEAS with increments of 2 KEAS. These 13 plant models of the BFF vehicle exhibit three flutter modes. The flutter modes can be seen in Fig. 6.3 where 40 KEAS is represented by the blue dark curves and 64 KEAS is represented by the bright green curves. Recall that this figure shows the change of dynamics of the BFF vehicle as seen through the modal velocities. Here, modal velocities are the main performance measure to guarantee damping in the system. Next, the LPV controller synthesis results are presented.

Initially, LPV control design algorithms with non-rate bounds were used to synthesize a controller. However, the algorithms could not find a feasible solution for this problem. This indicates that it is not possible to synthesize an LPV controller that allows the airspeed to vary infinitely fast. As expected, the LPV controller can not allow the vehicle to switch infinitely fast between a stable and unstable plant. Hence, the rate-bounded LPV synthesis
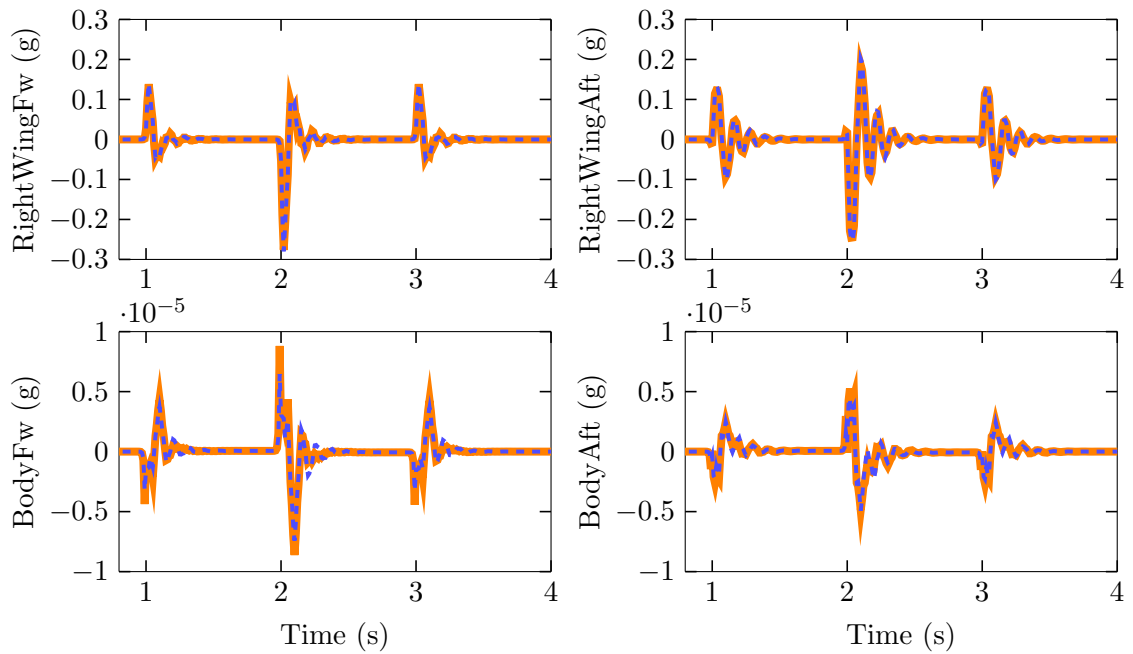
Figure 6.20: Case B. Acceleration time responses of closed-loop full order system (━━) and closed-loop reduced order system (- - -) at 62 KEAS

algorithm explained in Section 6.1 is used to design the parameter-varying controller. Here, the rate of change of airspeed is limited to ± 0.5 KEAS/s which corresponds to accelerations of 30 KEAS/min. This airspeed variation is close to the expected rate of the actual BFF vehicle in flight. On the other hand, the parametrization of the algorithm solutions are selected as quadratic basis functions. All these design parameters are included using the Matlab LPVTools [94].

Fig. 6.22 shows the frequency response from the right body and outboard flaps to the accelerometers in the right wing and center body of the full order (148 states) open-loop and closed-loop systems. This plot indicates that the LPV controller effectively suppresses the flutter modes peaks between 20 and 100 rad/s. Without the active flutter suppression, flying the vehicle above 42 KEAS would inevitably result in immediate structural failure due to the fast growing oscillation at 24 rad/s. In general, the disturbances are well attenuated for all considered airspeed, however this sensitivity is slightly increased at some low frequencies. The sensitivity increase does not destabilize any low frequency mode as was also observed in the $\mathcal{H}_\infty$ point designs.

Fig. 6.23 and Fig. 6.24 show the input and output disk margins obtained by the LPV controller at each grid point. Notice that these margins are very similar and in some cases
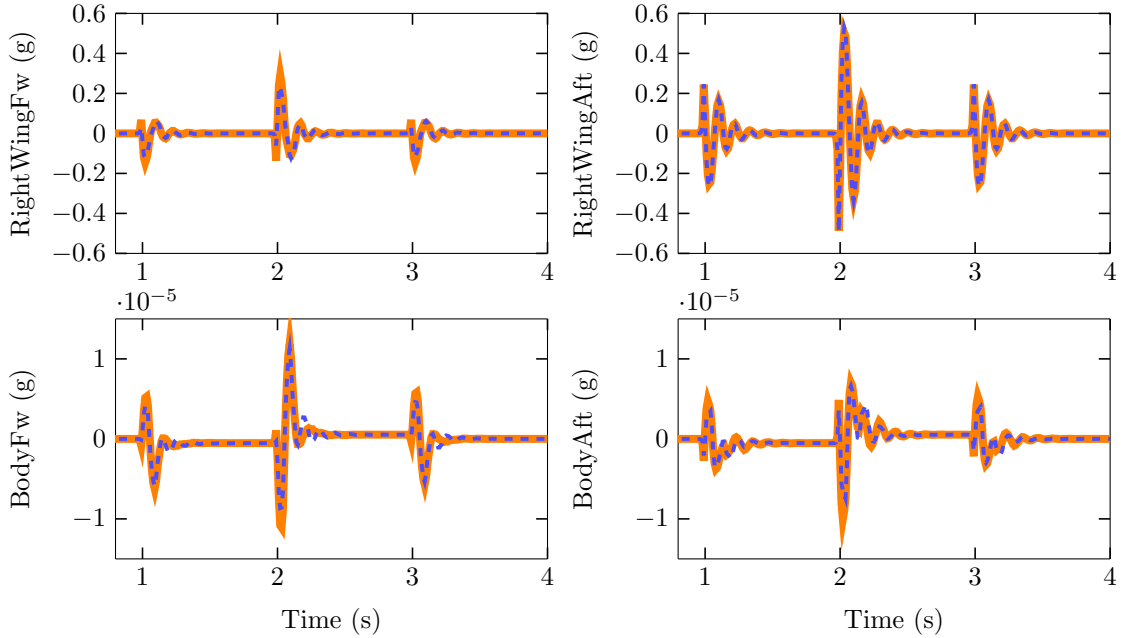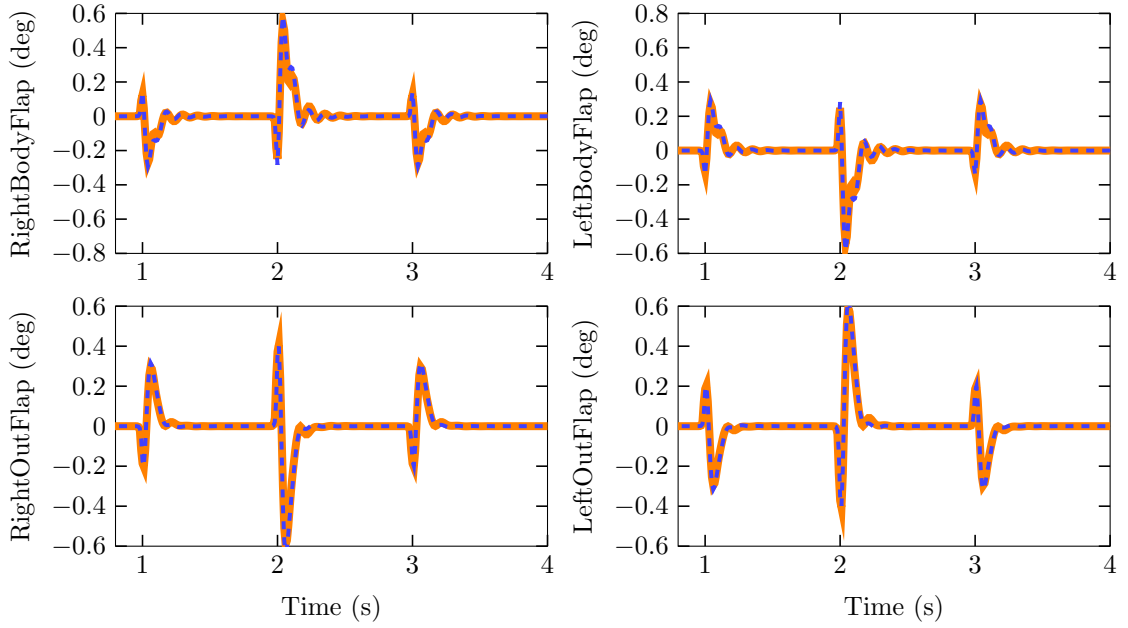
Figure 6.21: Case B. Flap control time responses of closed-loop full order system (━━) and closed-loop reduced order system (---) at 62 KEAS

better than the margins obtained from the $\mathcal{H}_\infty$ point designs. This indicates that the LPV controller guarantees the stability and performance of the closed-loop vehicle flying between 40 and 64 KEAS. Next, a comparison of time response simulations are presented.

The same two disturbances cases used in the point designs to evaluate the $\mathcal{H}_\infty$ controllers are simulated with the LPV controller. Recall that Case A corresponds to input disturbances in the body flaps and Case B corresponds to input disturbances in the outboard flaps. In addition, the airspeed is set to be time-variant as shown in Fig. 6.25. The simulation results show that the responses obtained with the LPV controller are very similar to the responses obtained with the $\mathcal{H}_\infty$ controller. Notice that the LPV controller slightly reduces acceleration amplitudes in the response. This is to be expected because the LPV controller is designed to account for speed variations. In conclusion, the LPV controller designed for velocities between 40 and 60 KEAS with rate-bounds of ± 0.5 KEAS/s successfully stabilizes the flutter modes and provides additional damping to flexible modes in the region of interest. However, the system does not have a good robustness at high velocities. This situation is due to the high instability of the open-loop system at those velocities. An analysis of the limitations in control of the system given high instabilities follows.
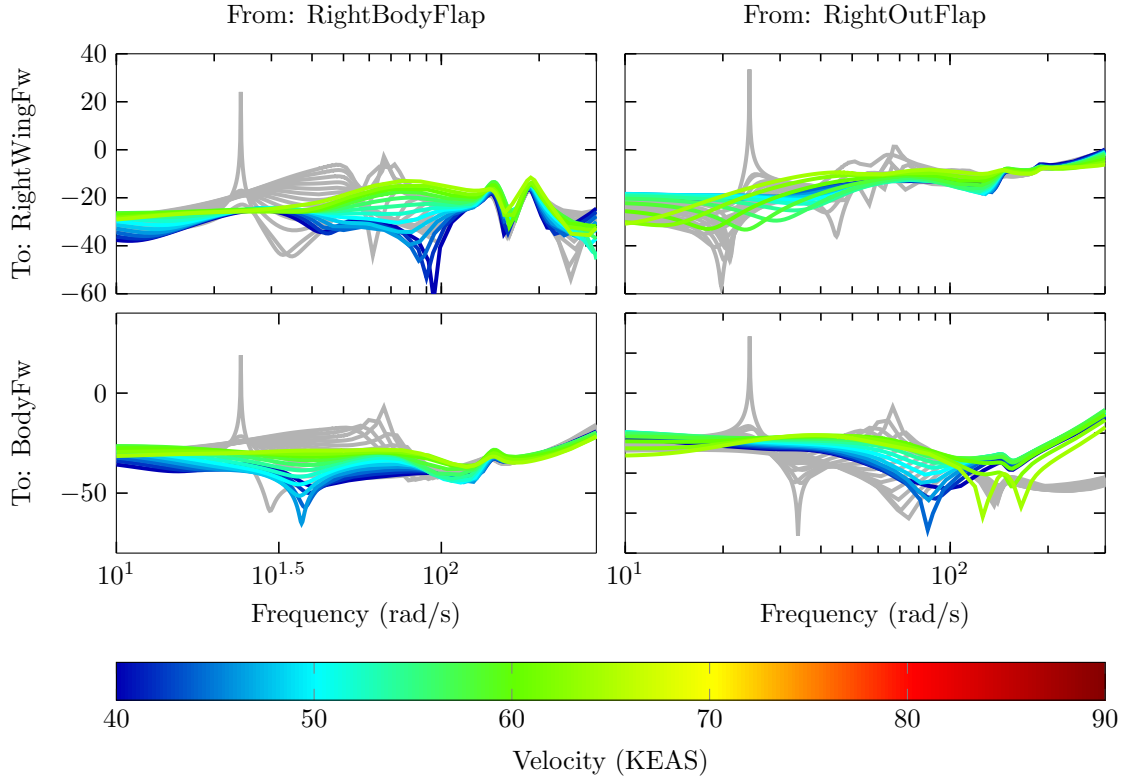
Figure 6.22: Frequency response magnitude from input disturbances at right body flap and right outboard flap to right wing forward accelerometer and body forward accelerometer. Open-loop (——) and closed-loop (——/——) full order model (148 states) comparison.

6.4 Limitations in Control Imposed by Unstable Poles

The previous sections showed that the feedback design goals are inherently conflicting and a tradeoff must be performed among the different performance and robustness objectives. An important tool used to quantify feedback design constraints is the Bode's sensitivity integral relation. This integral states that for single-input, single-output open-loop stable systems, the integral of the logarithmic magnitude of the sensitivity function over all frequencies must equal zero. Later, the theorem was extended to open-loop unstable systems showing that the presence of unstable poles makes the sensitivity tradeoff a more difficult task [95]. This section presents the limitations in control of the BFF vehicle imposed by its flutter modes. Here, a multivariable extension of Bode's theorem is used.

Consider the output sensitivity function, $S_O(s) = (I + L_O(s))^{-1}$, and the output complementary sensitivity function, $T_O(s) = L_O(s)(I + L_O(s))^{-1}$, where $L_O(s)$ is the open-loop
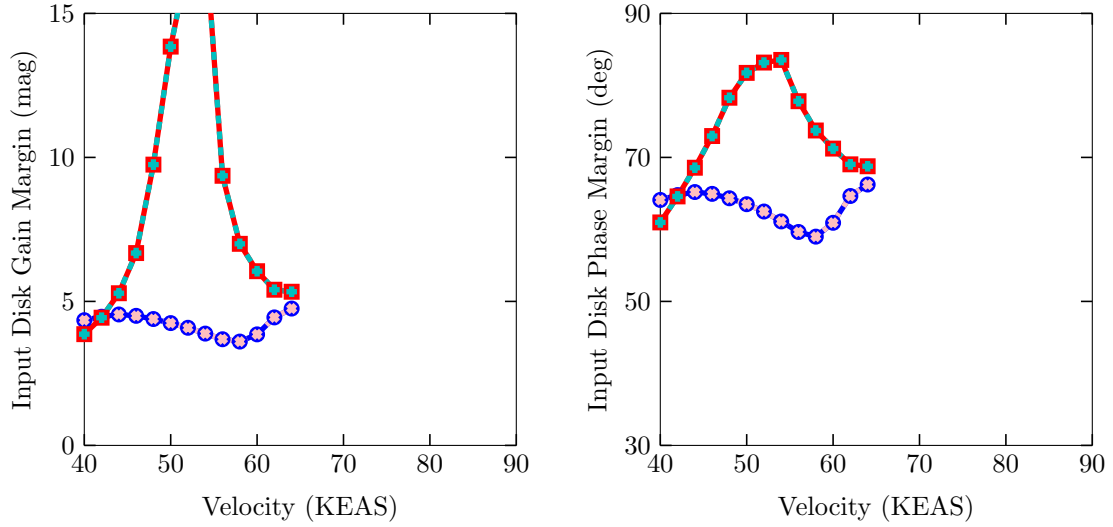
Figure 6.23: Input disk margins for right/left body flap (━●━/━●━) and right/left outboard flap (━■━/━■━)
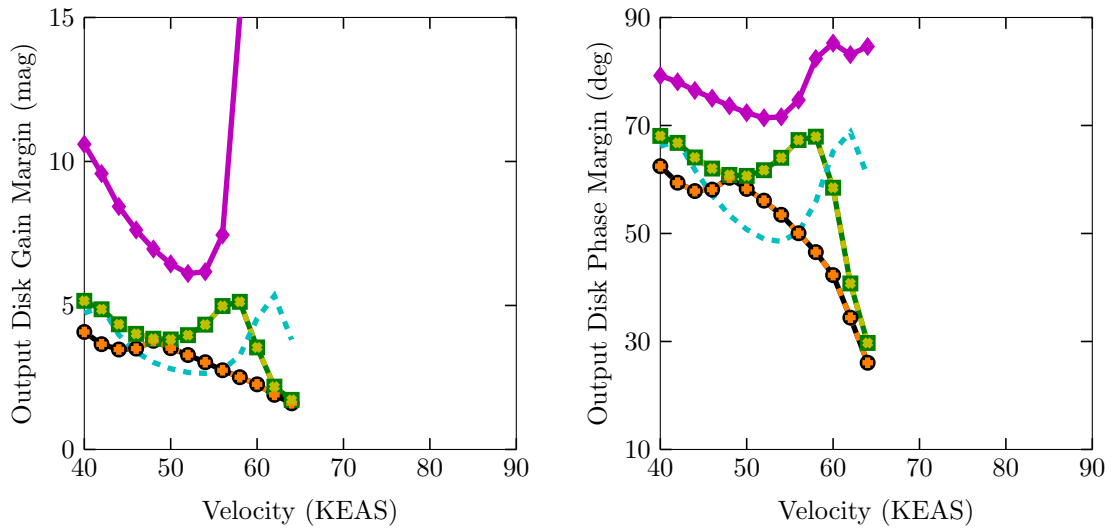
Figure 6.24: Output disk margins for right/left wing forward accels (━●━/━●━), right/left wing aft accels (━■━/━■━), body forward accel (━◆━), and body aft accel (━ ━ ━)

gain $G(s)K(s)$. Now, if $G(s)$ has a right half-plane pole p with output direction y_p, then
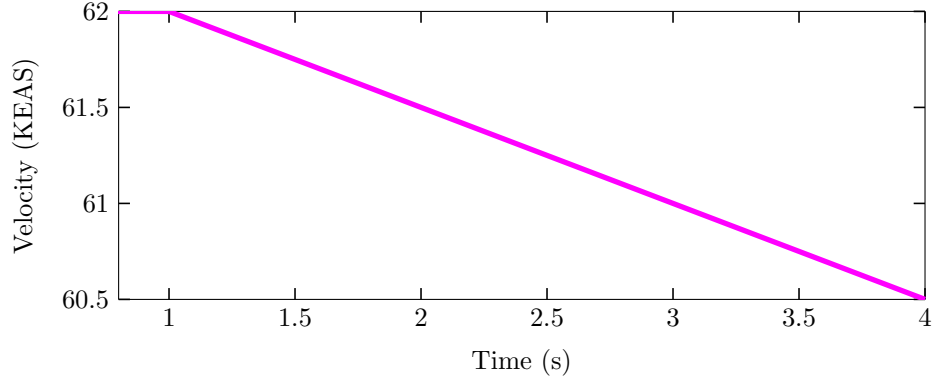
Figure 6.25: Time-varying velocity

Figure 6.26: Case A. Acceleration time responses of closed-loop full order system with LPV controller ($\mathbf{---}$) and $\mathcal{H}_\infty$ controller ($\mathbf{\rule[0.3ex]{1.5em}{1.2pt}}$) at 62 KEAS

for internal stability the following interpolation constraints apply:

$$S_O(p)y_p = 0 \tag{6.18}$$

$$T_O(p)y_p = y_p \tag{6.19}$$

Recall that p is a pole of $G(s)$ if there exist and output direction y_p and an input direction u_p with infinite gain for $s = p$, i.e. $G(p)u_p = \infty$ and $y_p^*G(p) = \infty$. These pole directions

115

Figure 6.27: Case A. Flap control time responses of closed-loop full order system with LPV controller (---) and $\mathcal{H}_\infty$ controller (━━) at $62\,\text{KEAS}$

can be computed from [96]

$$y_p = Cx_R \tag{6.20}$$

$$u_p = B^T x_L \tag{6.21}$$

where x_R and x_L are the eigenvectors corresponding to the two eigenvalue problems $Ax_R = px_R$ and $x_L^* A = x_L^* p$, respectively. Here, the pole directions are normalized such that $y_p^* y_p = 1$ and $u_p^* u_p = 1$. With these, the Bode's integral for multivariable unstable systems is defined as

$$\int_0^\infty \ln \bar{\sigma}(S(j\omega))d\omega \geq \pi \lambda_{\max}\left(\sum_{j=1}^k \Re(p_j) y_{p_j} y_{p_j}^*\right) \tag{6.22}$$

where

$$\lambda_{\max}\left(\Re(p_1) y_{p_1} y_{p_1}^* + \cdots + \Re(p_k) y_{p_k} y_{p_k}^*\right) = \lambda_{\max}\left(\begin{bmatrix} y_{p_1} \cdots y_{p_k} \end{bmatrix} \begin{bmatrix} \Re(p_1) & \cdots & 0 \\ \vdots & \ddots & \vdots \\ 0 & \cdots & \Re(p_k) \end{bmatrix} \begin{bmatrix} y_{p_1}^* \\ \vdots \\ y_{p_k}^* \end{bmatrix}\right) \tag{6.23}$$

The integral constraint in (6.22) is used to analyze the control limitations of the BFF vehicle in the presence of the three flutter modes. Here, a simple shape for the desired

116
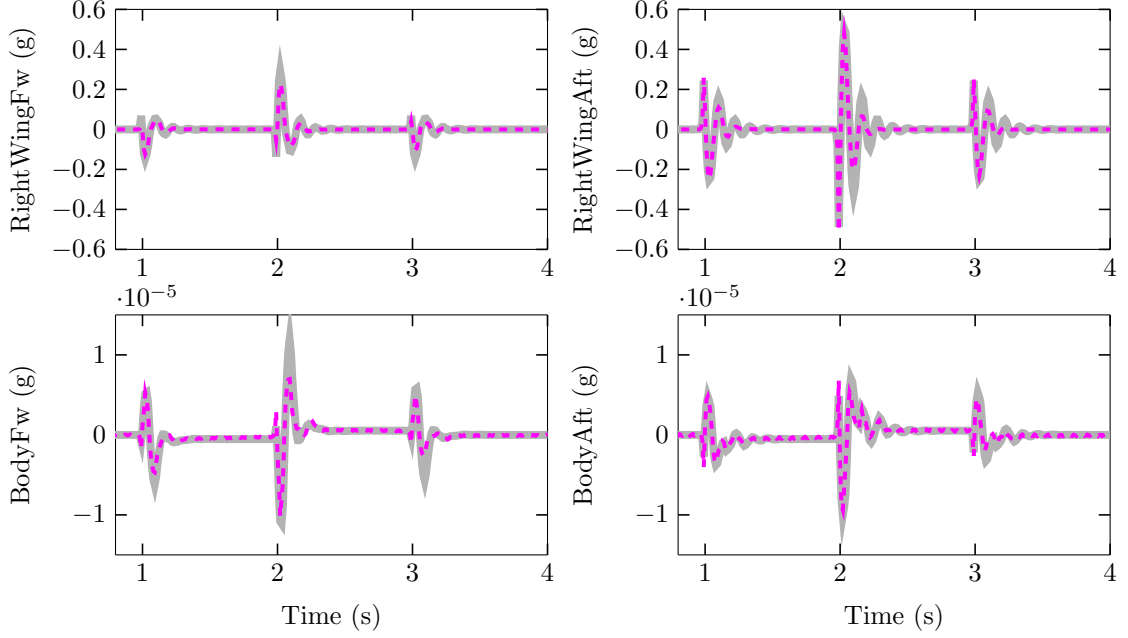
Figure 6.28: Case B. Acceleration time responses of closed-loop full order system with LPV controller ($\mathbf{- - -}$) and $\mathcal{H}_\infty$ controller ($\rule[0.3ex]{1.2em}{0.35ex}$) at $62\,\mathrm{KEAS}$

sensitivity function is considered to perform the analysis [97]. Fig. 6.30 shows that the closed-loop system has small sensitivity at low frequencies rising linearly above $0\,\mathrm{dB}$ up to Ω_1. Following, the sensitivity function stays flat from Ω_1 to Ω_a in order to pay as small sensitivity penalty as possible. Finally, the sensitivity returns to $0\,\mathrm{dB}$ beyond Ω_a so that unmodeled dynamics is not excited by the controller. This frequency is usually determined by the actuator bandwidth and/or model uncertainty. From this, the minimum sensitivity peak value, $s_{\min}$, is determined by the performance requirements Ω_1 and Ω_a as

$$s_{\min} = \exp\left[\frac{\pi\lambda_{\max}\left(\sum_{j=1}^{k}\Re(p_j)y_{p_j}y_{p_j}^*\right) + \Omega_1}{\Omega_a}\right] \tag{6.24}$$

This maximum sensitivity peak is related to the multivariable gain and phase margins of the system by [98]

$$GM = \left[\frac{1}{1 + s_{\min}^{-1}}, \ \frac{1}{1 - s_{\min}^{-1}}\right] \tag{6.25}$$

$$PM \subseteq \left[-2\sin^{-1}\left(\frac{s_{\min}^{-1}}{2}\right), \ +2\sin^{-1}\left(\frac{s_{\min}^{-1}}{2}\right)\right] \tag{6.26}$$
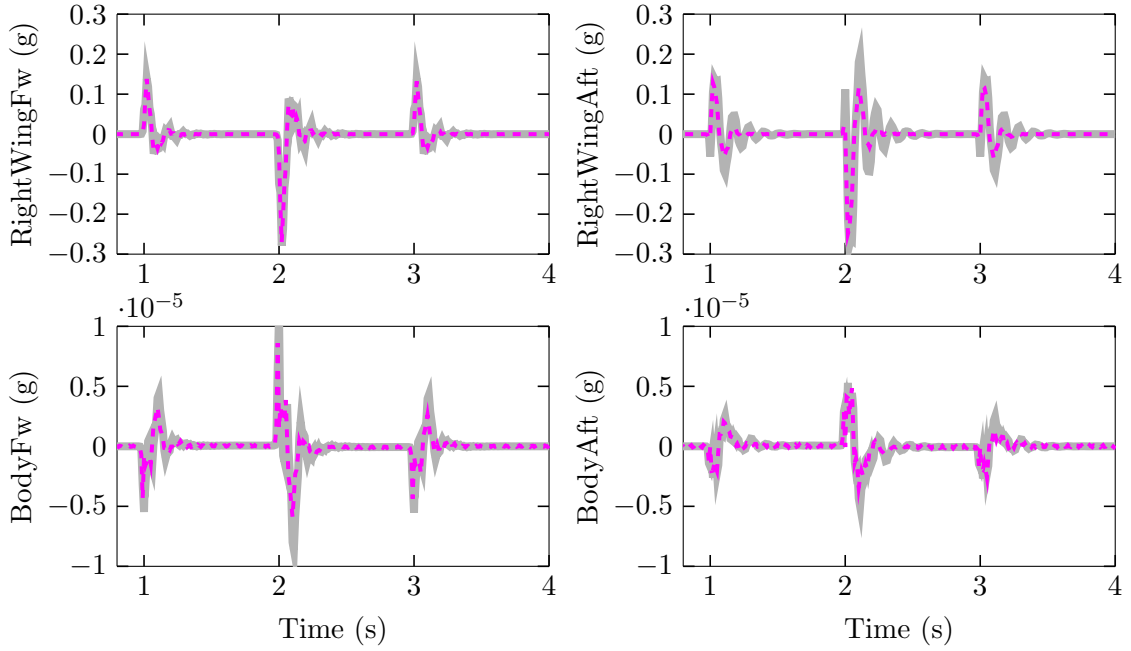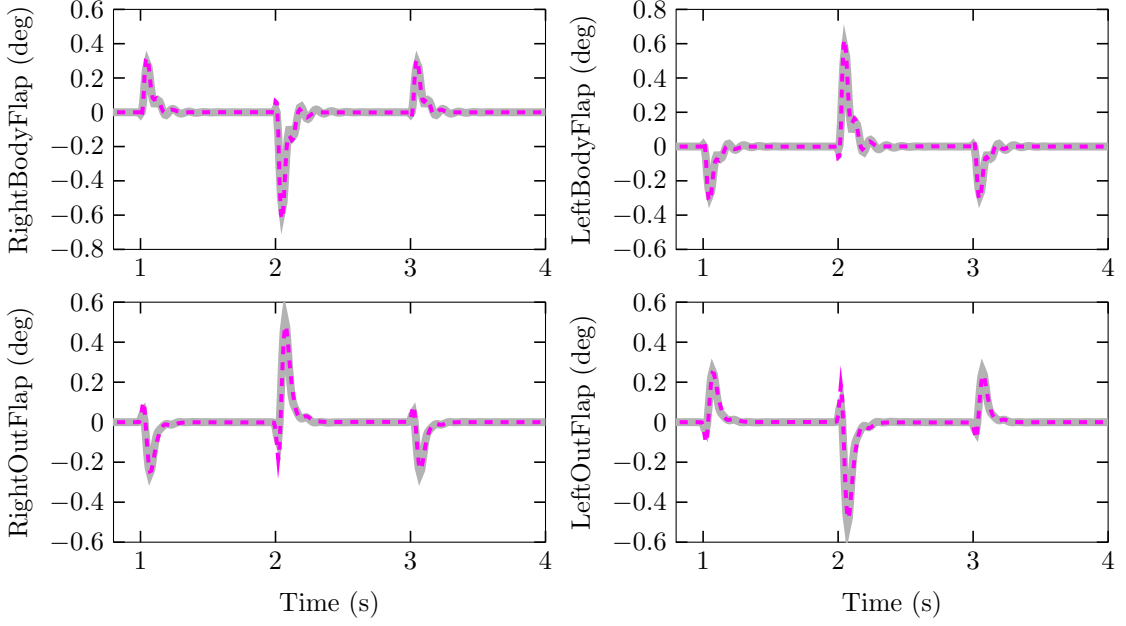
117
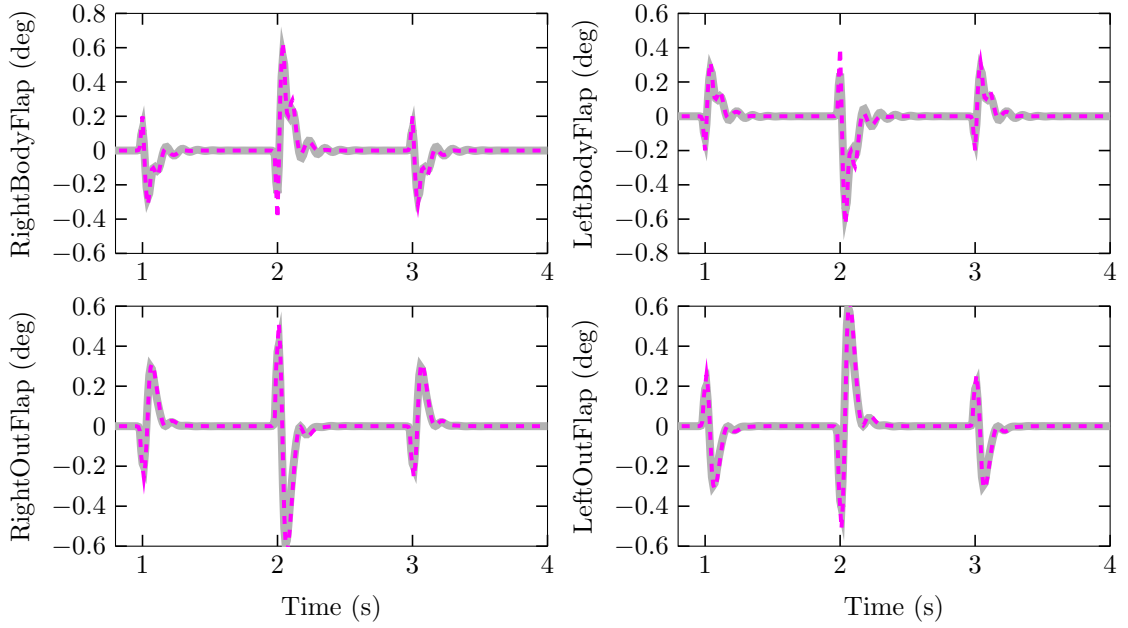
Figure 6.29: Case B. Flap control time responses of closed-loop full order system with LPV controller (---) and $\mathcal{H}_\infty$ controller (▬) at 62 KEAS
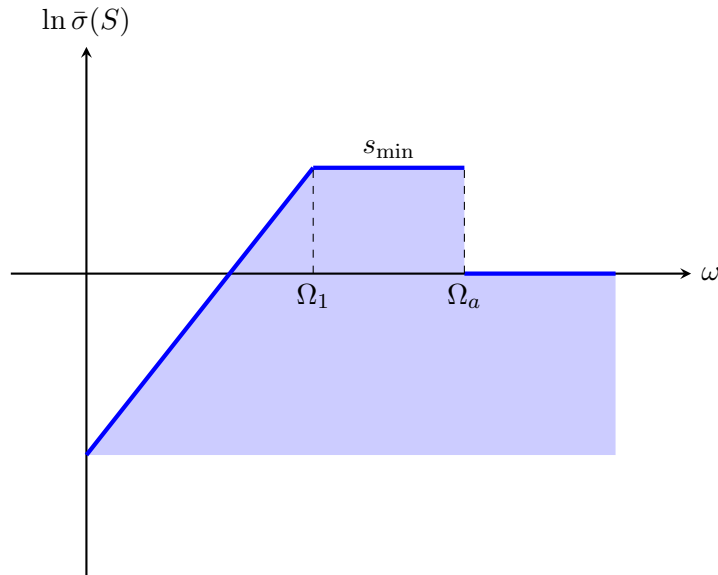
Figure 6.30: Sensitivity function shape

Fig. 6.31 shows the multivariable gain and phase margins in (6.25) and (6.26) computed for a fixed value $\Omega_1 = 100\,\mathrm{rad/s}$ and varying Ω_a. In the first case, the margins for the

118

available bandwidth of the BFF vehicle are plotted. This bandwidth corresponds to $\Omega_a = 160 \, \text{rad/s}$. Here, it is observed that the multivariable gain margins decay from 2 to 1 in magnitude across the flight envelope. Similarly, the multivariable phase margins vary from 30 to 5 deg decaying rapidly at 60 KEAS. Recall that the aircraft is unstable at 42 KEAS with one flutter mode, at 60 KEAS with two flutter modes, and at 62 KEAS with three flutter modes. Notice that these results are very similar to the results obtained from the control design in Section 6.2. Fig. 6.14 shows that the output feedback controllers designed to stabilize the flutter phenomena and attenuate flexible modes do not provide the desired robustness. Here, the multivariable gain margins decay from 2 to 1 in magnitude and the multivariable phase margins vary from 40 to 5 deg as with a significant reduction at 60 KEAS as well.
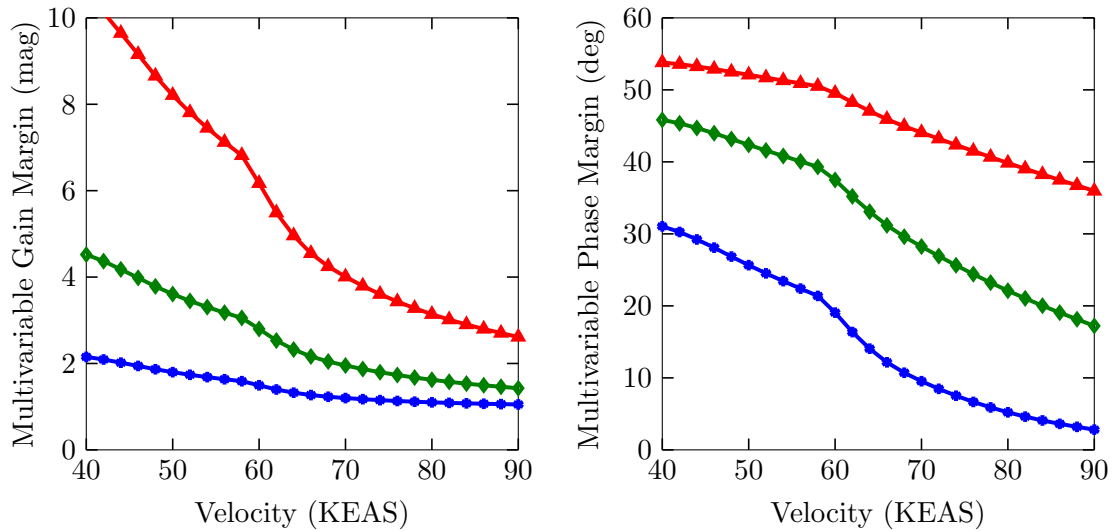
Figure 6.31: Minimum sensitivities for the BFF vehicle with $\Omega_1 = 100 \, \text{rad/s}$ and varying $\Omega_a = 160 \, \text{rad/s}$ (—•—), $\Omega_a = 400 \, \text{rad/s}$ (—◆—), and $\Omega_a = 1000 \, \text{rad/s}$ (—▲—).

On the other hand, two additional control bandwidths are analyzed with the Bode's integral. These correspond to values of $\Omega_a = 400 \, \text{rad/s}$ and $\Omega_a = 1000 \, \text{rad/s}$. Fig. 6.31 shows that if the controller bandwidth is increased then the stability robustness of the system improves. From here, it is observed that the controller needs to respond as fast as $1000 \, \text{rad/s}$ in order to obtain the specified performance with good multivariable margins. However, the control action at this broad frequency range may destabilize unmodeled dynamics at high frequencies. Hence, an accurate model of the plant or appropriate model uncertainty weights are required in the control bandwidth.

6.5 Summary

This chapter presented a linear, parameter-varying output feedback controller for the Body Freedom Flutter aircraft. The control objectives were to suppress the dangerous aeroservoelastic interactions across the flight envelope and to provide additional damping to flexible modes. These objectives are formulated using the modal velocities as the performance measure. Initially, $\mathcal{H}_\infty$ controllers are designed at each individual flight condition. This control interconnection is the base for the design of the parameter-varying controllers. The results showed that the controllers meet the control goals by stabilizing and providing additional damping to the system. However, the rapid change in dynamics across the flight envelope degrades the stability margins at velocities where three flutter modes are present. This is also the reason for which the parameter-varying algorithm design can not find a feasible solution for the entire envelope.

Finally, an analysis of the limitations in control imposed by the unstable poles of the system was presented. Here, a simple shape for the desired sensitivity function of the system was used to compute analytical bounds for performance and robustness. The results showed that the desired performance for the Body Freedom Flutter requires a higher bandwidth than the one provided for the actuators available. In conclusion, it is recommended to perform this control limitation analysis for unstable systems previous to the control design in order to determine the achievable performance, desired robustness and actuator requirements of the system.

Chapter 7

Conclusions and Recommendations

This dissertation detailed an aeroservoelastic (ASE) robust control design procedure for the University of Minnesota Body Freedom Flutter (BFF) aircraft. This procedure is based on the application of linear, parameter-varying (LPV) systems techniques available in the literature. Three main aspects for LPV control design were considered. The first aspect was the model reduction of ASE systems. Here, a four-step procedure was proposed to reduce the model order of ASE LPV models while retaining a set of common states. This procedure was successfully applied to the experimental BFF aircraft, generating a LPV model that was suitable for control synthesis. Model reduction was an important step previous to the design of controllers because LPV synthesis techniques scale badly with the state order of the systems. Hence, the state order reduction of ASE models that retained their natural LPV description allowed the application of well-known LPV synthesis techniques for the design of robust controllers.

The second aspect considered in this dissertation was the selection of actuators and sensors for feedback control. This actuator and sensor selection method was based on the robust stability and robust performance closed-loop objectives of ASE systems. The proposed method was also applied to the experimental BFF aircraft for which active flutter suppression and structural modes attenuation were the main control objectives. Selection of adequate sensor measurements and control effectors played a key role in the control design process. A wrong choice of actuators or sensors may put limitations on performance and robustness that cannot be overcome by the control design. Hence, the effects of different actuator and sensor sets on the closed-loop objectives of ASE systems must be analyzed to assure a successful control design.

Finally, the application of LPV control techniques for active flutter suppression of the

BFF aircraft was the third aspect considered in this dissertation. The control objectives were the suppression of dangerous ASE interactions and structural attenuation of flexible modes across the flight envelope. However, a feasible LPV controller that meet these control objectives was only synthesized for part of the flight envelope. This numerical limitation was imposed by the rapid change in dynamics across the flight envelope. Another issue observed in the control design was the poor robustness margins that the aircraft had across the flight envelope. These poor robustness margins were the motivation to analyze the limitations in control of the BFF imposed by instabilities. The results showed that the available control bandwidth provided by the actuators could not achieve the desired performance with good stability margins. As a final recommendation, this dissertation proposed to perform a control limitation analysis previous to the design task in order to determine the appropriate actuator control bandwidth for the desired robustness and performance.

All the results presented in this dissertation leave several open topics for further research. The model reduction approach presented in Chapter 4 is still an *ad hoc* procedure applied to a particular system. In the future, the development of a model reduction method that can handle high-order models without pre-processing is desired. Having a one-step procedure that can successfully be applied to a broad range of ASE systems will generate more accurate models for control purposes. In addition, a deeper investigation on the error measures to determine the closeness of a reduced model to the full order model is required.

On the other hand, the combinatorial nature of the sensor selection approach proposed in Chapter 5 is the motivation to incorporate a sparsity condition for the controller into the optimization problem. This condition will minimize the number of nonzero rows or columns in order to find the minimum subset of actuator and sensors that will achieve the desired robust performance. With this, the limitation of the method to a determined number of configurations will be eliminated.

In Chapter 6, a LPV controller was synthesized only for part of the flight envelope. This indicates that it was challenging for the LPV rate-bounded controller synthesis algorithm to find a parameter-varying controller that stabilizes all the plant models in the set and achieves the desired performance. Further investigation is required to determine the reasons for which the algorithm does not obtain a feasible solution. On the other hand, this LPV controller was only designed for flutter suppression objectives. In the future, the introduction of handling qualities in the control problem is desired. An integrated control design will guarantee global stability, flutter suppression, structural mode attenuation and good handling qualities. Finally, flight testing with these controllers will be the validation of all the work presented in this dissertation.

References

[1] H. Pfifer, C. Moreno, J. Theis, A. Kotikalpudi, A. Gupta, B. Takarics, and P. Seiler. Linear parameter varying techniques applied to aeroservoelastic aircraft: In memory of Gary Balas. Submitted to *1st IFAC Workshop on Linear Parameter Varying Systems*, Grenoble, France, 2015.

[2] A. Gupta, C. P. Moreno, H. Pfifer, B. Taylor, and G. J. Balas. Updating a finite element based structural model of a small flexible aircraft. In *AIAA Science and Technology Forum*, Kissimmee, FL, 2015.

[3] C. P. Moreno, A. Gupta, H. Pfifer, B. Taylor, and G. J. Balas. Structural model identification of a small flexible aircraft. In *American Control Conference*, pp. 4379–4384, 2014.

[4] E. Burnett, C. Atkinson, J. Beranek, B. Sibbitt, B. Holm-Hansen, and L. Nicolai. NDOF simulation model for flight control development with flight test correlation. In *AIAA Modeling and Simulation Technologies Conference*, vol. 3, pp. 7780–7794, Toronto, Canada, 2010.

[5] A. Kotikalpudi, H. Pfifer, and G. J. Balas. Unsteady aerodynamics analysis for a flexible unmanned aerial vehicle. Accepted to *AIAA Atmospheric Flight Mechanics Conference*, Boston, MA, 2015.

[6] B. Holm-Hansen, C. Atkinson, J. Benarek, E. Burnett, and H. Youssef. Envelope expansion of a flexible flying wing by active flutter suppression. In *AUVSI's Unmanned Systems North America*, Denver, CO, 2010.

[7] V. Mukhopadhyay. Flutter suppression control law design and testing for the active flexible wing. *Journal of Aircraft*, 32(1):45–51, 1995.

[8] B. Raghavan. *Flight dynamics and control of highly flexible flying wings*. PhD thesis, Aerospace and Ocean Engineering Department, Virginia Polytechnic Institute and State University, Blacksburg, VA, 2009.

[9] M. Waszak. Robust multivariable flutter suppression for the benchmark active control technology (BACT) wind-tunnel model. In *11th Symposium on Struct. Dynamics and Control*, Blacksburg, VA, 1997.

[10] P. Haley and D. Soloway. Generalized predictive control for active flutter suppression. *IEEE Control Systems*, 17(4):64–70, 1997.

[11] G. J. Balas. Linear, parameter-varying control and its application to aerospace systems. In *23rd Congress of International Council of the Aeronautical Sciences*, Toronto, Canada, 2002.

[12] J. M. Barker, G. J. Balas, and P. A. Blue. Gain-scheduled linear fractional control for active flutter suppression. *AIAA Journal of Guidance, Dynamics and Control*, 22(4):507–512, 1999.

[13] C. Van Etten, G. J. Balas, and S. Bennani. Linear parameter-varying integrated flight and structural mode control for a flexible aircraft. In *AIAA Guidance, Navigation and Control Conference*, Portland, OR, 1999.

[14] M. J. Patil and D. H. Hodges. Flight dynamics and control of highly flexible flying-wings. *Journal of Aircraft*, 43(6):1790–1798, 2006.

[15] R. Lind and M. Brenner. *Robust aeroservoelastic stability analysis*. Springer-Verlag, London, 1999.

[16] S. Benani, J. W. Van Staveren, B. Beuker, and J. J. Meijer. Flutter analysis of an F-16A/B in heavy store configuration. *Journal of Aircraft*, 42(6):1565–1574, 2005.

[17] R. Lind. Flutter margins for multimode unstable couplings with associated flutter confidence. *Journal of Aircraft*, 46(5):1563–1568, 2009.

[18] D. H. Baldelli, J. Zeng, R. Lind, and C. Harris. Flutter-prediction tool for flight-test-based aeroelastic parameter-varying models. *Journal of Guidance, Control and Dynamics*, 32(1):158–171, 2009.

[19] N. Nguyen and I. Tuzcu. Flight dynamics of flexible aircraft with aeroelastic and inertial force interactions. In *AIAA Atmospheric Flight Mechanics Conference*, Chicago, IL, 2009.

[20] MSC Software Corporation. MSC/NASTRAN structural and multidiscipline finite element analysis software package, 2012.

[21] Siemens PLM Software. FEMAP engineering finite element analysis software package, 2012.

[22] ZONA Technology Inc. ZAERO engineers toolkit for aeroelastic solutions software package, 2011.

[23] J. S. Shamma. *Analysis and design of gain scheduled control systems*. PhD thesis, Department of Mechanical Engineering, Massachusetts Institute of Technology, Cambridge, MA, 1988.

[24] G. Becker. *Quadratic stability and performance of linear parameter dependent systems*. PhD thesis, University of California, Berkeley, CA, 1993.

[25] A. Packard. Gain scheduling via linear fractional transformations. *Systems and Control Letters*, 22(2):79–92, 1994.

[26] F. Wu, X. H. Yang, A. Packard, and G. Becker. Induced L_2-norm control for lpv system with bounded parameter variation rates. In *Proceedings of the 1995 American Control Conference*, vol. 3, pp. 2379–2383, Seattle, WA, 1995.

[27] P. Apkarian and P. Gahinet. A convex characterization of gain-scheduled H_∞ controllers. *IEEE Transactions on Automatic Control*, 40(5):853–864, 1995.

[28] A. Helmersson. *Methods for robust gain scheduling*. PhD thesis, Department of Electrical Engineering, Linkoping University, Linkoping, Sweden, 1995.

[29] A. Packard and M. Kantner. Gain scheduling the LPV way. In *Proceedings of the 35th IEEE Conference on Decision and Control*, vol. 4, pp. 3938–3941, Kobe, Japan, 1996.

[30] H. Pfifer. *LPV/LFT Modeling and its Application in Aerospace*. PhD thesis, Technische Universitaet Munich, Munich, Germany, 2013.

[31] M. R. Waszak and D. K. Schmidt. Flight dynamics of aeroelastic vehicles. *Journal of Aircraft*, 25(6):563–571, 1988.

[32] M. Drela. Integrated simulation model for the preliminary aerodynamic, structural, and control-law design of aircraft. In *AIAA Structures, Structural Dynamics, and Materials Conference*, St. Louis, MO, 1999.

[33] M. J. Patil and D. H. Hodges. Nonlinear aeroelastic analysis of complete aircraft in subsonic flow. *Journal of Aircraft*, 37(5):753–760, 2000.

[34] L. Meirovitch and I. Tuzcu. The lure of the mean axes. *Journal of Applied Mechanics*, 74:497–504, 2007.

[35] C. M. Shearer and C. E. Cesnik. Nonlinear flight dynamics of very flexible aircraft. *Journal of Aircraft*, 44(5):1528–1545, 2007.

[36] T. M. Kier. Aerodynamic modelling for integrated loads analysis models. In *Third Symposium in Simulation of Wing and Nacelle Stall*, Braunschweig, Germany, 2012.

[37] K. L. Roger. Airplane math modeling methods for active control design. In *Structural Aspects of Active Controls*, Lisbon, Portugal, 1977.

[38] S. H. Tiffany and W. M. Adams Jr. Nonlinear programming extensions to rational function approximation methods for unsteady aerodynamic forces. Technical paper, National Aeronautics and Space Administration, Langley Research Center, Hampton, Virginia, 1988.

[39] A. Marcos and G. J. Balas. Development of linear, parameter-varying models for aircraft. *Journal of Guidance, Control and Dynamics*, 27(2):218–228, 2004.

[40] J. Beranek, L. Nicolai, M. Buonanno, E. Burnett, C. Atkinson, B. Holm-Hansen, and P. Flick. Conceptual design of a multi-utility aeroelastic demonstrator. In *13th AIAA/ISSMO Multidisciplinary Analysis Optimization Conference*, vol. 3, pp. 2194–2208, Fort Worth, TX, 2010.

[41] T. Chandrupatla and A. D. Belegundu. *Introduction to Finite Elements in Engineering*. Prentice Hall, Upper Saddle River, NJ, 3rd ed. edition, 2001.

[42] A. Kotikalpudi, C. P. Moreno, B. Taylor, H. Pfifer, and G. J. Balas. Low cost development of a nonlinear simulation for a flexible uninhabited air vehicle. In *American Control Conference*, pp. 2029–2034, 2014.

[43] R. W. Clough and J. Penzien. *Dynamics of Structures*. Computers & Structures, Inc., Berkeley, CA, 1995.

[44] A. K. Chopra. *Dynamics of Structures: Theory and Application to Earthquake Engineering.* Prentice Hall, Englewood Cliffs, NJ, 1995.

[45] D. J. Ewins. *Modal Testing: Theory and Practice.* Research Studies Press Ltd., England, 1984.

[46] Inc. Agilent Technologies. Agilent 35670A service guide, 2011.

[47] Inc. Agilent Technologies. Agilent 35670A operator's guide, 2010.

[48] L. Ljung. *System Identification: Theory for the User.* Prentice Hall, Englewood Cliffs, NJ, 1987.

[49] J. N. Juang and R. S. Pappa. An eigensystem realization algorithm for modal parameter identification and model reduction. *Journal of Guidance, Control and Dynamics*, 8(5):620–627, 1985.

[50] J. M. Caicedo, S. J. Dyke, and E. A. Johnson. Natural excitation technique and eigensystem realization algorithm for phase I of the IASC-ASCE benchmark problem: Simulated data. *Journal of Engineering Mechanics*, 130(1):49–60, 2004.

[51] The Mathworks Inc. MATLAB language of technical computing software package, 2012.

[52] L. Ljung. *System Identification Toolbox: User's Guide.* The Mathworks Inc, ver. 9.0 (release 2014a), 2014.

[53] B. J. Schwarz and M. H. Richardson. Experimental modal analysis. In *CSI Reliability Week*, Orlando, FL, 1999.

[54] S. Gade, H. Herlufsen, and H. Konstantin-Hansen. How to determine the modal parameters of simple structures. *Sound and Vibration*, 36(1):72–73, 2002.

[55] H. J. Henriksen, L. Troldorg, P. Nyegaard, T. O. Sonnenborg, J. C. Refsgaard, and B. Madsen. Methodology for construction, calibration and validation of a national hydrological model for denmark. *Journal of Hidrology*, 280(1):52–71, 2003.

[56] G. Vinnicombe. *Measuring Robustness of Feedback Systems.* PhD thesis, University of Cambridge, Cambridge, England, 1992.

[57] K. Zhou, J. Doyle, and K. Glover. *Robust and optimal control.* Prentice Hall, Upper Saddle River, NJ, 1996.

[58] G. Vinnicombe. Frequency domain uncertainty and the graph topology. *IEEE Transactions on Automatic Control*, 38(9):1371–1383, 1993.

[59] G. Buskes and M. Cantoni. Reduced order approximation in the ν-gap metric. In *Proceedings of the 46th IEEE Conference on Decision and Control*, pp. 4367–4372, New Orleans, LA, 2007.

[60] A. Sootla. ν-gap model reduction in the frequency domain. In *American Control Conference*, pp. 5025–5030, San Francisco, CA, 2011.

[61] S. Lall and C. Beck. Error-bounds for balanced model-reduction of linear time-varying systems. *IEEE Transactions on Automatic Control*, 48(6):946–956, 2003.

[62] R. Saragih. Model reduction of linear parameter varying systems based on LMIs. In *Proceedings of the 2nd IMT-GT Regional Conference on Mathematics, Statistics and Applications*, Penang, Malaysia, 2006.

[63] G. D. Wood. *Control of parameter-dependent mechanical systems*. PhD thesis, Aerospace and Ocean Engineering Department, Cambridge University, Cambridge, UK, 1995.

[64] R. Widowati and R. Bambang. Model reduction of LPV control with bounded parameter variation rates. In *6th Asian Control Conference*, Bali, Indonesia, 2006.

[65] G. D. Wood, P. J. Goddard, and K. Glover. Approximation of linear parameter-varying systems. In *Proceedings of the 35th IEEE Conference on Decision and Control*, vol. 4, pp. 406–411, Kobe, Japan, 1996.

[66] R. Widowati, R. Bambang, R. Sagari, and S. M. Nababan. Model reduction for unstable LPV system based on coprime factorizations and singular perturbation. In *5th Asian Control Conference*, pp. 963–970, Melbourne, Australia, 2004.

[67] S. Skogestad and I. Postlethwaite. *Multivariable Feedback Control: Analysis and Design*. John Wiley and Sons Ltd, Chichester, England, 2nd edition, 2005.

[68] M. Green and D. J. N. Limebeer. *Linear Robust Control*. Prentice Hall, Englewood Cliffs, N. J., 1st edition, 1995.

[69] Y. Liu and B. D. O. Anderson. Singular perturbation approximation of balanced systems. In *Proceedings of the 28th IEEE Conference on Decision and Control*, pp. 1355–1360, Tampa, FL, 1989.

[70] M. G. Safonov and R. Y. Chiang. A schur method for balanced-truncation model reduction. *IEEE Transactions on Automatic Control*, 34(7):729–733, 1989.

[71] A. C. Or, J. L. Speyer, and J. Kim. Reduced balancing transformations for large non-normal state-space systems. *Journal of Guidance, Control, and Dynamics*, 35(1):129–137, 2012.

[72] M. van de Wal and Bram de Jager. A review of methods for input/output selection. *Automatica*, 37(4):487–510, 2001.

[73] M. Morari. Design of resilient processing plants III: A general framework for the assessment of dynamic resilience. *Chemical Engineering Science*, 38(11):1881–1891, 1983.

[74] S. Skogestad, M. Morari, and J. C. Doyle. Robust control of ill-conditioned plants: high purity distillation. *IEEE Transactions on Automatic Control*, 33(12):1092–1105, 1988.

[75] E. H. Bristol. On a new measure of interactions for multivariable process control. *IEEE Transactions on Automatic Control*, 11(1):133–134, 1996.

[76] R. Weber and C. B. Brosilow. Use of secondary measurements to improve control. *AIChE Journal*, 18(3):614–623, 1972.

[77] N. K. Dhingra, M. R. Jovanovic, and Z. Q. Luo. An ADMM algorithm for optimal sensor and actuator selection. In *Proceedings of the 53rd IEEE Conf. on Decision and Control*, pp. 4039–4044, Los Angeles, CA, 2014.

[78] B. Joseph and C. B. Brosilow. Inferential control of processes. *AIChE Journal*, 24(3):485–492, 1978.

[79] A. Albertos. Relevance of actions and measurements in control performance. *Australian Journal of Electrical and Electronics Engineering*, 2(2):159–166, 2005.

[80] G. J. Balas and P. M. Young. Sensor selection via closed-loop control objectives. *IEEE Transactions on Control Systems Technology*, 7(6):692–705, 1999.

[81] M. Van de Wal, P. Philips, and B. De Jager. Actuator and sensor selection for an active vehicle suspension aimed at robust performance. *International Journal of Control*, 70(2):703–720, 1998.

[82] D. E. Rivera. A structured singular value test for variable selection and pairing. In *Proceedings of 1989 American Control Conference*, pp. 560–565, Pittsburgh, PA, 1989.

[83] R. D. Braatz, J. H. Lee, and M. Morari. Screening plant designs and control structures for uncertain systems. *Computers and Chemical Engineering*, 20(2):463–468, 1996.

[84] J. H. Lee, R. D. Braatz, M. Morari, and A. Packard. Screening tools for robust control structure selection. *Automatica*, 31(1):229–235, 1995.

[85] G. Stein and J. Doyle. Beyond singular values and loop shapes. *Journal of Guidance, Control, and Dynamics*, 14(1):5–16, 1991.

[86] G. J. Balas, J. Doyle, K. Glover, A. Packard, R. Smith, MUSYN, and The Mathworks. μ-analysis and synthesis toolbox: Users guide, 2001.

[87] A. Packard, J. Doyle, and G. J. Balas. Linear multivariable robust control with a μ perspective. *Journal of Dynamics, Measurements and Control: Special Edition on Control*, 115(2(B)):426–438, 1993.

[88] G. Dullerud and F. Paganini. *A course in robust control theory: A convex approach.* Springer, New York, NY, text in applied mathematics, no. 36, 2000.

[89] M. Hanel. *Robust Integrated Flight and Aeroelastic Control System Design for a Large Transport Aircraft.* PhD thesis, University of Stuttgart, Dusseldorf, Germany, 2001.

[90] J. Theis, H. Pfifer, G. J. Balas, and H. Werner. Integrated flight control design for a large flexible aircraft. In *submitted to the American Control Conference*, 2015.

[91] J. S. Shamma and M. Athans. Gain scheduling: Potential hazards and possible remedies. In *American Control Conference*, Boston, MA, 1991.

[92] G. J. Balas, C. P. Moreno, and P. Seiler. Robust aeroservoelastic control utilizing physics-based aerodynamic sensing. In *AIAA Guidance, Navigation and Control Conference*, pp. AIAA–2012–4897, 2012.

[93] F. Wu. *Control of Linear Parameter Varying Systems.* PhD thesis, University of California at Berkeley, Berkeley, CA, 1995.

[94] A. Hjartarson, P. J. Seiler, and G. J. Balas. LPV aeroservoelastic control using the LPVtools toolbox. In *AIAA Atmospheric Flight Mechanics Conference*, Boston, MA, 2013.

[95] J. S. Freudenberg and D. P. Looze. Right half plane zeros and poles and design tradeoffs in feedback systems. *IEEE Transactions of Automatic Control*, 30(6):555–565, 1985.

[96] H. Havre and K. Skogestad. Directions and factorizations of zeros and poles in multivariable systems. Technical report, Norwegian University of Science and Technology, Trondhein, Norway, 1996.

[97] G. Stein. Respect the unstable. *IEEE Control Systems*, 23(4):12–25, 2003.

[98] R. L. Dailey. Lecture notes for the workshop on $\mathcal{H}_\infty$ and μ methods for robust control. In *IEEE Conference on Decision and Control*, Brighton, England, 1991.